NASA Contractor Report 166088

NASA-CR-166088
19830021001

Development of Monofilar Rotor Hub Vibration Absorber

J. Duh, W. Miao

United Technologies Corporation
Sikorsky Aircraft Division

CONTRACT NAS1-16700
May 1983

Prepared for Structures Laboratory
AVRADCOM Research and Technology Laboratories
and NASA-Langley Research Center
under Contract NAS1-16700

NASA
National Aeronautics and
Space Administration

Langley Research Center
Hampton, Virginia 23665

NASA Contractor Report 166088

Development of Monofilar Rotor Hub Vibration Absorber

J. Duh, W. Miao

United Technologies Corporation
Sikorsky Aircraft Division

CONTRACT NAS1-16700
May 1983

Prepared for Structures Laboratory
AVRADCOM Research and Technology Laboratories
and NASA-Langley Research Center
under Contract NAS1-16700

National Aeronautics and
Space Administration

Langley Research Center
Hampton, Virginia 23665

This Page Intentionally Left Blank

TABLE OF CONTENTS

LIST OF FIGURES

LIST OF FIGURES (Continued)

LIST OF FIGURES (Continued)

LIST OF TABLES

SUMMARY

The results of a monofilar design and bench test are presented. A monofilar is a centrifugally tuned two degree-of-freedom hub absorber that provides force attenuation at two frequencies using the same dynamic mass. Linear and non-linear analyses of the coupled monofilar/airframe system were developed to study tuning and performance characteristics for vibration reduction. Based on these analyses, a four-bladed monofilar configuration was designed and fabricated. Monofilar tuning and performance were evaluated through controlled ground tests. Impact bench tests were conducted to verify the calculated non-rotating natural frequencies and mode shapes. Performance characteristics were verified using a rotating absorber test facility. These tests showed significant attenuation of fixed-system 4P hub motions due to 3P inplane rotating-system hub forces. In addition, detuning effects of the 3P monofilar modal response were small due to nonlinearities and tuning pin slippage. However, attenuation of 4P hub motions due to 5P inplane hub forces was poor. The performance of the 5P monofilar modal response was degraded by torsional motion of the dynamic mass relative to the support arm which resulted in binding of the dynamic components. Analytical design studies were performed to evaluate this torsional motion problem. An alternative design is proposed which may alleviate the torsional motion of the dynamic mass.

INTRODUCTION

A primary source of vibration for a single rotor helicopter is the main rotor. The shear forces generated by rotor blade airload distributions at the blade root are summed and filtered by the main rotor to produce hub forces which excite the airframe. This excitation in the non-rotating coordinate system is at the main rotor blade passage frequency, which is the product of the number of main rotor blades and the rotor speed.

The NP hub vertical force and yaw moment are caused by forces and moments in the rotating system at the same frequency. The frequency is maintained during the transformation from the rotating to non-rotating systems due to the symmetric nature of the excitation. However, the inplane hub forces are caused by cyclic blade forces at two frequencies in the rotating system, (N-1)P and (N+1)P. Since the inplane hub forces are the primary excitations of the aircraft, reducing the 3P and 5P rotating hub forces for a four-bladed rotor will greatly reduce overall 4P airframe vibration levels.

The stringent vibration requirements of the current generation of helicopters usually require some form of vibration control beyond airframe and rotor detuning. A proven and effective vibration control device is the rotor hub mounted centrifugally tuned bifilar absorber (References 1, 2, and 3). This absorber cancels rotor excitation forces at the hub thereby reducing the airframe vibration.

To date, the bifilar has been effectively and extensively used to control vibration on Sikorsky helicopters. Because of the bifilar construction, twin holes and tuning pins, the dynamic mass is restricted to pure translation. The bifilar has only one degree-of-freedom, and can be tuned to only one frequency. Consequently, two sets of bifilars are required in theory to suppress the inplane hub forces at NP; one bifilar set is tuned to (N-1)P and the other set to (N+1)P.

The bifilar tuned to (N-1)P has been applied to numerous Sikorsky helicopters: the S-58T, the S-61 series, the S-70 and the S-72. Two sets of bifilars, one set tuned to 3P and one set tuned to 5P, have been used successfully on the Sikorsky S-76 helicopter.

Figure 1 shows schematically the components of the bifilar system. The primary components are a support frame arm and sets of masses each of which is comprised of a dynamic mass, and two cylindrical tuning pins. These pins constrain the mass radially and, together with the circular tracking holes in the support arm and the dynamic mass define the pendular radius of the mass. A typical helicopter installation of a bifilar is shown in Figure 2.

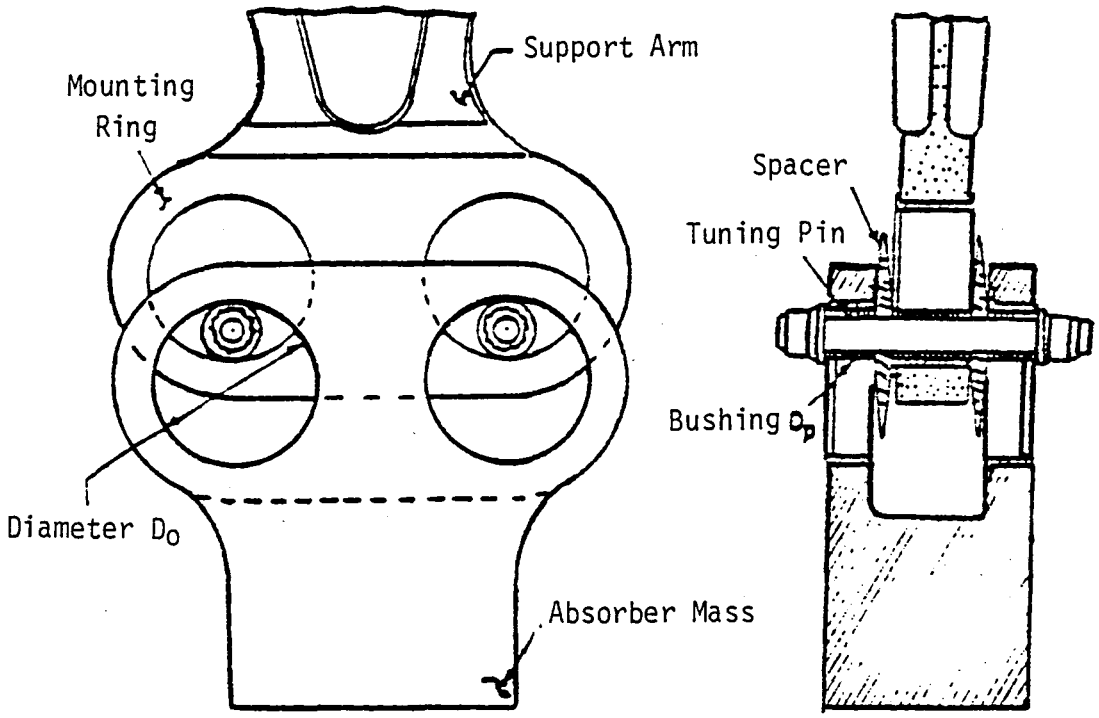

Figure 1. Bifilar Absorber Assembly.

Figure 2. Bifilar Installed on Aircraft.

The calculated reduction of overall aircraft vibration levels through the application of an (N-1)P bifilar is shown in Figure 3. This significant vibration reduction is not only important for pilot/passenger ride comfort but is very important to the reliability of all airframe components which are subject to the vibration environment.

To reduce the number of rotor absorber parts and the total overall absorber weight, the dual frequency absorber was conceived. This rotor absorber has been termed the monofilar (Reference 4). The monofilar absorber will attenuate both (N-1)P and (N+1)P rotor forces. The dynamic mass and pin both rotate and translate relative to the support arm which provides a dual frequency system that can be tuned to 3P and 5P for a four-bladed helicopter.

This report summarizes a design and test program to develop the monofilar concept, to demonstrate its performance and to define the appropriate monofilar design methodology and criteria.

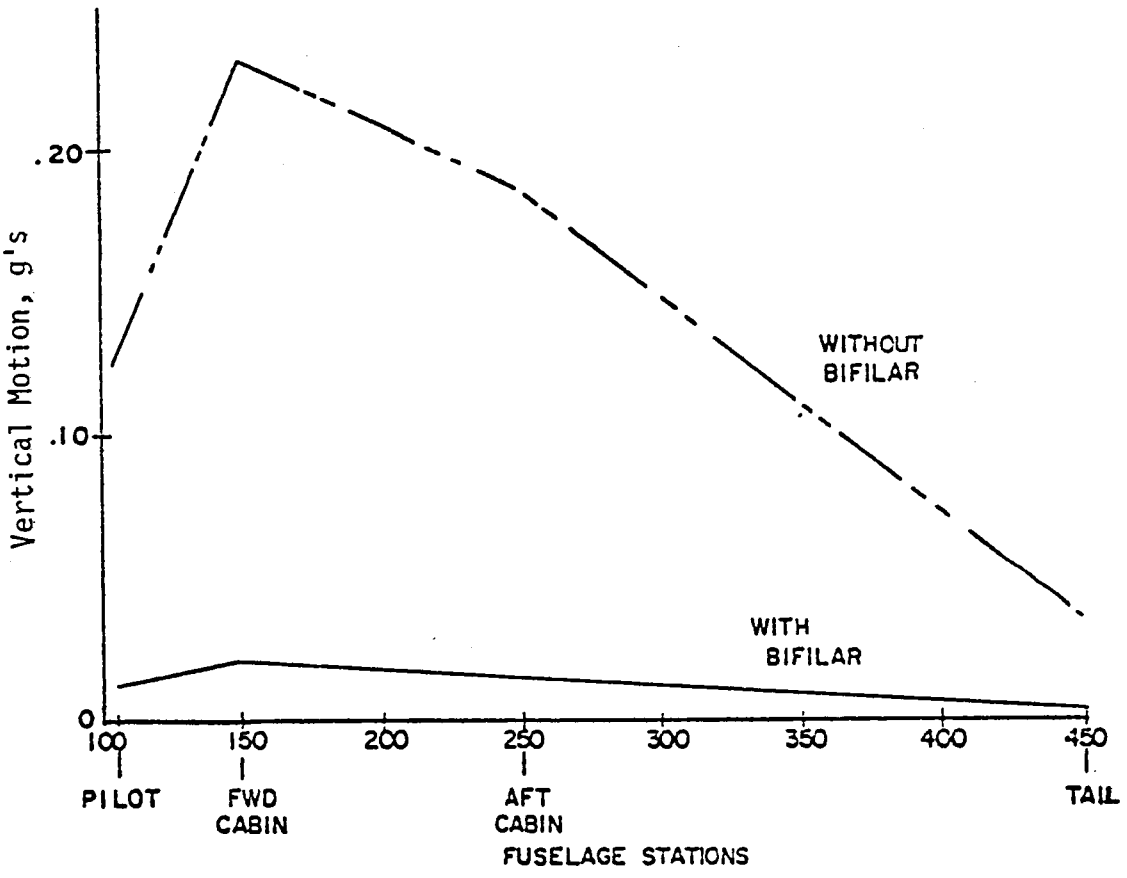

Figure 3. Calculated Bifilar Effect on Aircraft Vibration.

LIST OF SYMBOLS

CG	Center of gravity
D_1	Diameter of arm bushing, m (in.)
D_2	Diameter of mass bushing, m (in.)
d	Diameter of tuning pin, m (in.)
g	Gravitational acceleration, m/sec^2 (in./sec^2)
I	Inertia of dynamic mass, kg - m^2 (lb-in.-sec^2)
I_p	Inertia of pin mass, kg - m^2 (lb-in.-sec^2)
m	Dynamic mass, kg (lb-sec^2/in.)
m_p	Pin mass, kg (lb-sec^2/in.)
m_G	Fixed system generalized mass, kg (lb-sec^2/in.)
M_T	Total dynamic mass, kg (lb-sec^2/in.)
NP	Blade passage frequency, Hz
Q_{3P}	3P mode amplification factor
Q_{5P}	5P mode amplification factor
R_o	Distance from center of rotation to center of arm bushing, m (in.)
r_1	D_1 - d, m (in.)
r_2	D_2 - d, m (in.)
ΔR	CG offset of the dynamic mass from the center of mass bushing, m (in.)
ψ	Hub rotational angle, deg
Ω	Rotor speed, Hz
ζ	Percent critical damping

MONOFILAR DESIGN

The monofilar is a rotor absorber which has the capability of providing force attenuation in the rotating system at two frequencies using the same dynamic mass. To establish a monofilar design, analytical tools were developed that provide rapid evaluation of monofilar designs for tuning and absorber attenuation performance. The performance analyses were further expanded to include non-linear effects and fixed-system airframe dynamics which affect the monofilar absorber performance. Parametric studies using these analyses determine acceptable monofilar designs. Although these studies were performed for a rotor absorber designed for a four-bladed helicopter, the analyses developed will generate and evaluate monofilar designs for a rotor system with any number of blades.

Overview

The monofilar design is similar to the bifilar design. Both absorber designs use the centrifugal force field for the absorber mass restoring spring and therefore, the absorber remains tuned as the rotor speed is varied. This self-tuning feature is desirable since it permits the aircraft to fly at any of its normal operating rotor speeds without degradation in rotor absorber effectiveness.

The monofilar can be visualized as one half of a standard bifilar. Each monofilar unit consists of one hub arm with a single hole and tuning pin which joins the arm to the dynamic mass. This is shown schematically in Figure 4. Unlike the bifilar, the monofilar dynamic mass can rotate as well as translate, giving two degrees-of-freedom and, therefore, two natural frequencies. By proper choice of the monofilar design parameters such as mass, inertia, mass of pin, inertia of pin and geometry, the two natural frequencies can be located at (N-1)P and (N+1)P which are the principal inplane excitation frequencies in the rotating system. Therefore, one monofilar can be used in place of two bifilars to cancel both rotating-system inplane excitation forces. Thus, a monofilar design offers potential benefits relative to a bifilar in terms of simplicity, weight, and cost. For example, a monofilar absorber has 80 percent fewer major parts compared with two sets of bifilars which would be required to react both the (N-1)P and (N+1)P frequency forces.

Monofilar Analyses

Figure 5 describes the two degree-of-freedoms, γ_1 and γ_2, used to define the motion of a monofilar dynamic mass. Angular motion γ_1 is defined as the rotation of the pin in the arm bushing and γ_2 is the angular rotation of the dynamic mass around the pin.

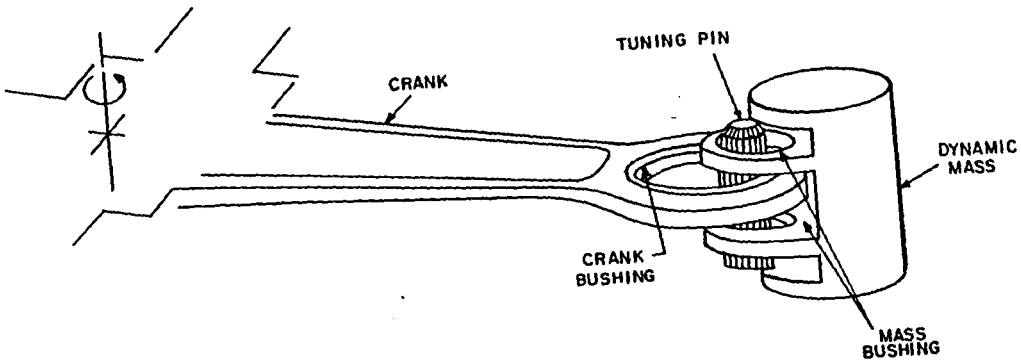

Figure 4. Monofilar Schematic.

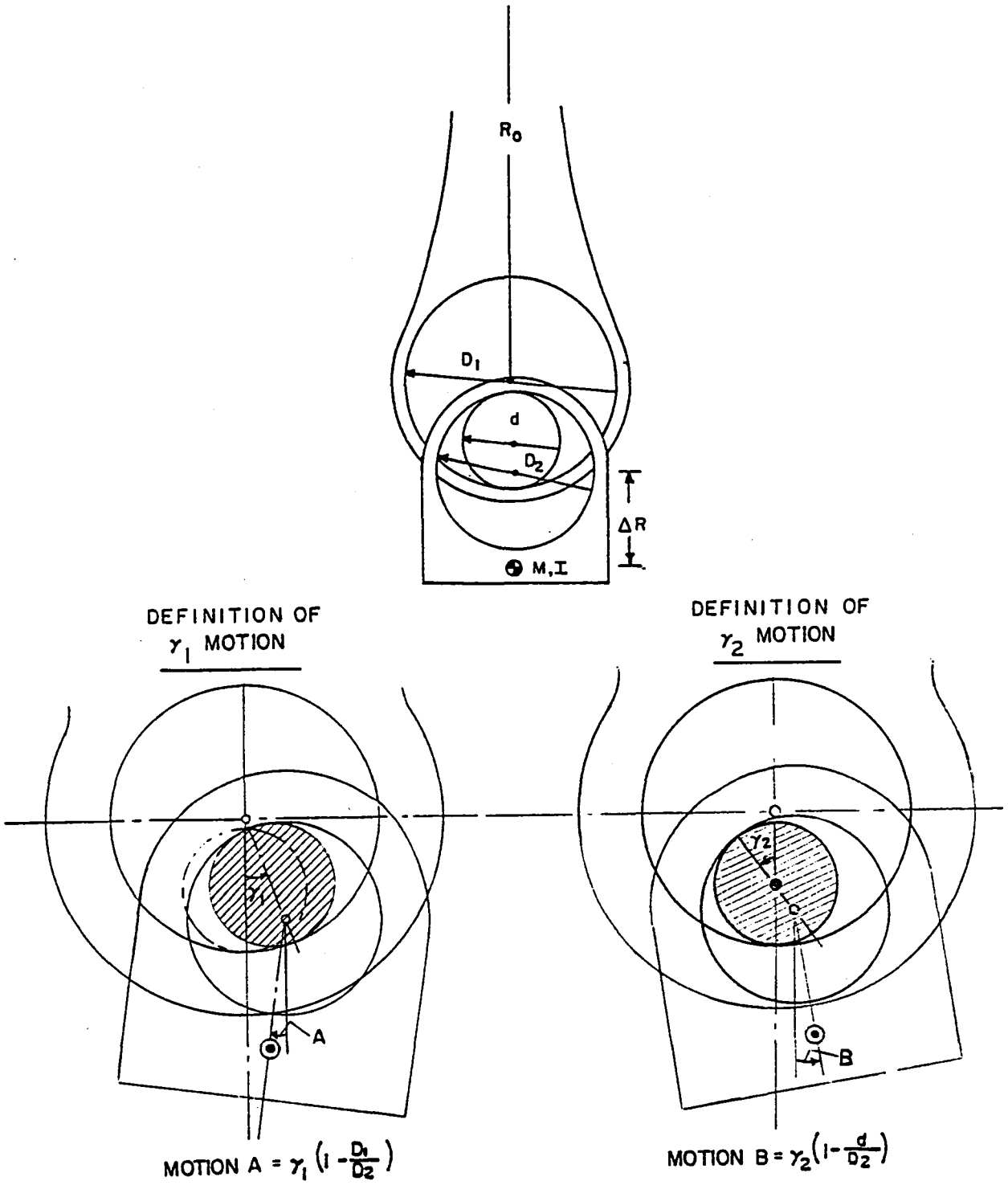

Figure 5. Definitions of Monofilar Motions.

A coupled monofilar/airframe nonlinear analysis was developed to evaluate the monofilar tuning and attenuation characteristics due to rotating inplane (N-1)P and (N+1)P forces. The analysis includes: (1) modeling of up to ten monofilars; (2) forcing excitations up to ten rotor speed harmonics; and (3) fixed-system lateral and longitudinal dynamics. A derivation of the coupled nonlinear equations of motion are presented in the Appendix. The analysis also provides an option to use linearized equations.

The linearized equations of motion are useful to establish relationships among the pertinent parameters that affect the tuning and performance of the system. The linearized tuning equations for a fixed-hub are shown below in equations (1) and (2).

$$\{[\frac{r_1+r_2}{2} + \Delta R \quad (1-\frac{D_1}{D_2})]^2 + \frac{I}{m} \quad (1-\frac{D_1}{D_2})^2$$

$$+ \frac{m_p}{m} \quad [\frac{r_1}{4}^2 + \frac{I_p}{m_p} \quad (\frac{r_1}{d})^2]\} \quad \ddot{\gamma}_1$$

$$+ \quad \{\frac{r_2}{2} \quad [\frac{r_1+r_2}{2} + 2\Delta R \quad [\frac{\Delta R}{D_2} \quad (1-\frac{D_1}{D_2}) \quad + \frac{r_2}{D_2}]]$$

$$+ \frac{I}{m} \quad \frac{r_2}{D_2} \quad (1-\frac{D_1}{D_2})\} \ddot{\gamma}_2$$

$$+ \Omega^2 \quad \{\frac{r_1+r_2}{2} [R_o + \Delta R \quad (\frac{D_1}{D_2})^2] + R_o \Delta R \quad (1-\frac{D_1}{D_2})^2$$

$$+ \frac{m_p}{m} \quad \frac{r_1}{2} R_o\} \gamma_1$$

$$+\Omega^2 \quad \{\frac{r_2}{2} [R_o + \frac{\Delta R}{D_2} \quad \frac{D_1}{D_2} (d-r_1) + 2R_o \frac{\Delta R}{D_2} \quad (1-\frac{D_1}{D_2})]\} \gamma_2 = 0 \qquad (1)$$

$$\left\{\frac{r_2}{2}\left[\frac{r_1+r_2}{2} + 2\Delta R\left[\frac{\Delta R}{D_2}\left(1-\frac{D_1}{D_2}\right) + \frac{r_2}{D_2}\right]\right.\right.$$

$$\left.\left. + \frac{I}{m}\frac{r_2}{D_2}\left(1-\frac{D_1}{D_2}\right)\right\}\ddot{\gamma}_1\right.$$

$$+\left\{\left(\frac{r_2}{2}\right)^2 + \left(\frac{r_2\Delta R}{D_2}\right)^2 + r_2^2\frac{\Delta R}{D_2} + \frac{I}{m}\left(\frac{r_2}{D_2}\right)^2\right\}\ddot{\gamma}_2$$

$$+\Omega^2\left\{\frac{r_2}{2}\left[R_o + \frac{\Delta R}{D_2}\frac{D_1}{D_2}(d-r_1) + 2R_o\frac{\Delta R}{D_2}\left(1-\frac{D_1}{D_2}\right)\right]\right.\gamma_1$$

$$+\Omega^2\left\{\frac{r_2}{2}\left[\frac{r_1}{2} + R_o + \frac{\Delta R}{D_2^2}\left[2r_2R_o + r_1r_2 + d^2\right]\right]\right\}\gamma_2 = 0 \qquad (2)$$

As shown in the equations (1) and (2), the absorber dynamic mass frequencies are determined by the following parameters.

- Dynamic mass, m
- Inertia of dynamic mass, I
- CG offset of dynamic mass, ΔR
- Diameter of mass bushing, D_2
- Diameter of arm (crank) bushing, D_1
- Arm (crank) length, R_o
- Tuning pin mass, m_p
- Tuning pin inertia, I_p
- Diameter of tuning pin, d

Design Studies

As outlined in the Monofilar Analyses section there are nine parameters that determine the two frequencies of the monofilar. For an inplane rotor absorber on a four-bladed helicopter, the goal was to design the monofilar to attenuate inplane rotating hub forces at 3P and 5P frequencies with a total weight less than two bifilars. From previous experience with single frequency bifilar system on many different helicopters, a majority of the monofilar design parameters were estimated and the required 3P and 5P tuning was achieved by adjusting the diameters of the bushings of the arm and the mass.

A realistic length of the arm of the monofilar, R_o, should be of the order of .406 m (16 inches) for clearance and drag considerations. The dynamic mass, m of the order of 15.876 kilograms (35 pounds), since the total weight should be approximately one percent of the total aircraft weight. Center of gravity offset of the dynamic mass, ΔR, less than .051 m (two inches) for drag and clearance considerations. Finally, the dimensions of the pin were restricted by the Hertz stresses, i.e., the surface stress calculated for a cylinder of diameter d under a load per unit of length. For this, the pin diameter should be greater than .033 m (1.3 inches) and at least .051 m (2 inches) in length to withstand the surface stresses. Using the above considerations, the desired natural frequencies (3P and 5P for a four-bladed rotor) could be obtained with physically achievable mass, inertia, and geometric properties.

The effects of these parameters on monofilar tuning, calculated by the linear tuning analysis, are shown in Figure 6. Variations in tuning pin diameter, d, and inertia, I_p, primary affect mostly the 5P mode frequency. On the other hand, the arm length, R_o, and CG offset, ΔR, affect both 3P and 5P mode frequencies.

Again, from previous experience with single frequency rotor absorbers, it was expected that over-tuning the monofilar would provide improved performance when the hub force excitation levels at 3P or 5P frequency become large. These forces excite the dynamic masses and when angular excursions increase, the non-linear effects decrease the mass natural frequency. This detunes the absorber and reduces its ability to react the forces applied. Using the two degree-of-freedom non-linear analysis described in the Appendix this detuning effect was studied. Figures 7 and 8 show that for low levels of hub input excitation (e.g. hub acceleration a_{3P} = .15 g's and a_{5P} = .04 g's) the monofilar maximum performance occurs with tuning equal to the excitation frequency, 3P and 5P respectively. However, at higher excitation levels, the maximum performance occurs at tunings above 3P and 5P. Figure 9 shows that possible ranges and combinations of 3P and 5P monofilar dynamic mass tuning can be obtained by selecting the proper diameters of the arm and mass bushings.

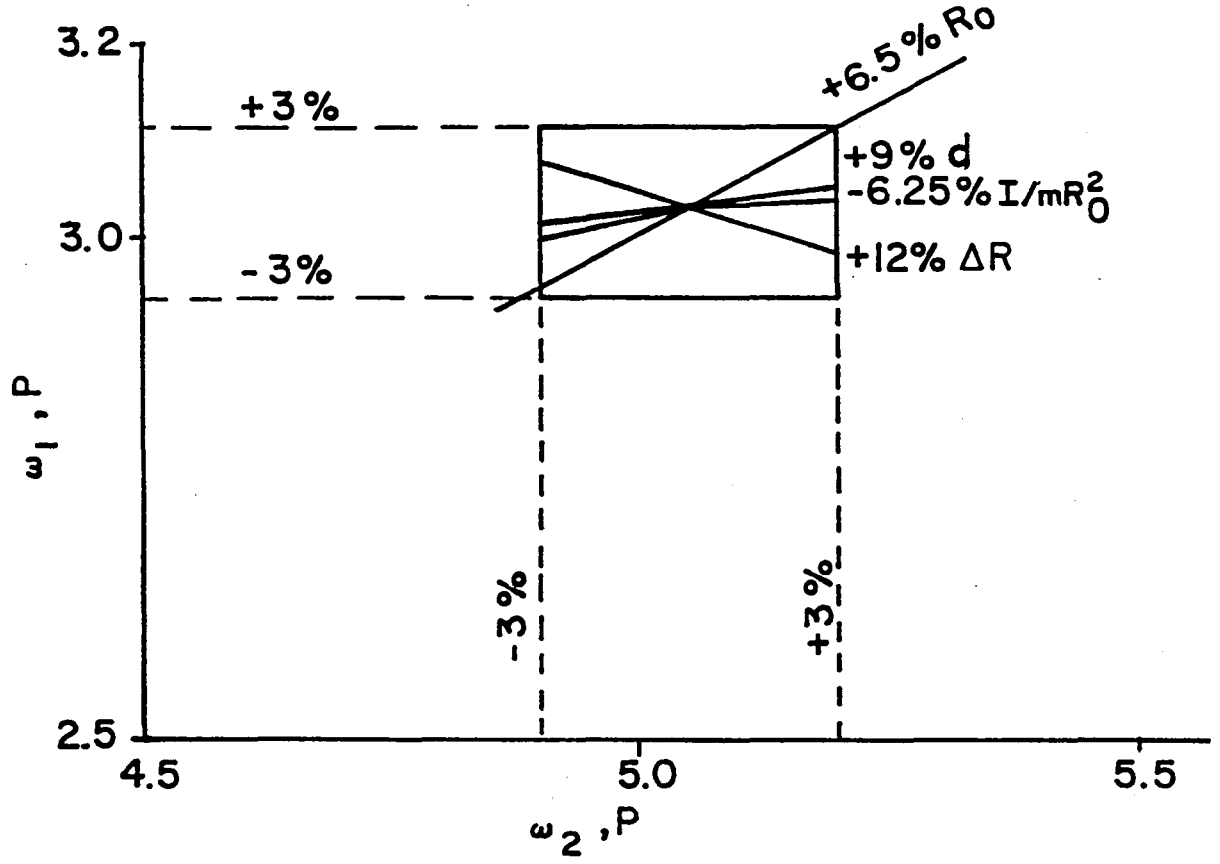

Figure 6. Typical Tuning Chart for Design.

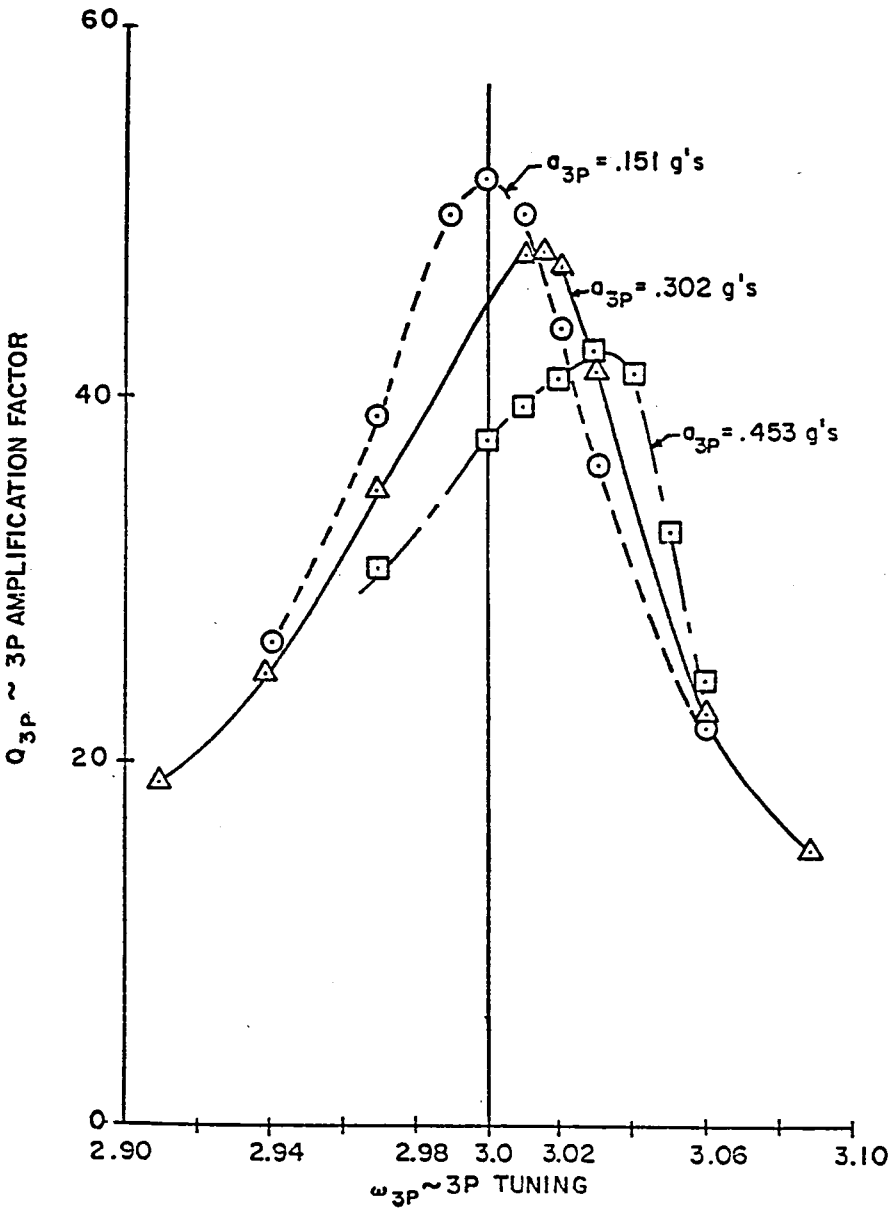

Figure 7. Predicted Non-Linear Effects on 3P Amplification and Tuning.

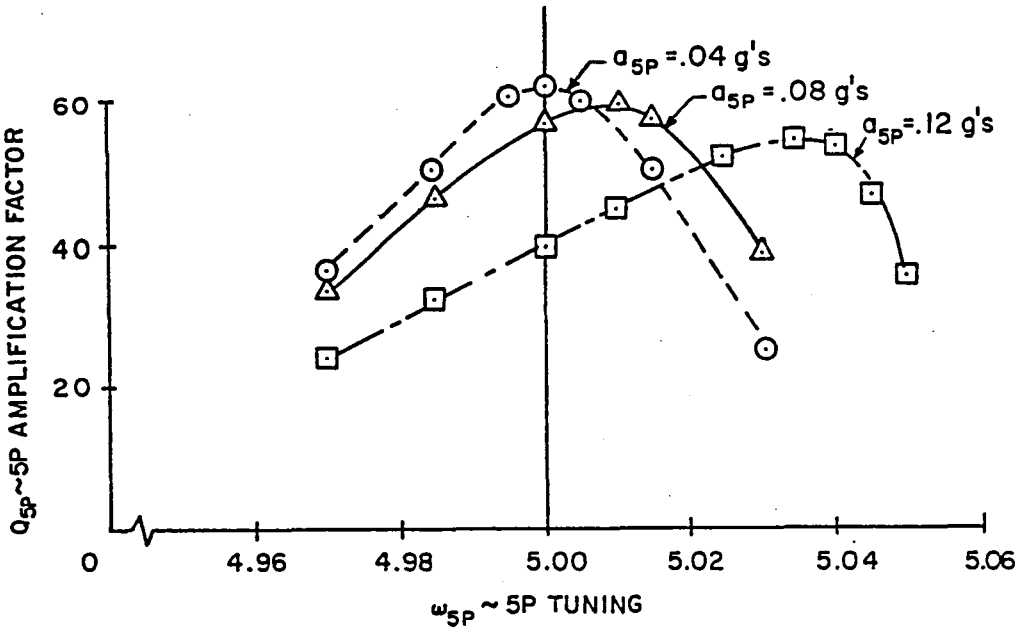

Figure 8. Predicted Non-Linear Effects on 5P Amplification and Tuning.

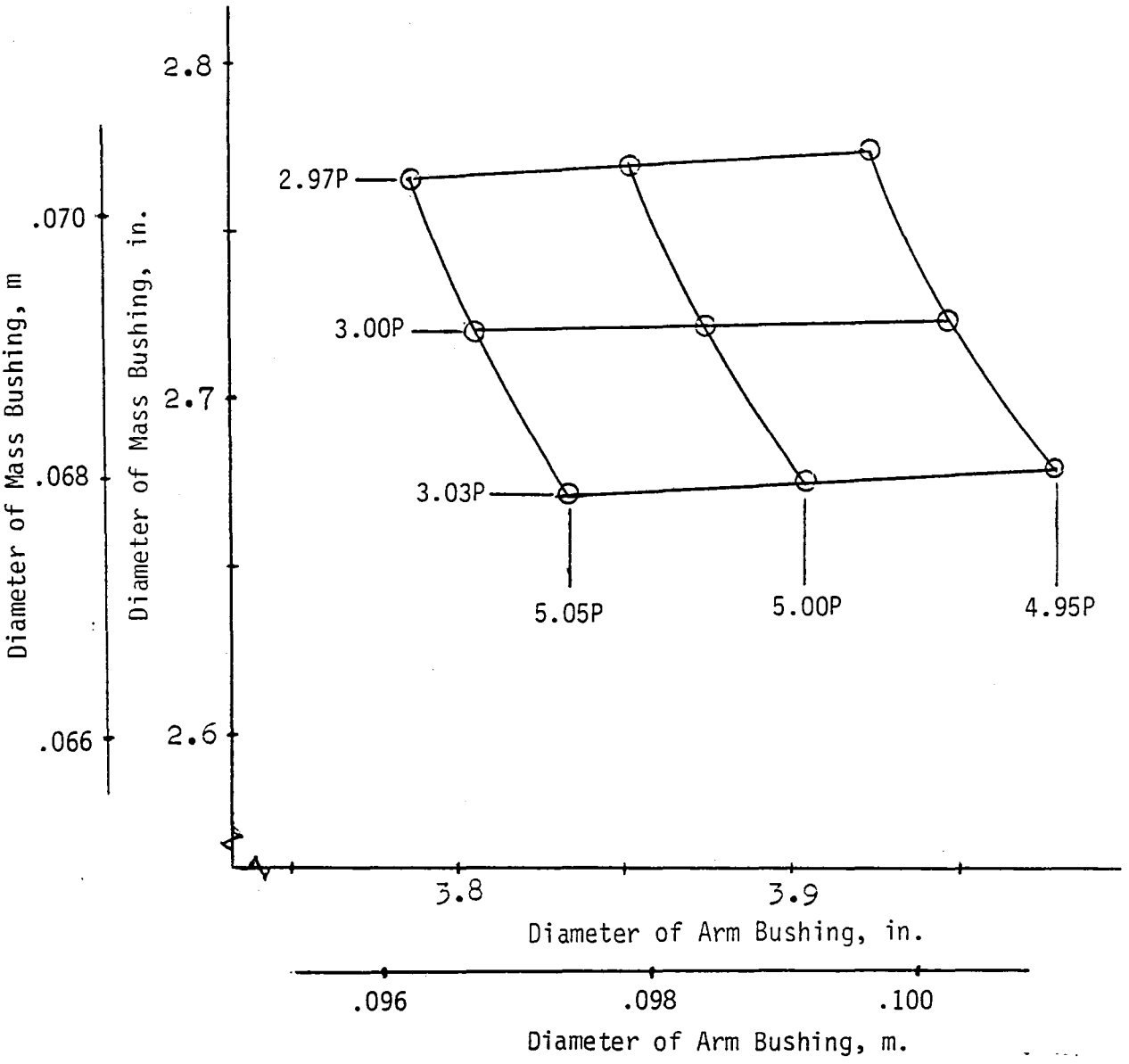

Figure 9. Monofilar Tuning as a Function of Arm and Mass Bushing Diameters.

The non-linear performance of the monofilar was analyzed for a four-mass monofilar mounted on an airframe with lateral and longitudinal hub impedance and excited by 3P and 5P rotating hub forces. Figure 10 shows the predicted monofilar performance as a function of applied 3P or 5P hub forces. The monofilar performance is determined by dividing the calculated residual 4P fixed-system hub force by the magnitude of the applied rotating excitation force. For the case of very small monofilar masses the attenuation is equal to one. As shown, the monofilar attenuation of rotor forces is strongly affected by the proximity of the airframe modes to 4P. For the configuration analyzed, the fixed-system longitudinal mode was placed below 4P and the lateral mode above. The results showed that the predicted attenuation is acceptable if the airframe modes are within approximately ±0.5P of 4P, and that the attenuation will degrade as the modes are moved away from 4P.

The preceding results were predicted for the case of the monofilar dynamic mass tuned exactly to 3P and 5P. Figure 11 shows that overtuning the monofilar dynamic mass to 3.03P and 5.04P improved the attenuation of the fixed system response at higher 3P rotor forces but did not improve the attenuation for 5P excitation. However, as shown in Figure 12 if the monofilar dynamic mass weight is increased by 44 percent, then the attenuation showed a considerable improvement for all configurations. This increased weight configuration tuned the dynamic mass to 3.0P and 5.0P.

Proper functioning of the monofilar requires sufficient friction between the pin surface and the mass and arm bushings to prevent slipping. For the present design of steel on steel, it was calculated that a range of mass angular motions of 18 to 33 degrees could be achieved. This was considered to be more than sufficient to evaluate the monofilar concept, since this range allowed testing in both the linear and non-linear ranges of the dynamic mass motion.

Final Design and Fabrication

Figure 13 shows the schematic of the monofilar final design that was determined from the analytical studies described in the previous section. The monofilar hub/arm assembly was similar to the bifilar hub assembly. Each of the monofilar arms had a four degree droop so that the vertical component of the centrifugal force of the dynamic mass will balance the vertical shear due to the weight of the mass.

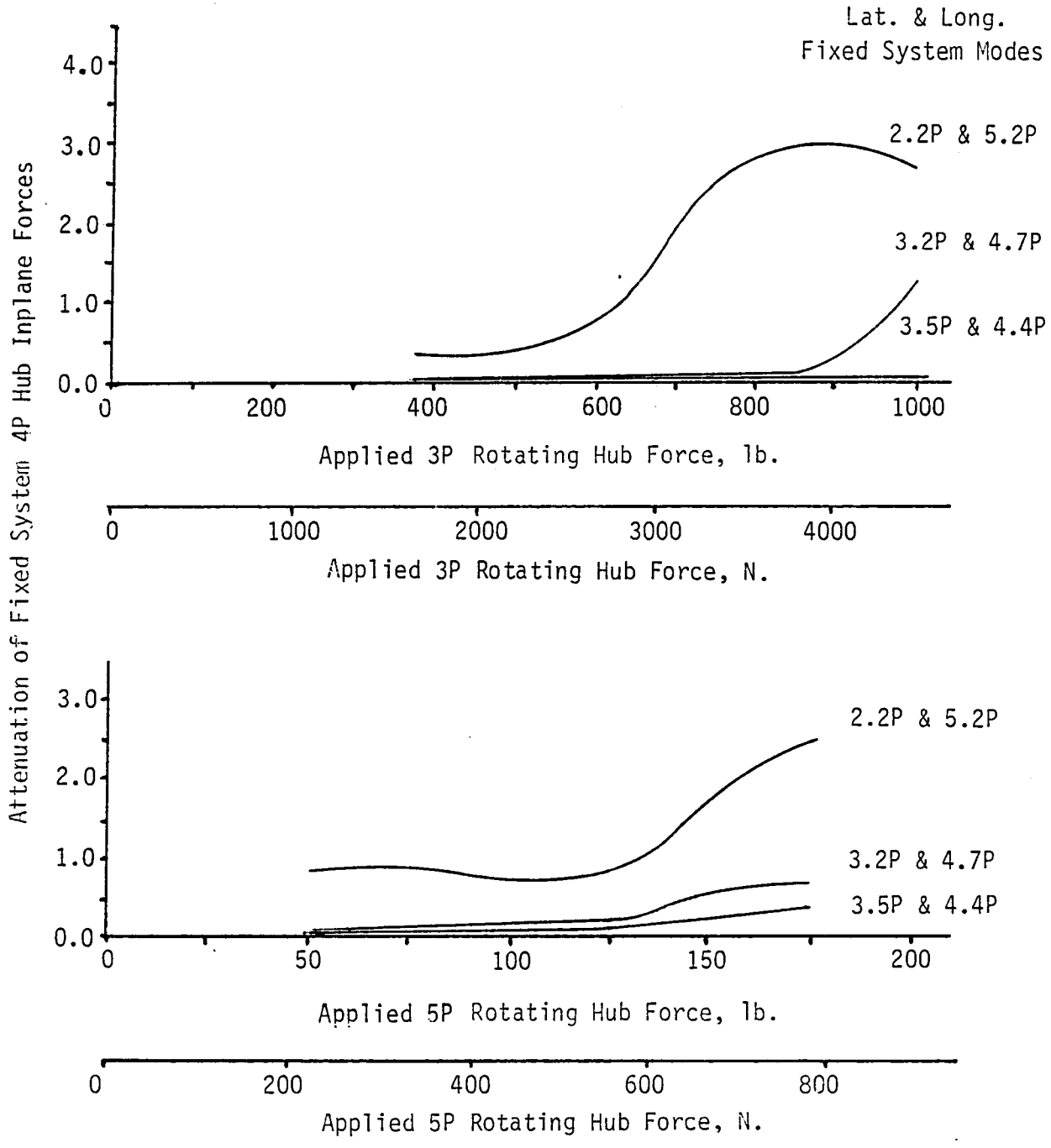

Figure 10. Monofilar Predicted Performance as a Function of Rotor Force Excitation for Various Hub Impedances.

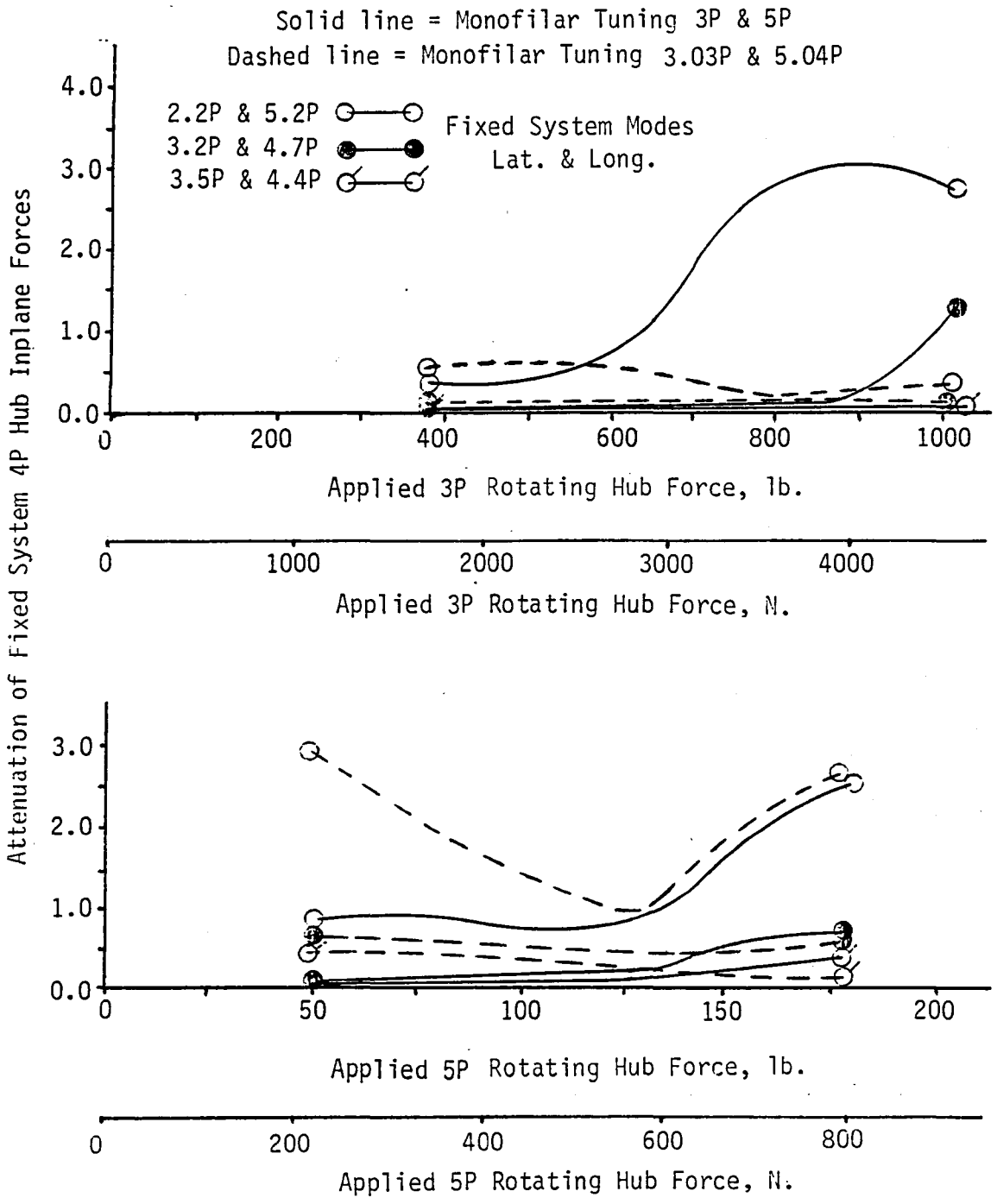

Figure 11. Effects of Over-Tuning on Predicted Monofilar Performance.

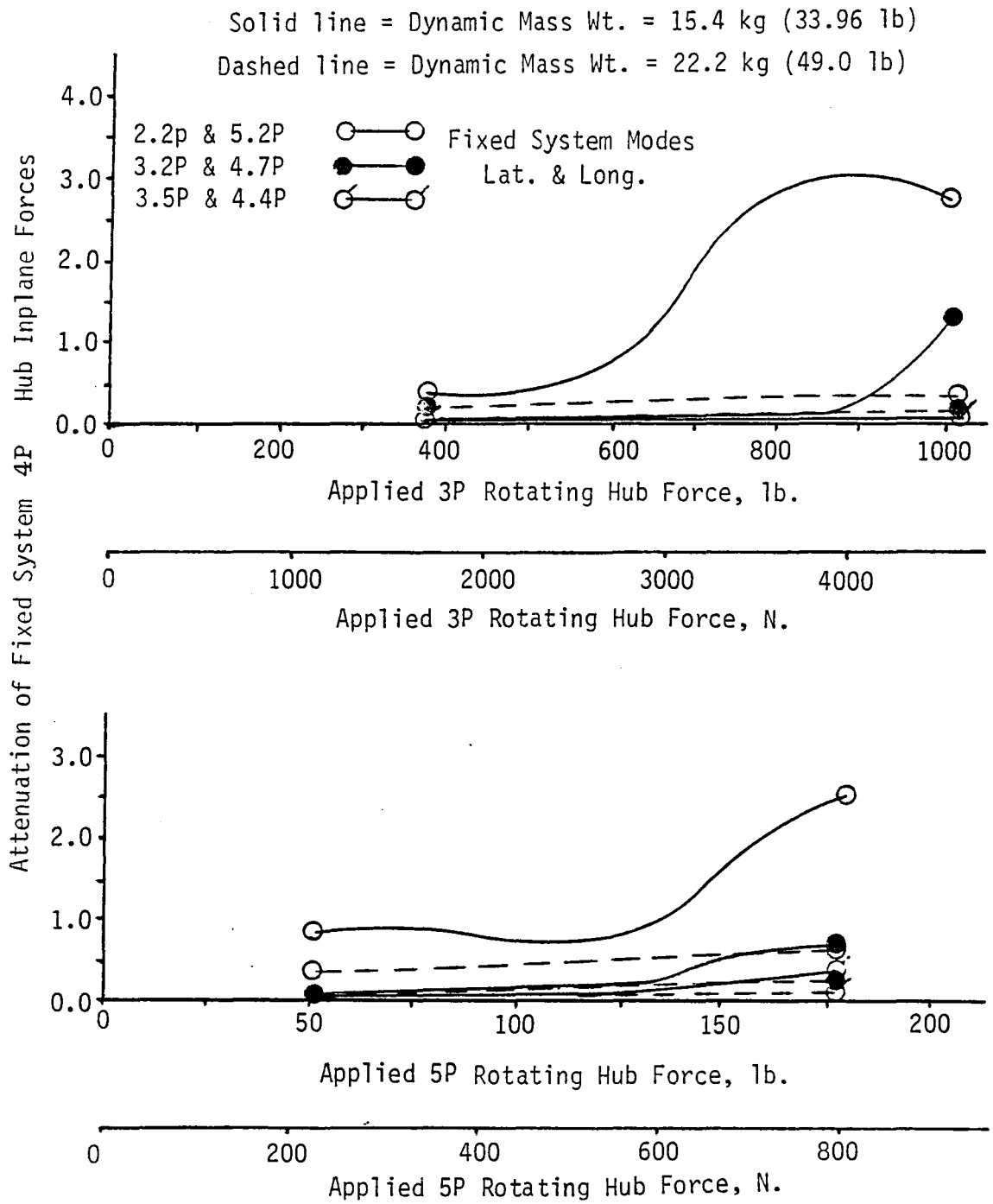

Figure 12. Effects of Dynamic Mass Weight Increase in Predicted Monofilar Performance.

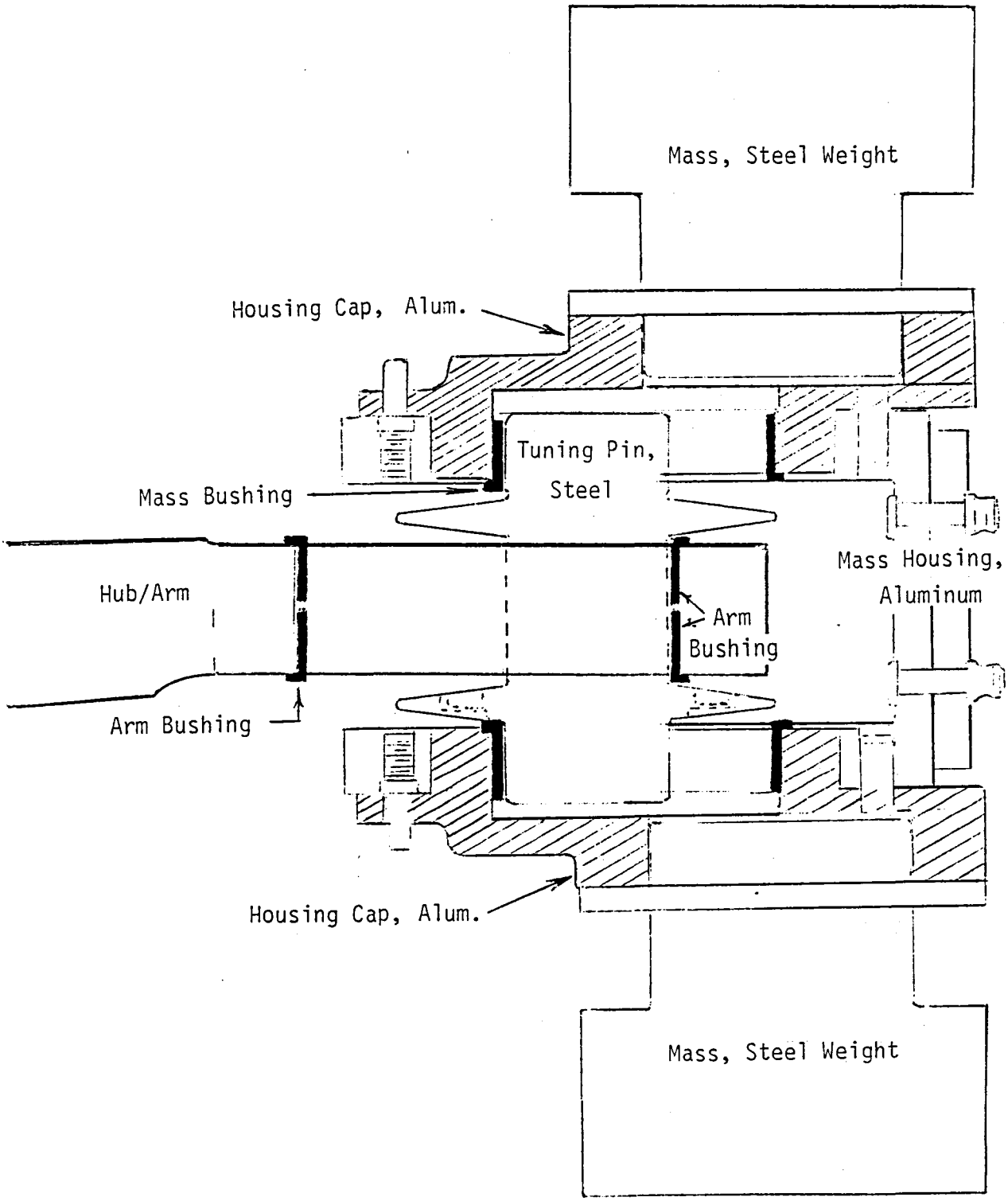

Figure 13. Monofilar Rotor Absorber Final Design Schematic.

The dynamic mass is comprised of three major components. An aluminum mass housing, top and bottom aluminum housing caps, and top and bottom steel weights. The mass bushings were press-fitted on the inside surface of each housing cap, while the steel weight was fitted on the outside surface. These steel weights are the primary control of the total weight and center-of-gravity offset for the monofilar design. The two housing caps were designed to be removable to facilitate assembly of the tuning pin to the hub arm and then the mass assembly to the tuning pin.

The steel tuning pins are of single piece construction except for the outer ring of the bottom flange. This ring was removable to facilitate assembly of the pin through the arm bushing of the monofilar hub. The properties of the final monofilar baseline design for a dynamic mass tuning of 3.0P and 5.0P were:

Dynamic mass, m = 15.4 kg (33.96 lb)

Inertia of dynamic mass, I = .03541 kg-m^2 (.3132 in.-lb-sec^2)

CG offset of dynamic mass, ΔR = .0394 m (1.55 in.)

Diameter of mass bushing, D_2 = .0691 m (2.721 in.)

Diameter of arm bushing, D_1 = .0984 m (3.874 in.)

Hub/arm length, R_o = .476 m (18.75 in.)

Tuning pin mass, m_p = 1.315 kg (2.90 lb)

Inertia of tuning pin mass, I_p = .000976 kg-m^2 (.00863 in.-lb-sec^2)

Diameter of tuning pin, d = .0445 m (1.75 in.)

The calculated 3P and 5P mode shapes, using the linear analysis, are shown in Figure 14. For the 3P mode, the motion was dominated by the rotation of the dynamic mass about the tuning pin with very little pin rotation. The 5P mode was primarily pin rotation with small motion of the dynamic mass about the pin. However, as shown, the resultant translation and rotation of the dynamic mass relative to its own axis for both modes create sufficient magnitudes of inertia force to react the 3P and 5P rotating excitations.

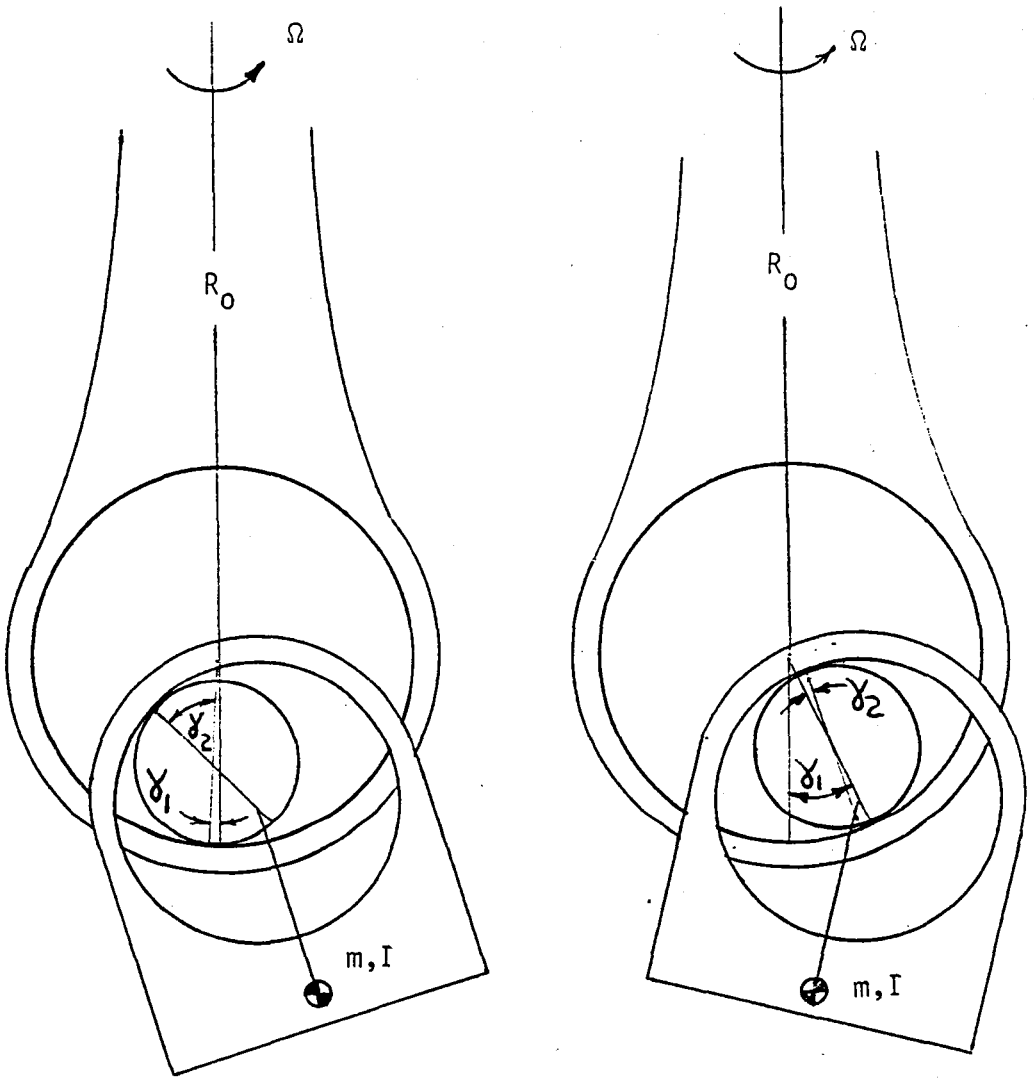

3P Mode Shapes

5P Mode Shapes

Figure 14. Monofilar Dynamic Mass Mode Shapes, Linear Analysis.

Figure 15 shows the fabricated monofilar dynamic mass components and tuning pin. Figure 16 shows the dynamic mass assembled with the tuning pin installed. Two additional sets of tuning pins were designed and fabricated. The first set will alter the 3P dynamic mass frequency to 3.03P and maintain the second mode frequency at 5.0P. The second set of pins will raise both modes of the baseline design to 3.03P and 5.04P, respectively. The properties of these pins are

	Set 1	Set 2
Tuning pin mass	1.839 kg (4.06 lb)	1.256 kg (2.77 lb)
Inertia of tuning pin	.001048 kg-m^2 (.00927 in.-lb-sec^2)	.000973 kg-m^2 (.00861 in.-lb-sec^2)
Diameter of tuning pin	.045 m (1.777 in.)	.045 m (1.777 in.)

An alternative absorber weight design was also fabricated. The total dynamic mass weight was increased to 22.2 kg (49 lb) by increasing the size of the top and bottom steel weights. For this configuration the tuning was placed at the baseline values of 3.0P and 5.0P by decreasing the mass bushing diameters by 3.4 percent.

Table 1 shows the weight breakdown of the monofilar parts and the total assembled weight for each dynamic mass and tuning pin. As shown the total weights are in very close agreement, less than 0.1 percent error.

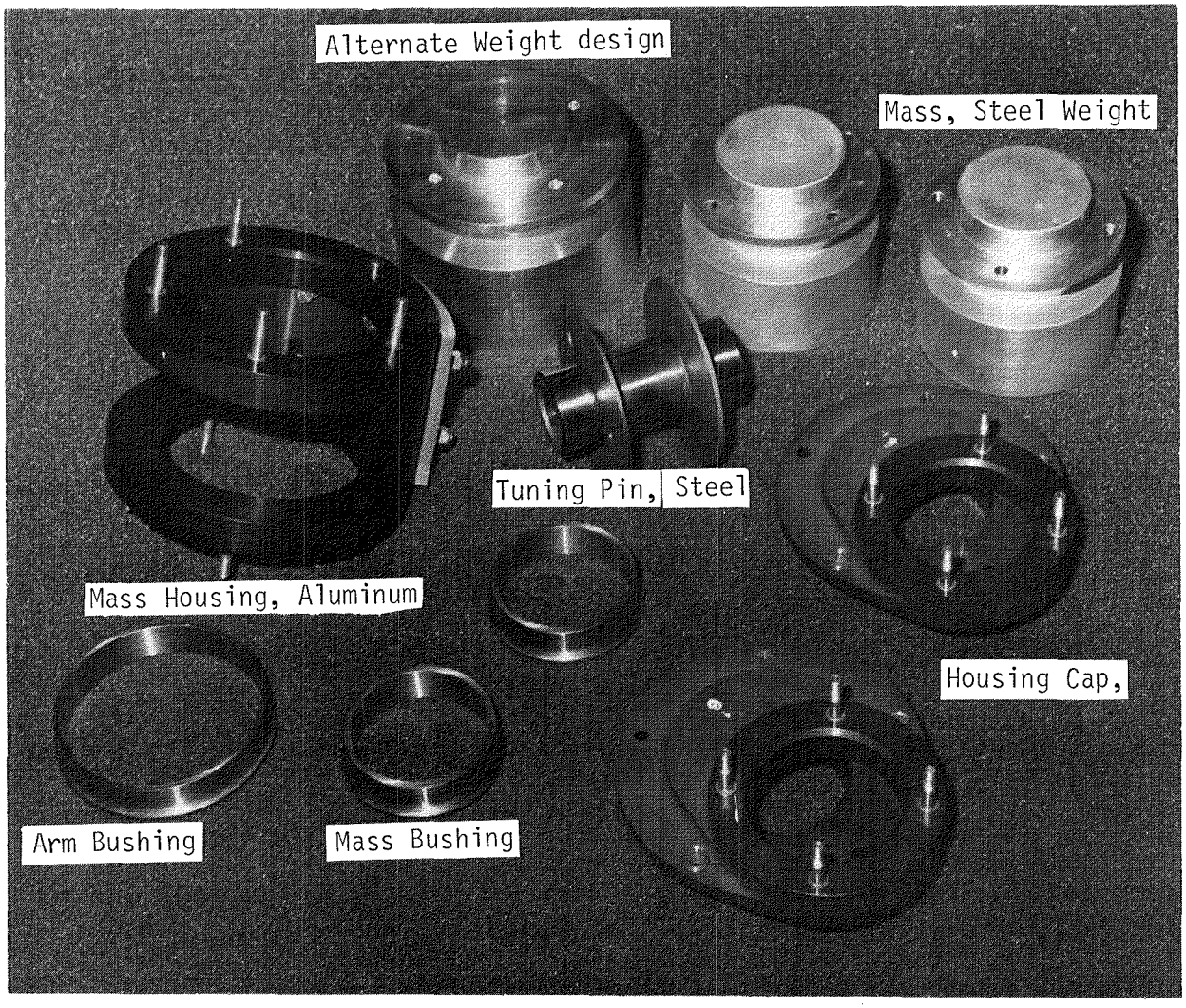

Figure 15. Monofilar Fabricated Parts.

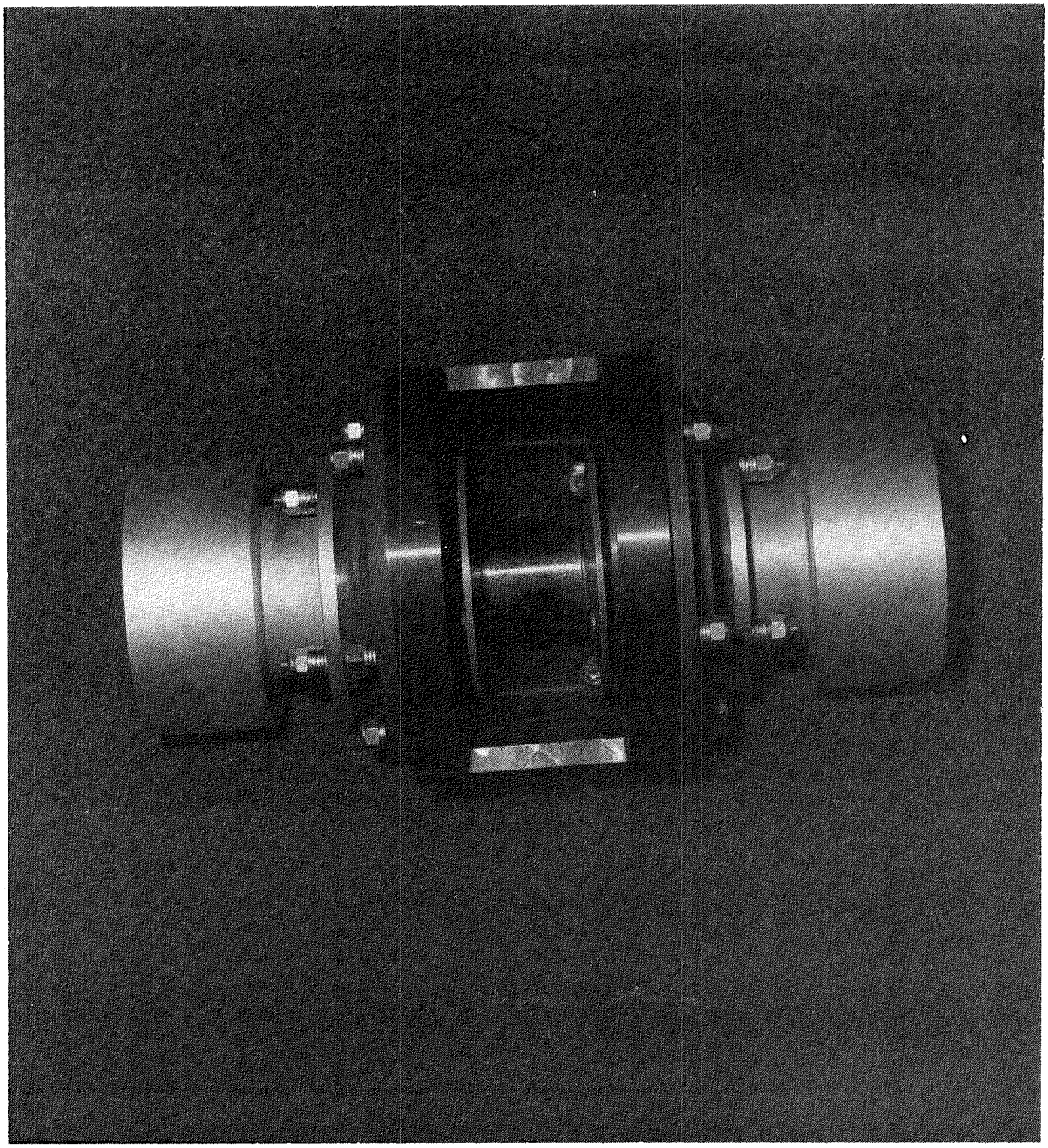

Figure 16. Monofilar Dynamic Mass and Tuning Pin.

Component	Dynamic Mass Assembly - (lb) #1	#2	#3	#4
Aluminum Housing	3.475	3.470	3.485	3.480
Steel Counterweight	1.840	1.835	1.840	1.835
Steel Housing Cap				
Top	2.070	2.070	2.060	2.060
Bottom	2.065	2.070	2.060	2.060
Steel Bushing				
Top	.220	.220	.220	.220
Bottom	.220	.225	.220	.220
Steel Weight Mass				
Top	11.840	11.820	11.820	11.840
Bottom	11.810	11.820	11.820	11.820
Hardware	.455	.455	.455	.455
TOTAL Dynamic Mass				
(lb)	33.995	33.985	33.980	33.990
(kg)	15.417	15.413	15.410	15.415

Component	Tuning Pin Assembly - (lb) #1	#2	#3	#4
Tuning Pin	2.555	2.557	2.562	2.562
Collar	.350	.348	.348	.342
TOTAL Tuning Pin				
(lb)	2.905	2.905	2.910	2.904
(kg)	1.317	1.317	1.320	1.317

TABLE 1. Monofilar Weight Breakdown

GROUND TEST

The monofilar was assembled and checked for all necessary clearances to assure proper operation. Initial testing consisted of supporting the monofilar hub on a bench such that the restoring spring was gravity in place of the normal centrifugal force. Using impact excitation, both dynamic mass modes were identified and defined. Next, the monofilar assembly was installed on a rotating absorber test facility, which tests the rotor absorber in a controlled environment that simulates hub forces and motions that are experienced on a helicopter in-flight. Using steady-state force excitation, the force response or the attenuation performance of the rotor absorber was measured. By varying the frequency of the excitation force, modal surveys of the dynamic mass were performed. To investigate these modal survey results, an eigenvalue analysis was developed to examine the monofilar mode shapes coupled with the fixed system modes.

Bench Impact Test

The test setup consisted of mounting the monofilar hub/arm assembly vertically to allow one dynamic mass/pin assembly to be installed and studied under 1g (gravity) force field. The hub was restricted so that the arm was basically cantilevered vertically off the lab bench, as shown in Figure 17. The purpose of this bench test was to examine the monofilar assembly under a simple test environment that would allow detail visual and measured observation of the dynamic characteristics of the arm, pin and mass assembly. Also, these tests provide early detection of problems before the initiation of more costly full scale ground testing.

The impact testing was conducted using an impact hammer, miniature accelerometer and digital analyzer. The test measured the mode shapes and natural frequencies of the monofilar dynamic mass assembly. Figure 18 shows the locations of the accelerometers that were used to define the mode shapes of the tuning pin and dynamic mass.

While testing the four dynamic mass assemblies and three sets of pins, it was necessary to have two assemblies shimmed to move the pair of mass bushings further apart to prevent binding on the pin flanges. This was caused by a very small error in stack-up dimensions and parallelism between the surfaces. Only a single shim per assembly was required and the shims were only .254mm (.010 inch) thick. This did not alter the frequencies or mode shapes of these assemblies.

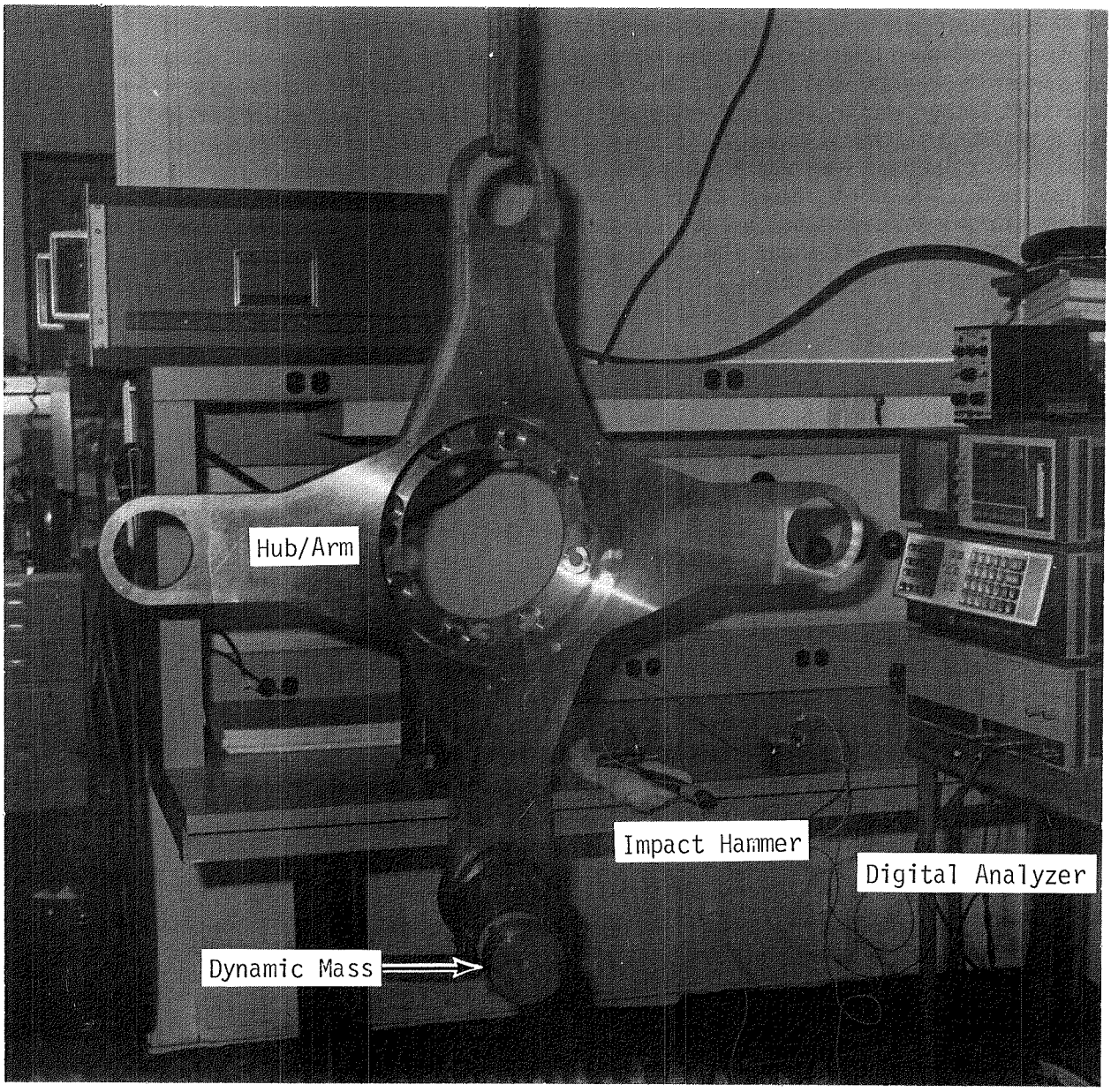

Figure 17. Monofilar Impact Bench Test Installation.

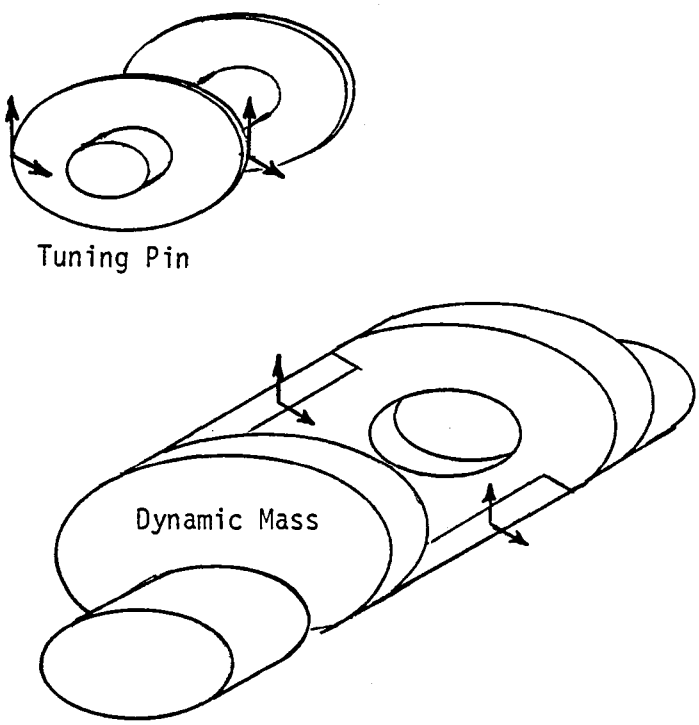

Figure 18. Monofilar Bench Impact Test Accelerometer Locations.

Figure 19 shows the results of the bench impact tests. The two degree-of-freedom system of the monofilar exhibits measured mode shapes and frequencies that show good correlation with predicted mode shapes and frequencies. As shown, the 3P mode consists of mostly mass motion, whereas the 5P mode has pin motion approximately twice the mass motion. Figure 20 shows the results of the measured transfer function (acceleration/force) from the impact tests for the four monofilar mass/pin assemblies. The results show that the natural frequencies for the four dynamic masses are nearly identical, and therefore, should provide similar response when excited by rotor forces. The impact tests also verified that the three sets of tuning pin designs altered the dynamic mass frequencies as predicted by the design tuning analysis. Figure 21 shows that the first alternative pin design only changed the 3P mode and that the second alternative pin design raised both the 3P and 5P modes.

Rotating Absorber Test Facility

The objective of the rotating absorber test stand was to provide a test environment that simulates a rotor absorber on an aircraft during flight. The full-scale rotating absorber test stand has three important advantages over aircraft testing.

1. The excitation force can be applied singularly at (N-1)P or at (N+1)P and at both frequencies simultaneously. Also, the forcing frequency and magnitude can be adjusted to any value.

2. The fixed-system dynamics representing the airframe hub impedance are well controlled. They can be set in the lateral, longitudinal and vertical directions to values which represent airframe dynamic characteristics of any aircraft.

3. The effectiveness of a rotor absorber design can be precisely defined. Single frequency attenuation levels can be measured as well as attenuation for dual frequency excitation.

This facility has been very successful for testing rotor absorbers. The test costs were estimated to be 8 to 10 times less than a similar flight test program. The rotating absorber test facility is shown schematically in Figure 22 and a photograph of the test stand is shown in Figure 23. The removable springs and masses that determine the fixed-system impedances are shown in Figure 24.

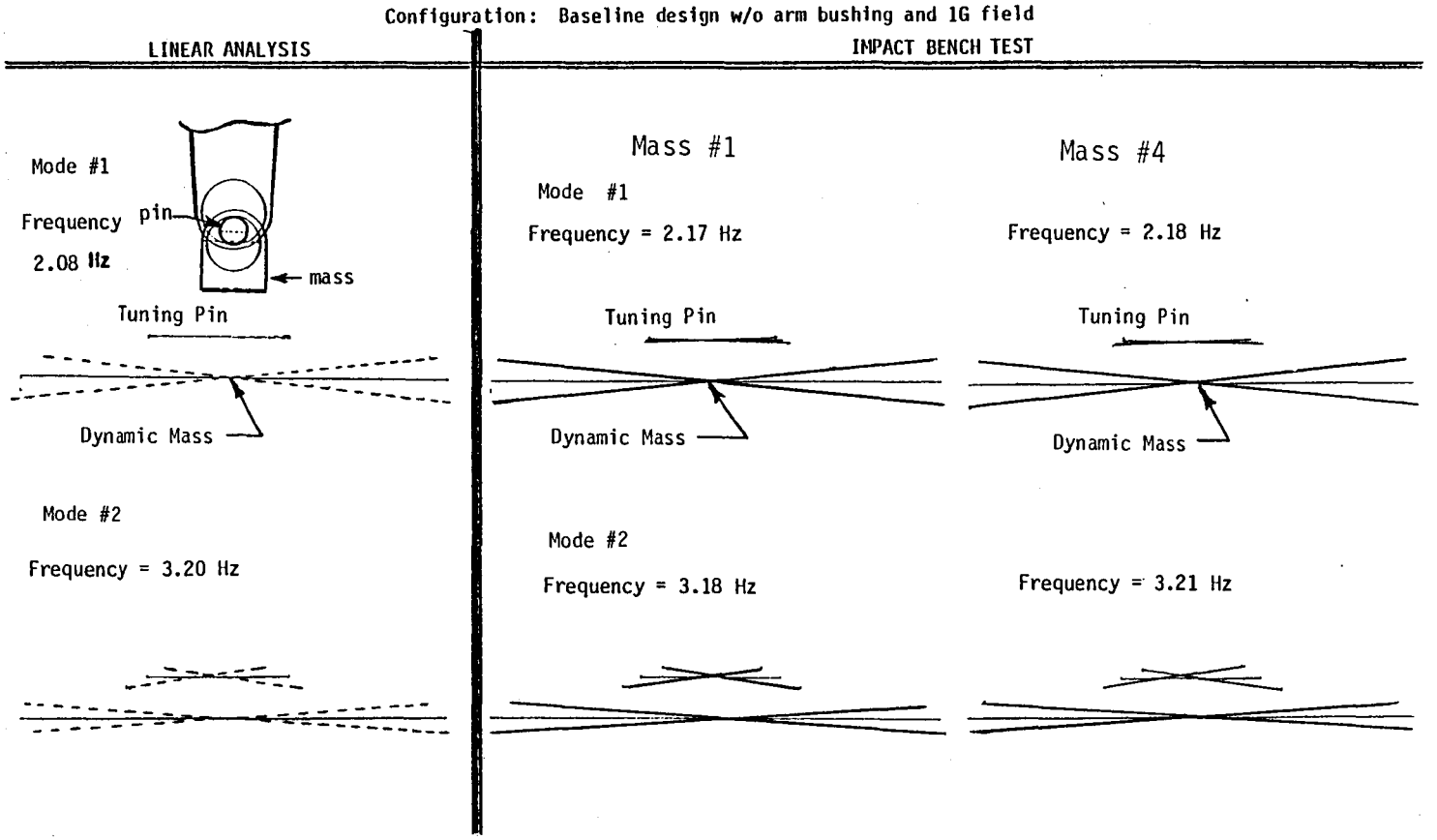

Figure 19. Monofilar Test Mode Shapes and Frequencies and Correlation with Analysis.

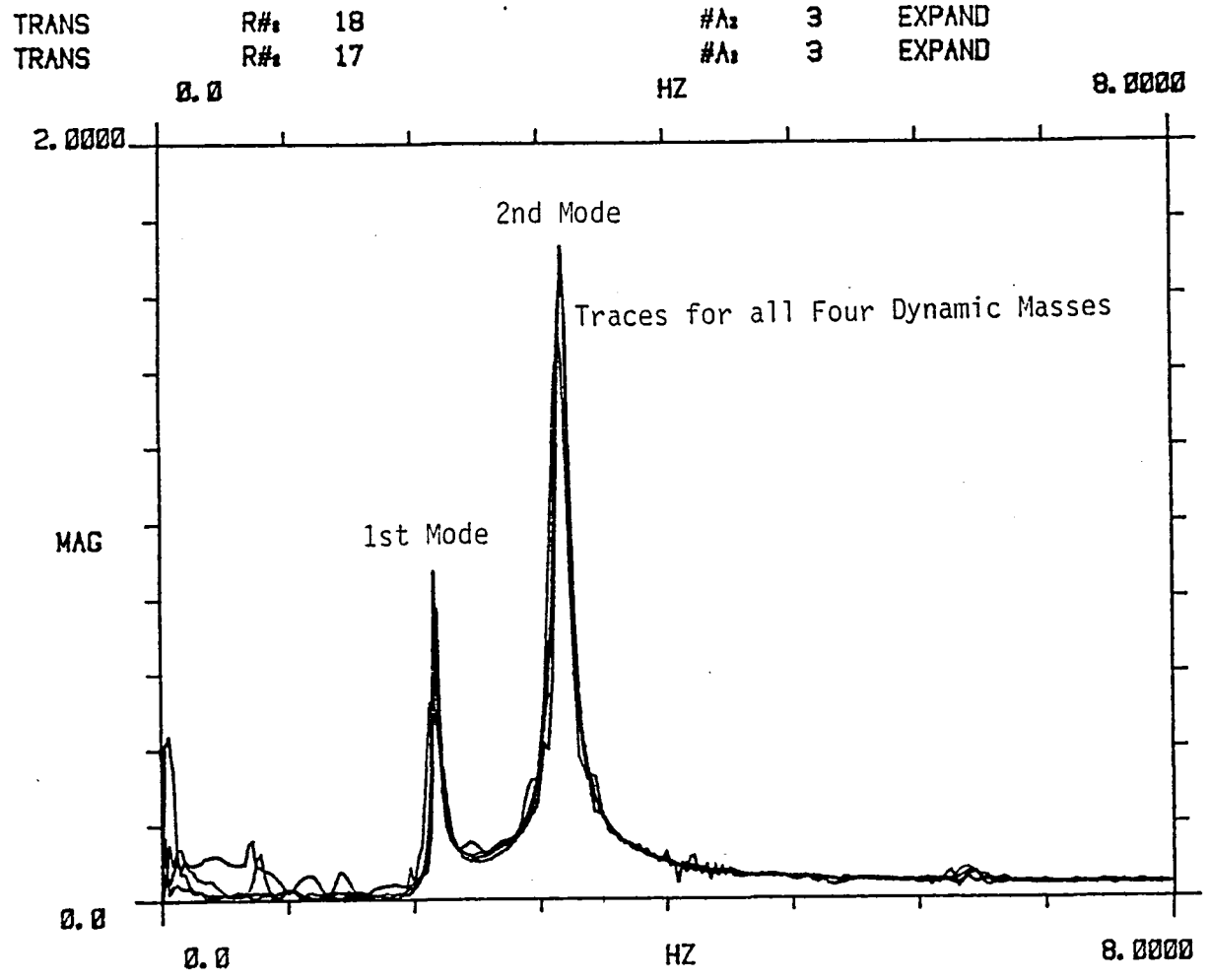

Figure 20. Impact Test - Dynamic Similarity of the Four Masses.

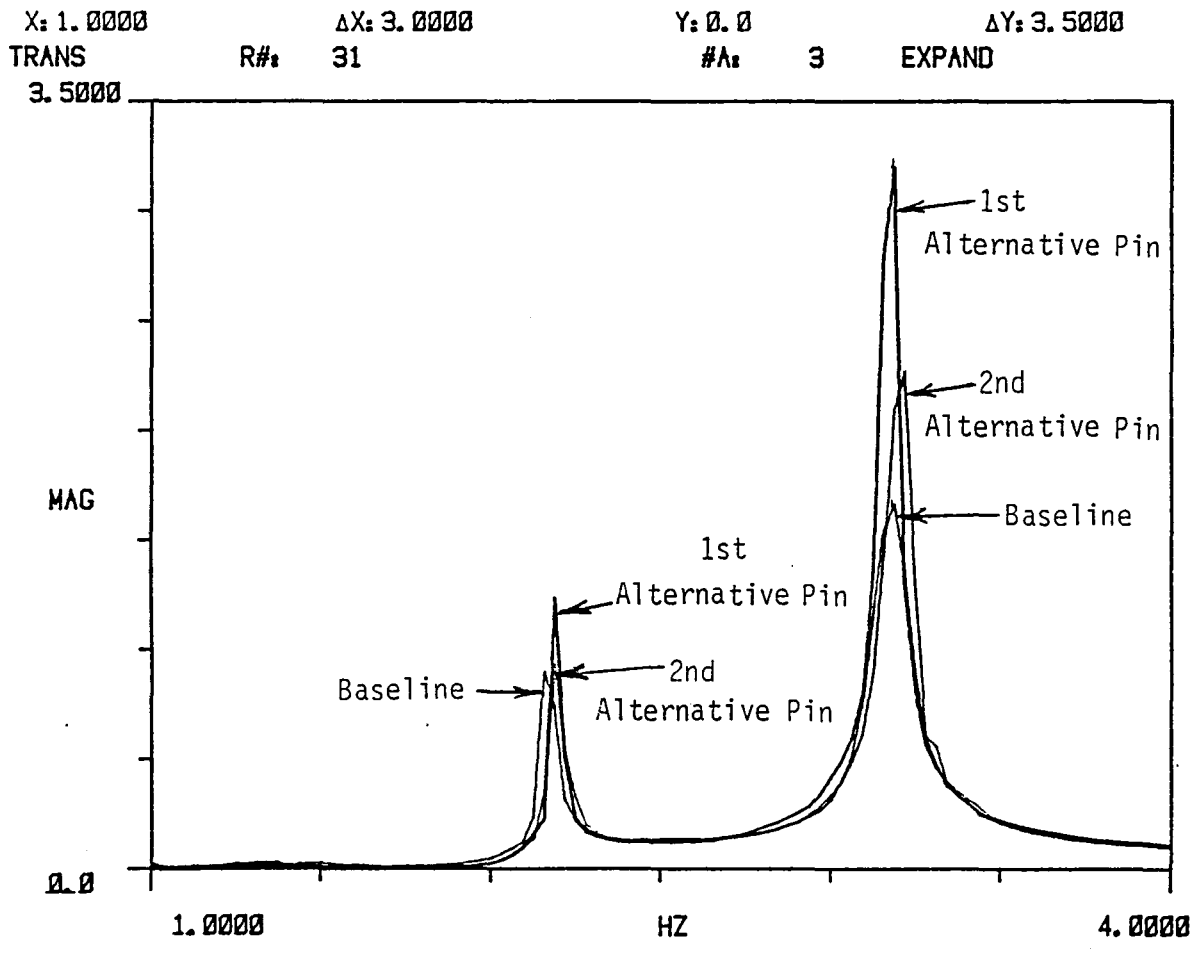

Figure 21. Impact Test Results of Three Sets of Tuning Pins.

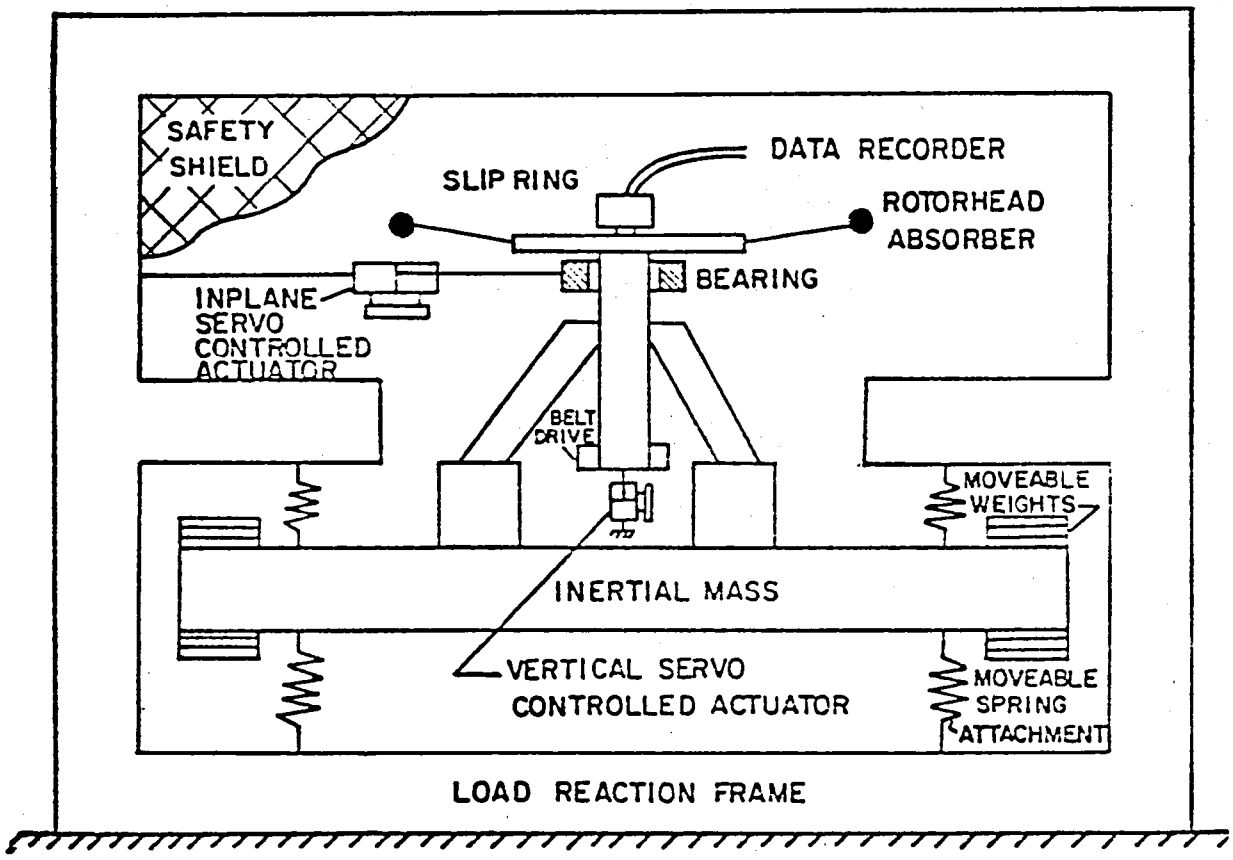

Figure 22. Rotating Absorber Test Facility Schematic.

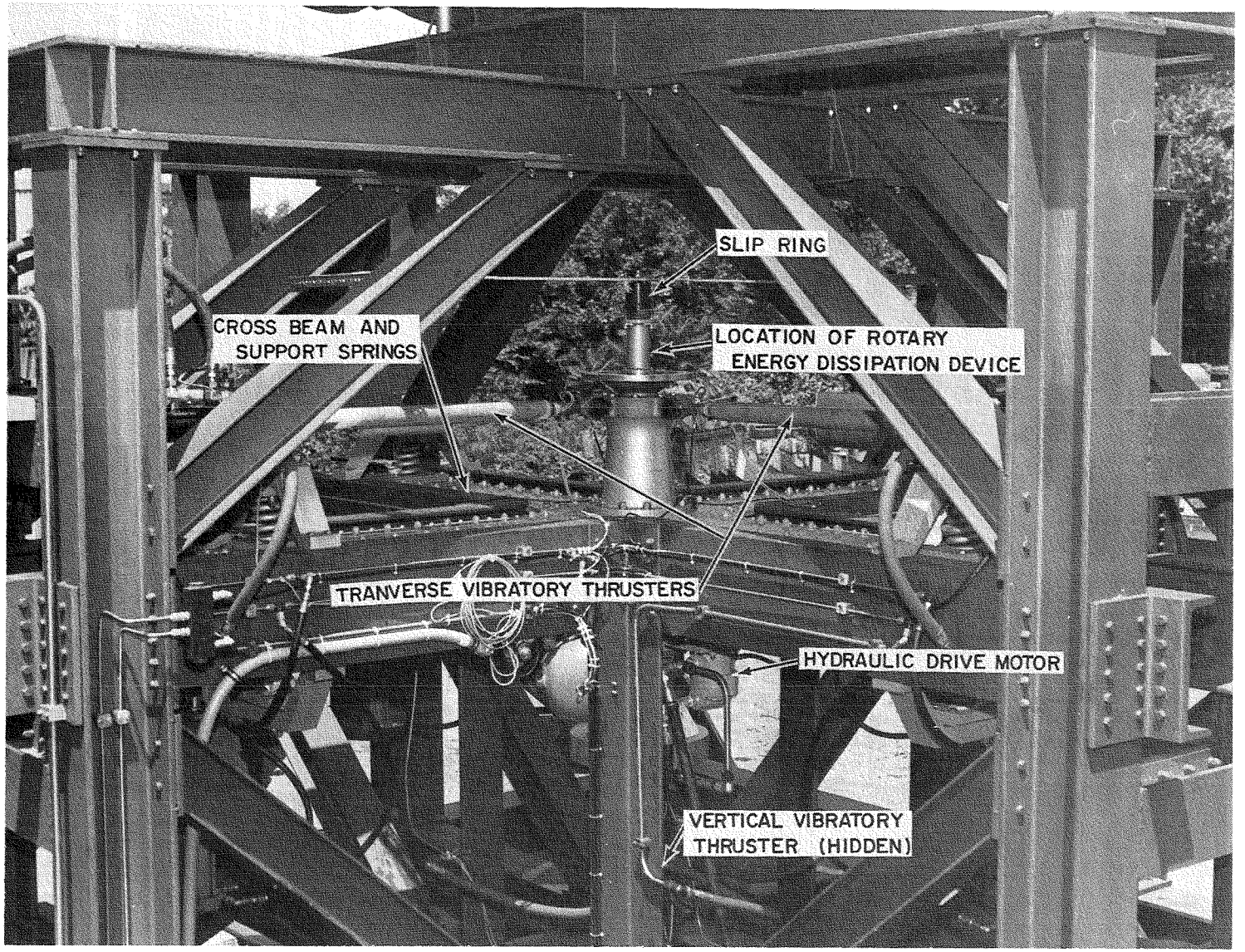

Figure 23. Rotating Absorber Test Facility and Components.

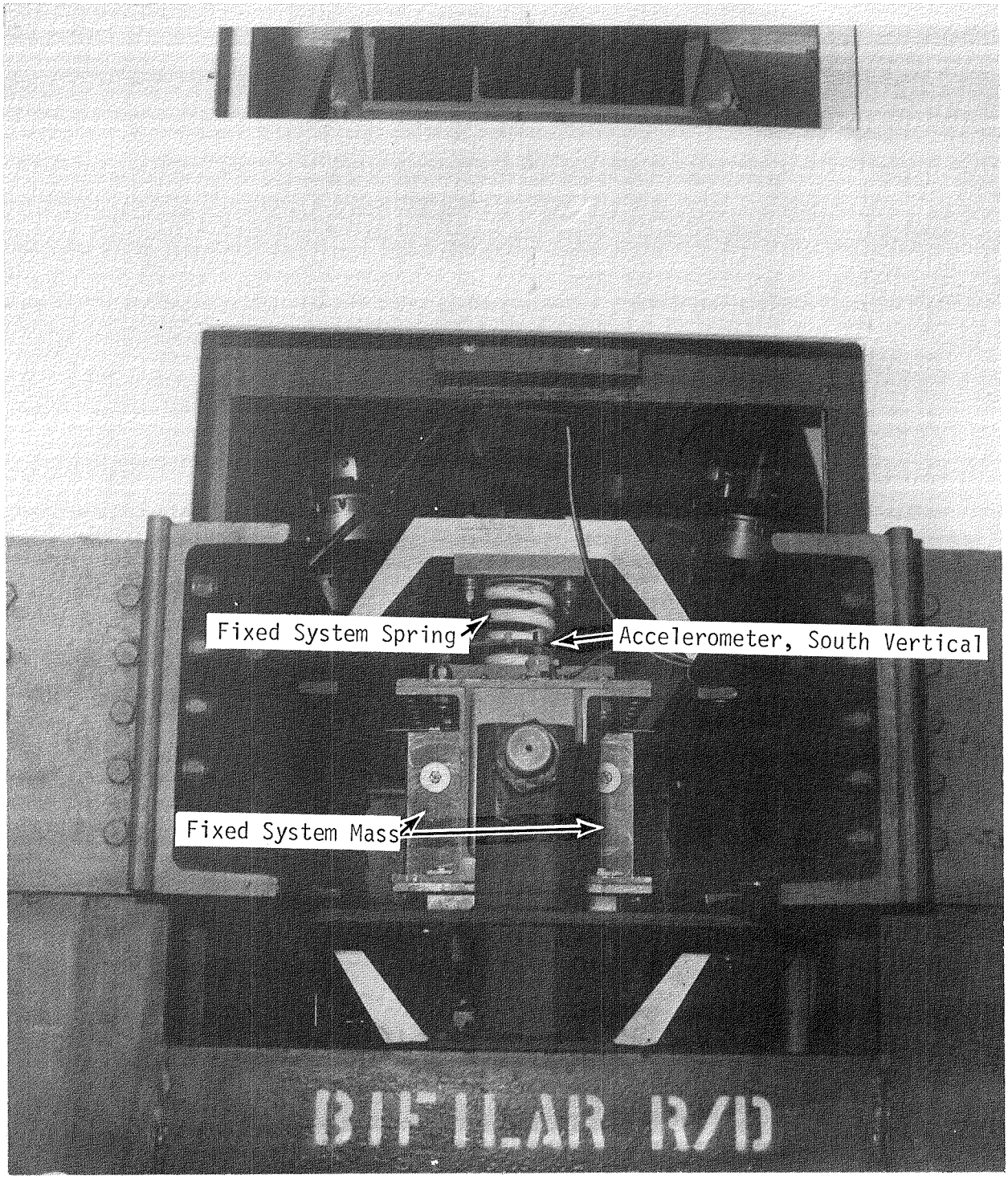

Figure 24. Test Stand Fixed-System Springs and Masses.

Rotor Absorber Ground Testing

Figure 25 shows the monofilar hub with dynamic masses installed on the rotating absorber test facility. As shown, a .051 meter (two inch) high spacer was installed at the base of the monofilar hub to provide the necessary clearance between the bottom of the dynamic masses and the top of the fixed system input force excitation rods. Also shown are the accelerometer pickup locations on the dynamic masses, hub arms and the facility stand hub. The measurements included:

A. Fixed-system measurements

   1. Hub lateral and longitudinal accelerations.

   2. End or cross beam tip vertical accelerations.

   3. Lateral and longitudinal hub excitation forces.

B. Rotating-system measurements

   1. Monofilar outer arm radial and tangential accelerations (all four arms).

   2. Monofilar mass housing tangential, radial leading edge and radial trailing edge accelerations (all four masses at ΔR = .0152 m (.60 in.) and a radius .0923 m (3.68 in.).

For the monofilar tests, the rotating absorber test facility was configured to represent the UH-60 helicopter. Representative values for lateral and longitudinal hub impedances were defined based on the airframe shake test. A test stand spring/mass combination was chosen to simulate these properties. Figure 26 shows the test stand dynamic characteristics as matched to the UH-60 measured lateral and longitudinal impedances.

Critical to a successful study of the dynamic characteristics of a rotor absorber was the ability of the test facility to provide single frequency excitations in the rotating system. The stand provides either (N-1)P or (N+1)P excitations and excitation at any frequency while holding rotor speed constant. Figure 27 illustrates that for a (N-1)P or (N+1)P excitation of the monofilar with the dynamic masses and pins removed, the motion of each of the arms moved with the correct frequency, i.e. 3P and 5P and the magnitude of response was the same for either excitation frequency.

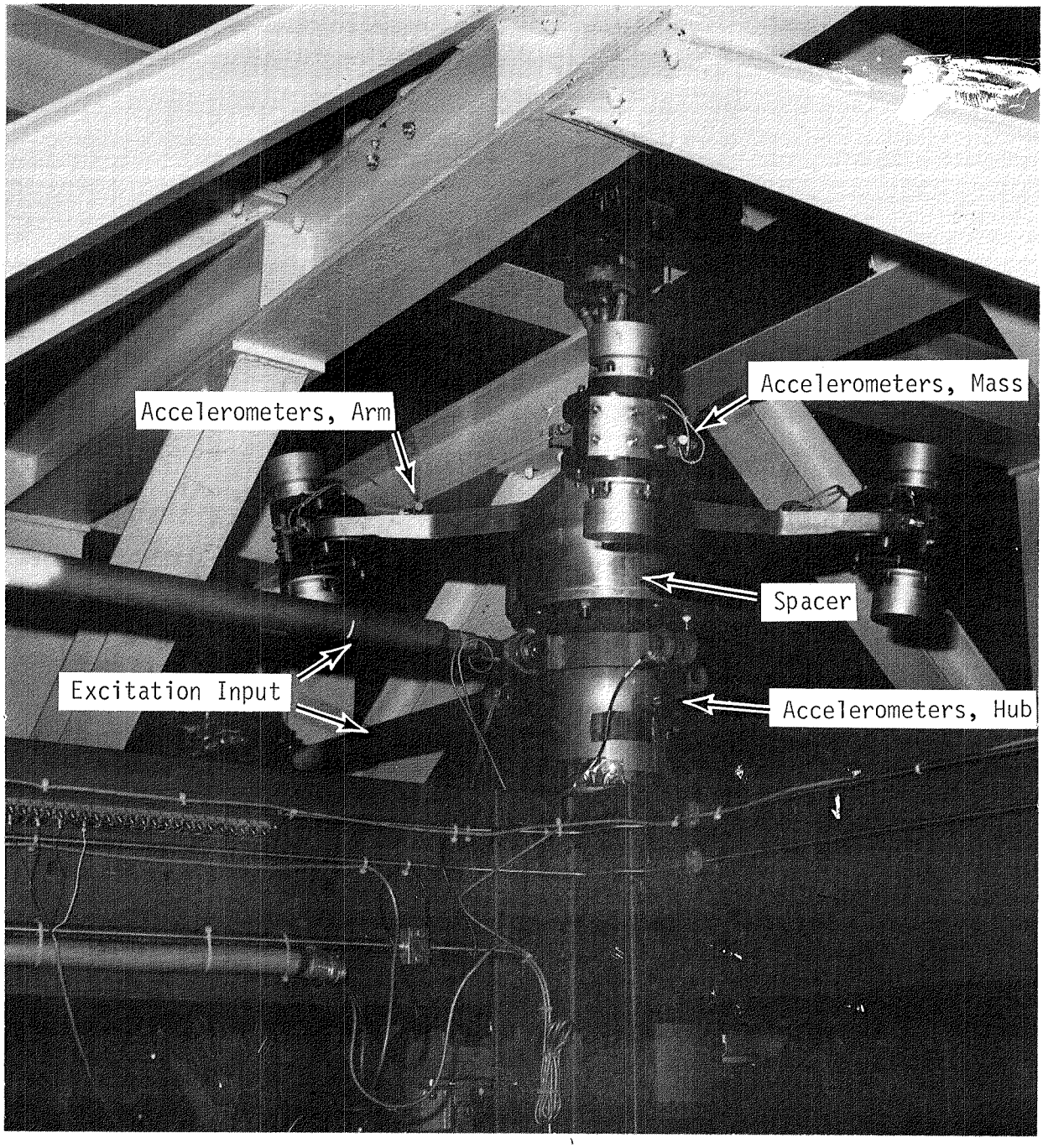

Figure 25. Monofilar Absorber Installed in Ground Test Facility

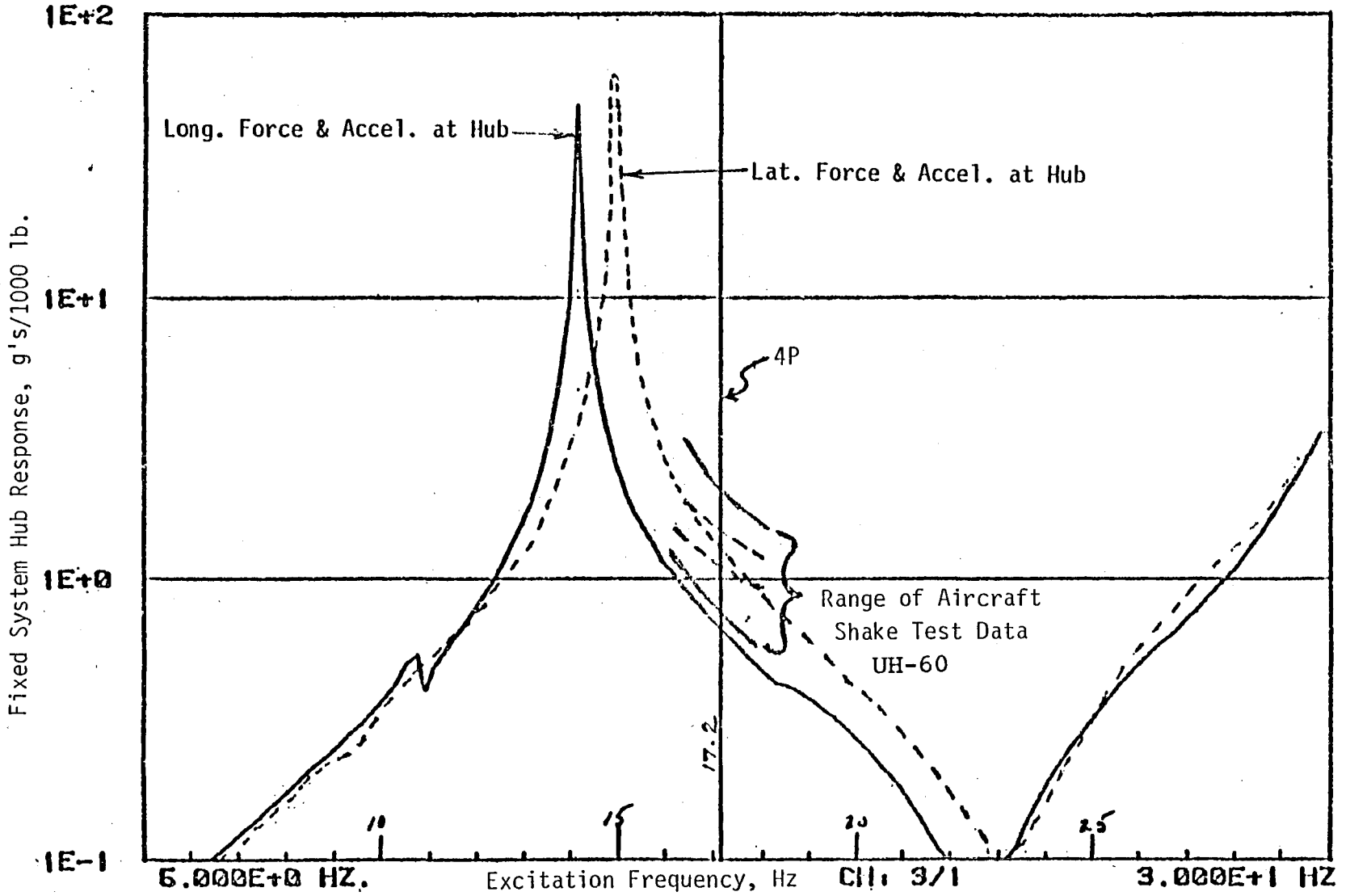

Figure 26. Rotating Absorber Test Stand Dynamic Characteristics as Matched to the UH-60 Data

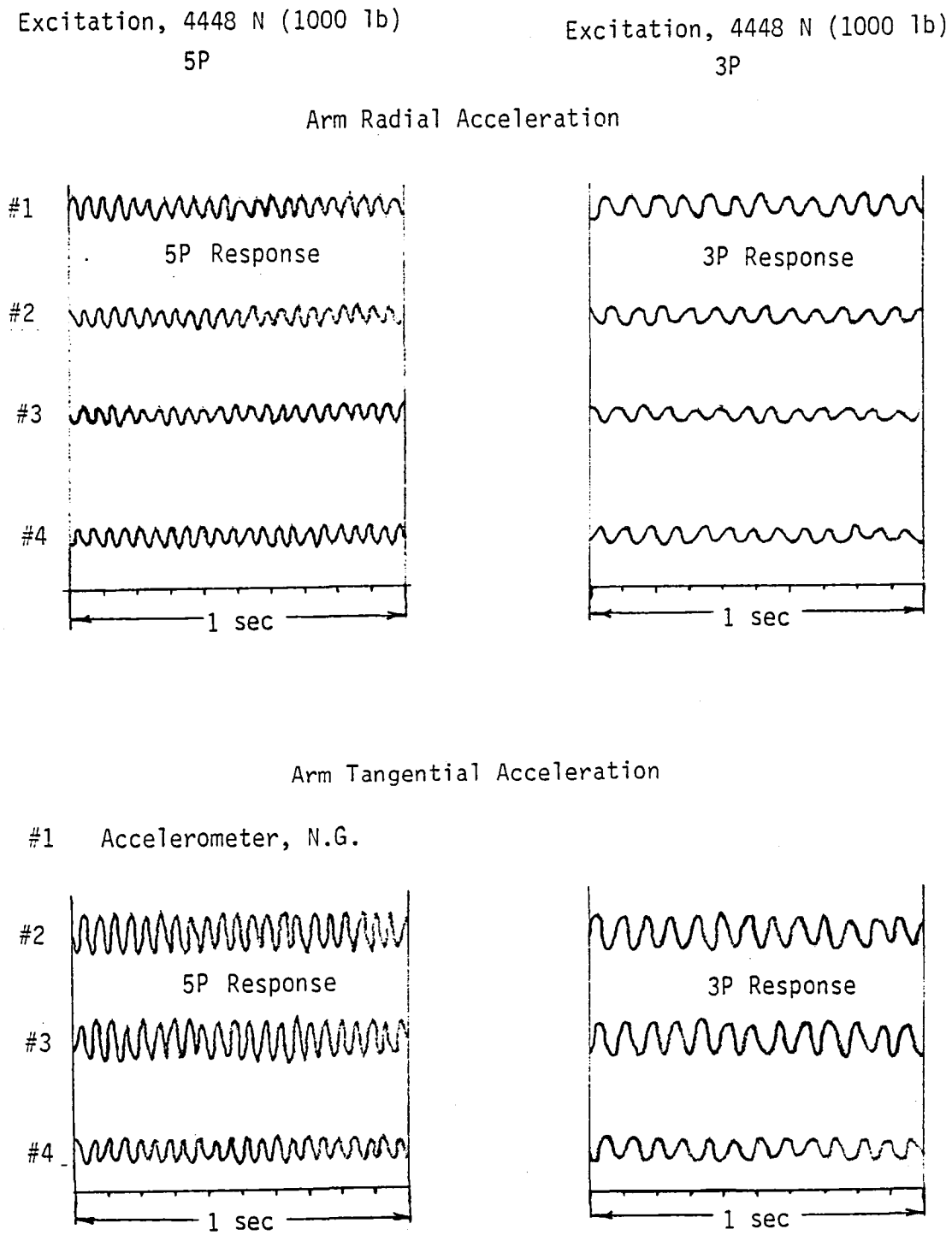

Figure 27. Monofilar Arm Response for (N-1)/rev and (N+1)/rev Excitations.

For the monofilar baseline design, the performance of the absorber was measured as a function of applied rotor excitation. The baseline design consisted of the 15.4 kg (33.9 pound) dynamic mass and the tuning pin for 3.0P and 5.0P tuning. The monofilar performance characteristics are shown in Figure 28. Presented are the fixed system 4P hub lateral and longitudinal response with and without the monofilar. For the monofilar excited by 3P forces, the attenuation of fixed system response was 60 to 80 percent. When the 3P excitation increased to the test stand limit, 11120 N (2500 lb), the attenuation remained the same. This force excitation level exceeded the maximum UH-60 flight load, which is 6672 N (1500 lb) at 150 kts.

The monofilar dynamic mass motions are shown in Figure 29 for excitation levels up to 11120 N (2500 lb) of 3P and 3558 N (800 lb) of 5P. As shown, the four dynamic masses performed very similarly at each level of excitation. Compared to the bifilar, the monofilar mass motion has much less dissimilarity. This result indicates that the monofilar dynamic properties, vary less than the bifilar. This less variance of dynamic mass motion is beneficial because it reduces the potential for non-4P vibration introduced into the fixed system (airframe) from the rotor absorber response.

Also shown in Figure 28 is the monofilar performance for 5P excitation. For this excitation, the attenuation of the fixed system hub response was approximately 40 percent. Accounting for the increase in hub impedance due to the addition of dynamic masses, an approximate 23 percent attenuation will result from adding weight only. This implies that the 5P attenuation was relatively low. Correlated to this low 5P performance were the results from the monofilar modal frequency survey. The survey was performed by holding the excitation level constant at 445 N (100 lb), fixing the rotor speed at 100% N_R (4.3 Hz), and first phasing the fixed-system excitation forces to give a (N-1)P rotating excitation. The system response was then recorded as the excitation frequency was varied. Then a similar test was performed with a (N+1)P rotating excitation force.

As shown in Figures 30 and 31 the forced response identified <u>two</u> monofilar modes when excited by the (N-1)P rotating force and, unexpectedly, only one monofilar mode, the lower mode, when excited by the (N+1)P rotating force. This absence of monofilar modal response when excited by the (N+1)P rotating force explains the small 5P attenuation performance of the monofilar.

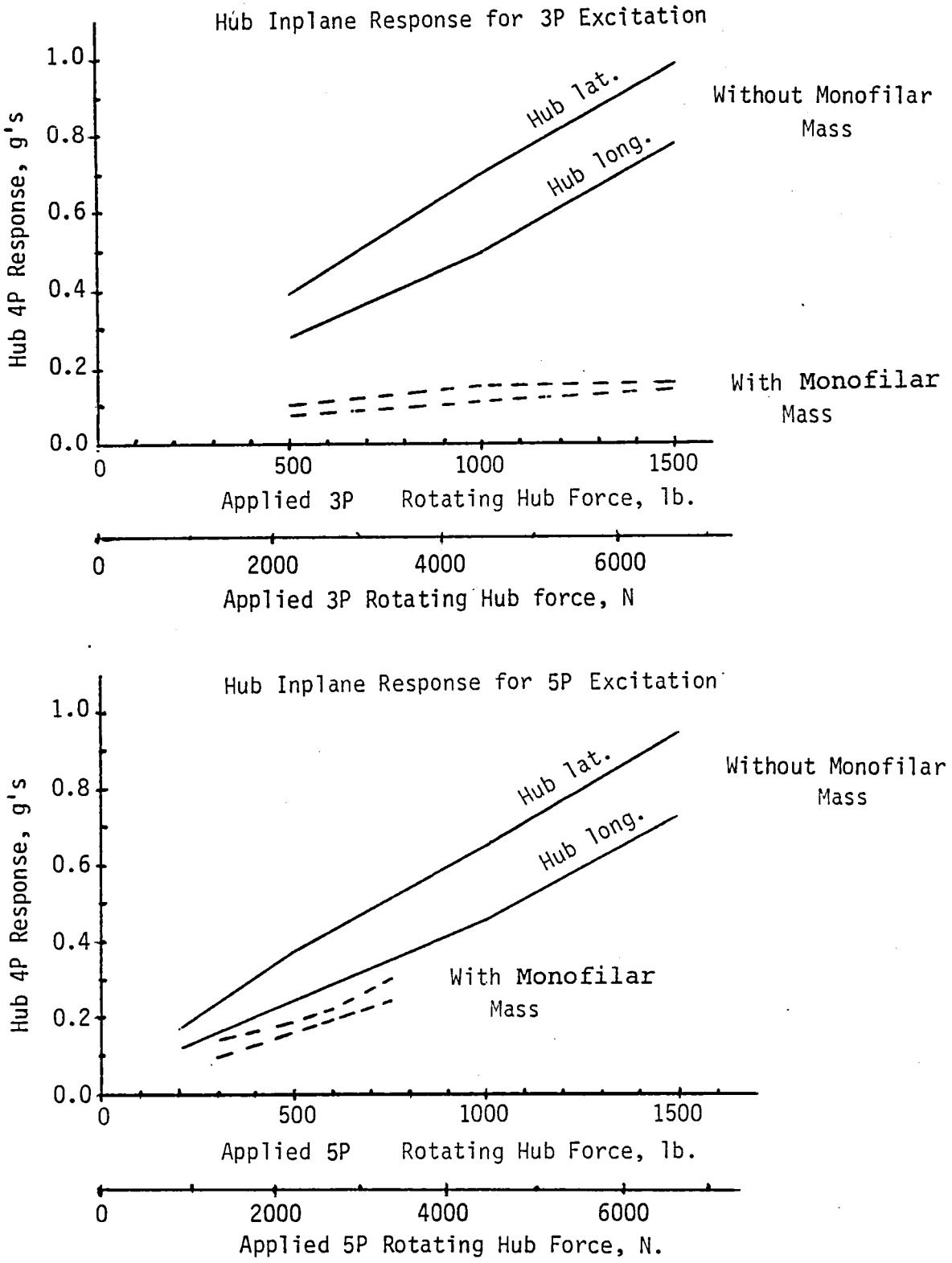

Figure 28. Monofilar Performance on Ground Test Stand.

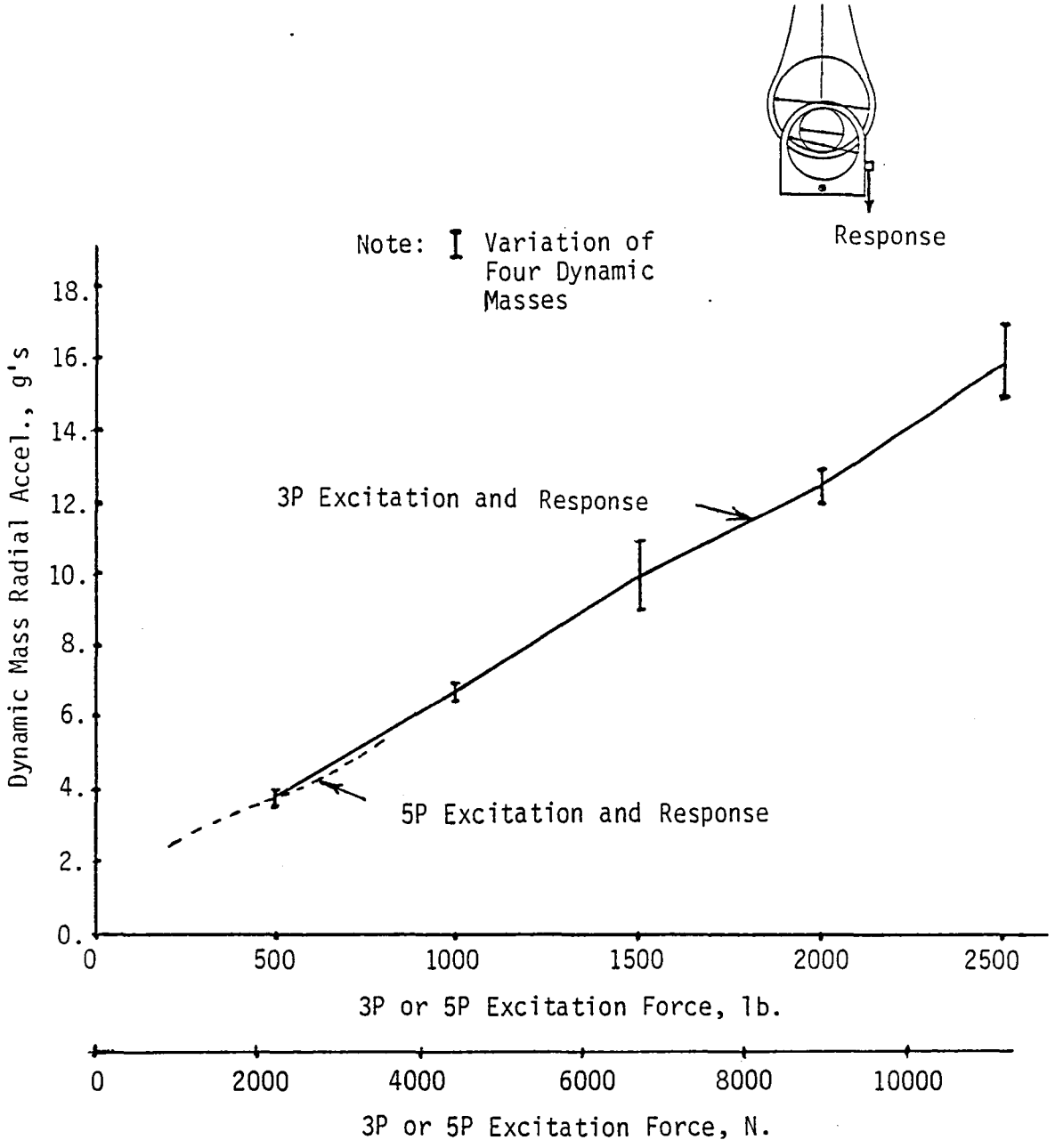

Figure 29. Monofilar Dynamic Mass Response for 3P or 5P Excitation.

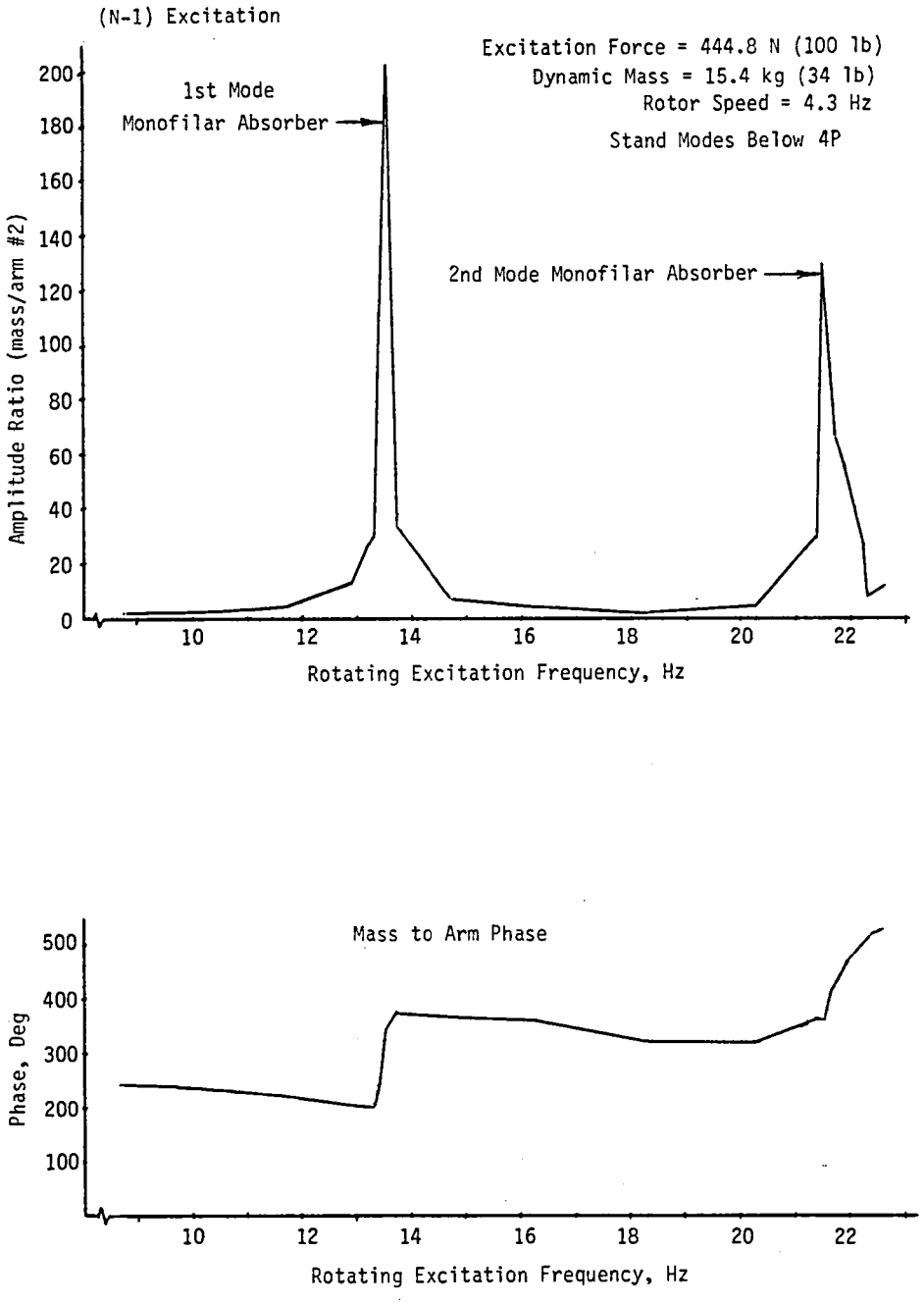

Figure 30. Modal Survey for (N-1)P Excitation, Stand Modes below 4P.

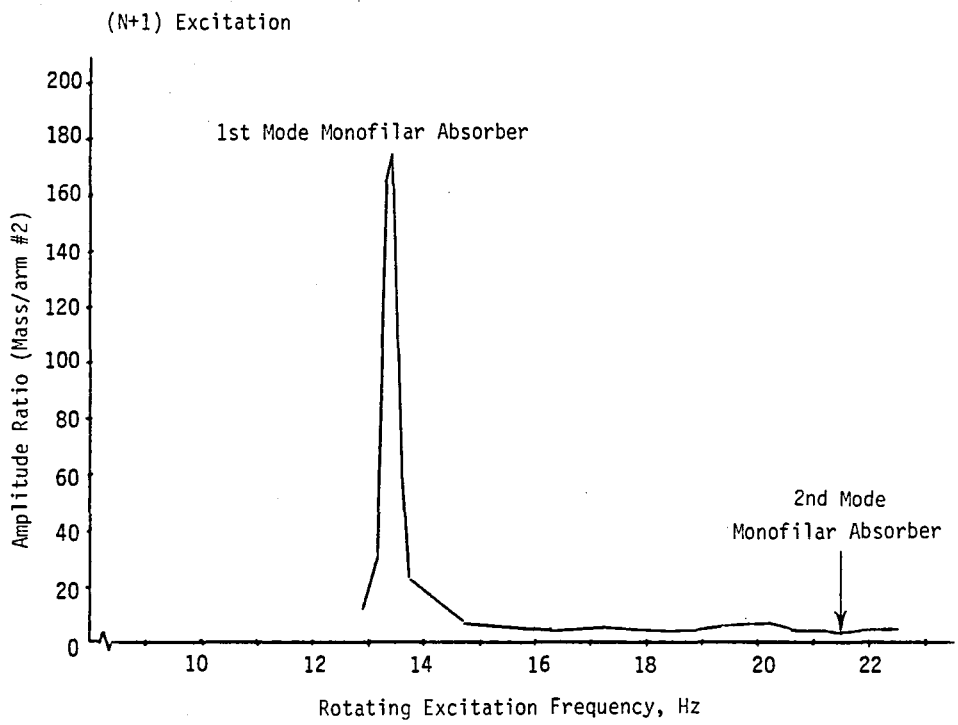

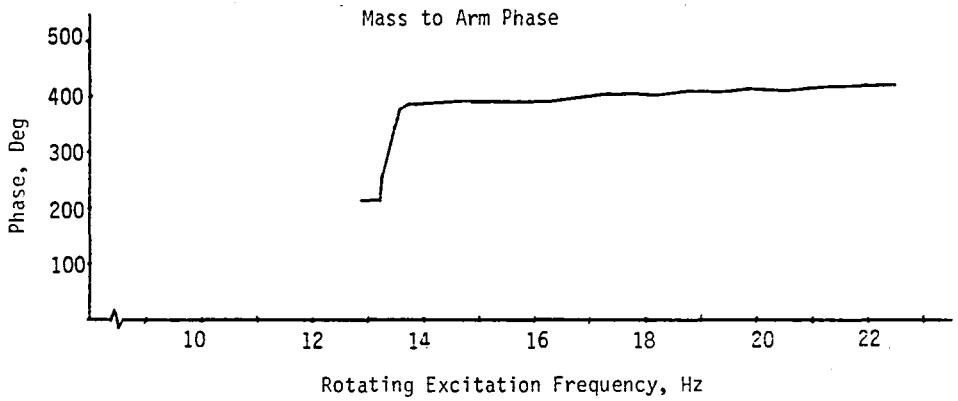

Figure 31. Modal Survey for (N+1)P Excitation, Stand Modes below 4P.

To study the effects of fixed-system impedance on monofilar response, the test stand fixed-system modes were raised above 4P (17.2 Hz) by replacing the test stand support springs with stiffer springs. This raised the fixed-system modes (lateral and longitudinal) from 14.8 Hz and 14.2 Hz to 21.6 Hz and 22.3 Hz respectively as shown in Figure 32. For this test configuration the results of a similar modal survey test are shown in Figures 33 and 34. As before, the 3P monofilar mode was excited for both the (N-1)P and (N+1)P force excitations. However, the 5P mode, which was previously excited with (N-1) force excitation and stand modes below 4P, could not be excited with either excitation. An effort to measure the monofilar 3P and 5P performance (attenuation) for this configuration was halted when at a third test point of 1779 N (400 lb) of (N-1)P force produced excessive vibrations (heard as loud clattering). This performance test was terminated to avoid damage to the absorber hardware.

To understand this anomally, the test stand modes were returned to baseline configuration (modes below 4P). The frequency survey was repeated and the 5P mode did not respond with either (N-1)P or (N+1)P excitation. Performance testing was stopped because of excessive vibration at 3558 N (800 lb) of 3P force.

With an alternative tuning pin installed, designed for tuning of 3.03P and 5.0P, the performance test was stopped due to vibration at 1779N (400 lb) of 3P force. This tuning pin had been modified by removing material on the inside surfaces of the flange to increase clearance by .25mm (.010 in.) over baseline pins, as shown in Figure 35.

Examination of the tuning pins (3.0P and 5.0P configuration), revealed galling on their rolling surfaces (see Figure 36). Material was also being removed from the inside root surfaces of the tuning pin flanges (see Figure 37). Along with the wear of the pin was the wear of the top outside edges of the arm bushing and the mass bushing. Figure 38 shows the wear of the mass bushings. An overall schematic summarizing the wear patterns of all the components is shown in Figure 39.

This evidence indicated that the monofilar dynamic mass was rocking torsionally about a radial axis perpendicular to the hub arm bushing and the inside root pin flange resulting in added friction due to the pin rotation. As shown earlier, the 5P mode shape has ten times the pin-rotation-to-mass-motion ratio than the 3P mode. While the 3P mode was not significantly affected by the rocking motion of the dynamic mass, the 5P mode was much reduced. This torsional motion of the mass relative to the support arm was believed to result from two sources. The first was the small

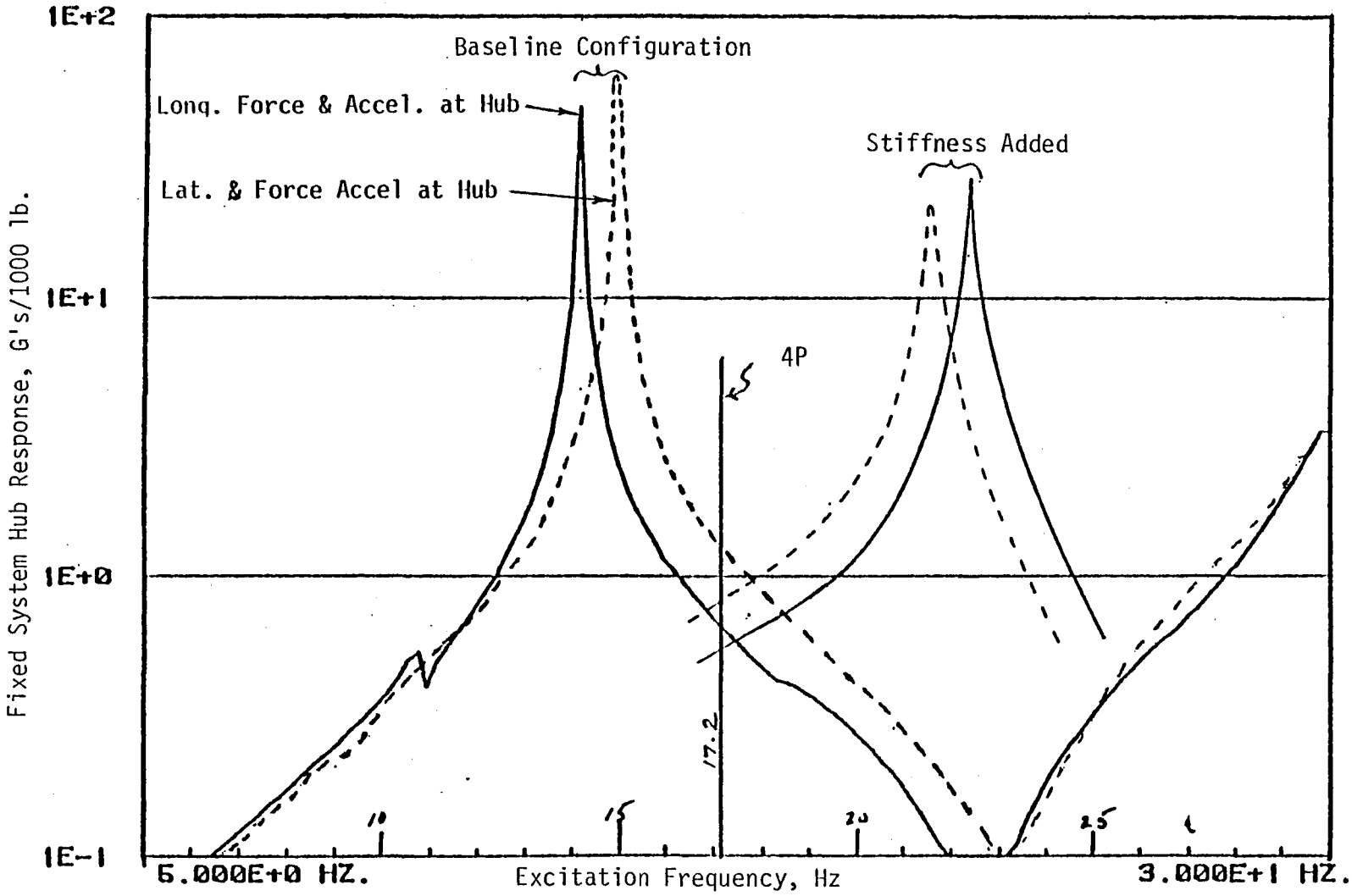

Figure 32. Test Stand Response with Stiffer Springs.

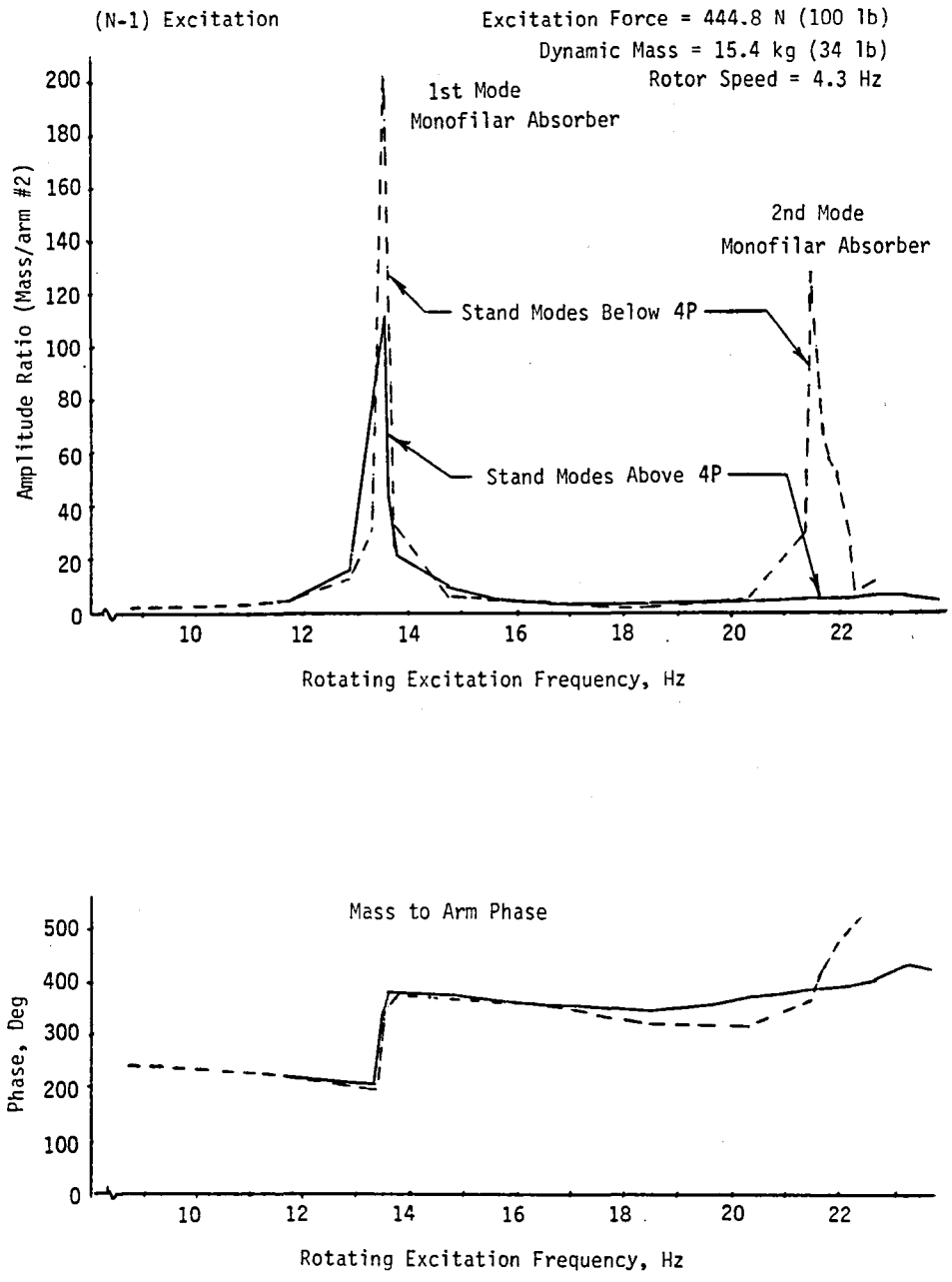

Figure 33. Modal Survey for (N-1)P Excitation, Stand Modes above 4P.

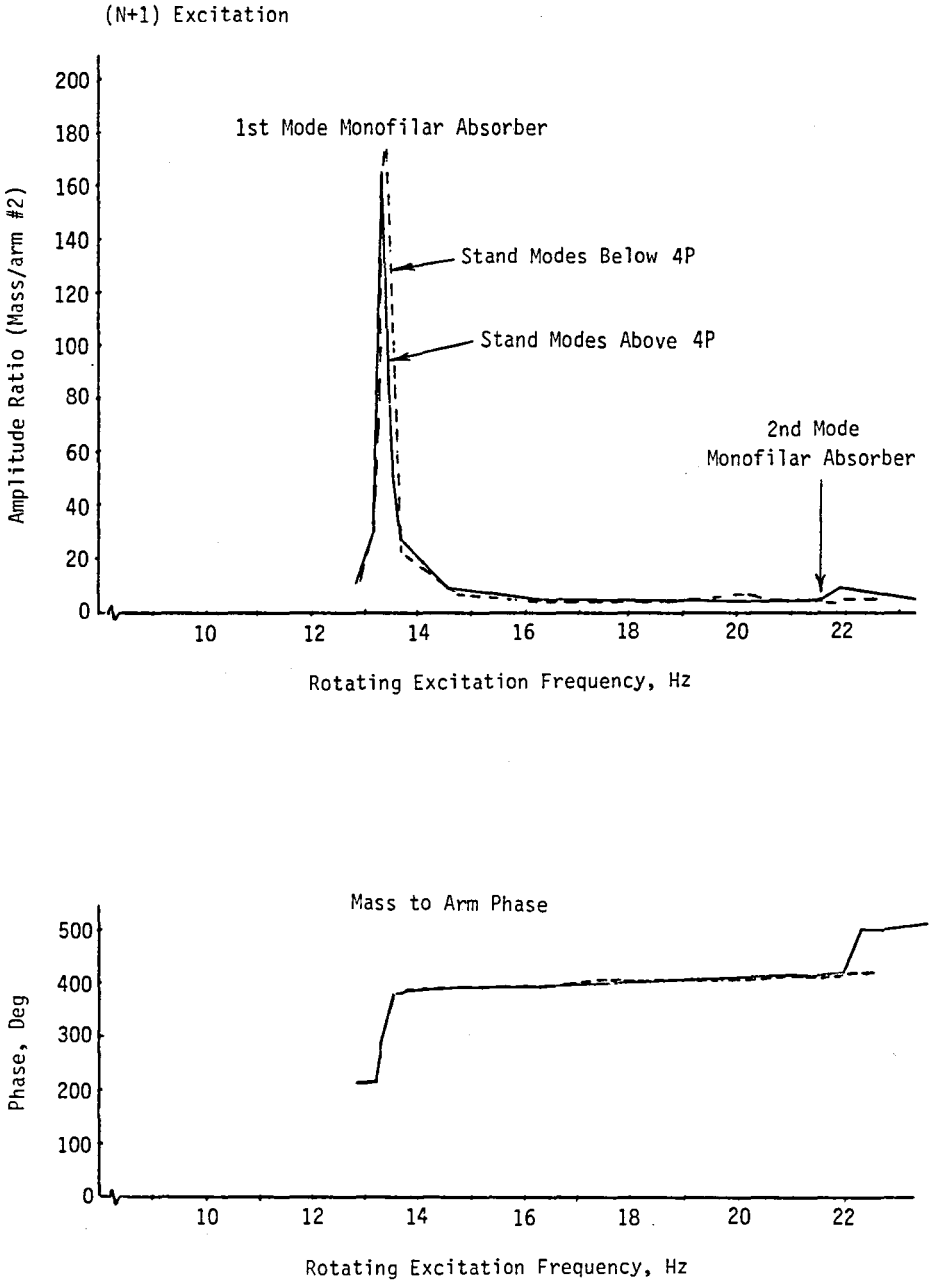

Figure 34. Modal Survey for (N+1)P Excitation, Stand Modes above 4P.

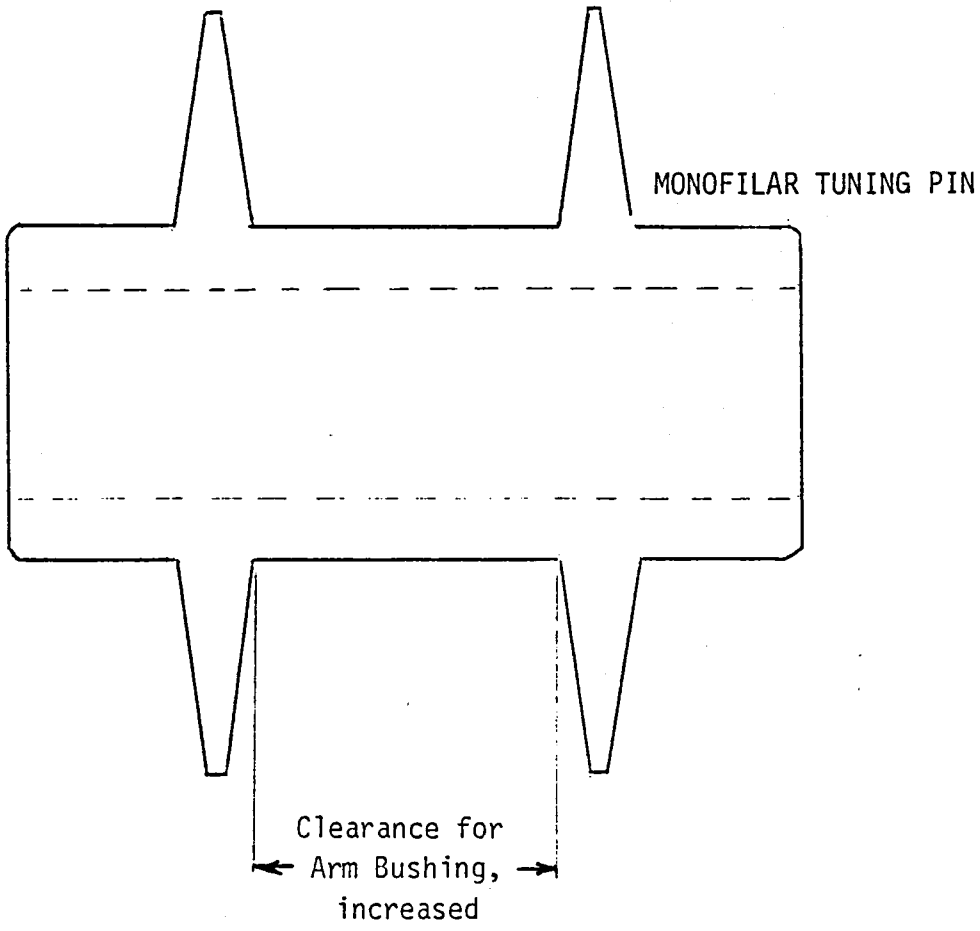

Figure 35. Monofilar Tuning Pin Modified to Increase Clearance.

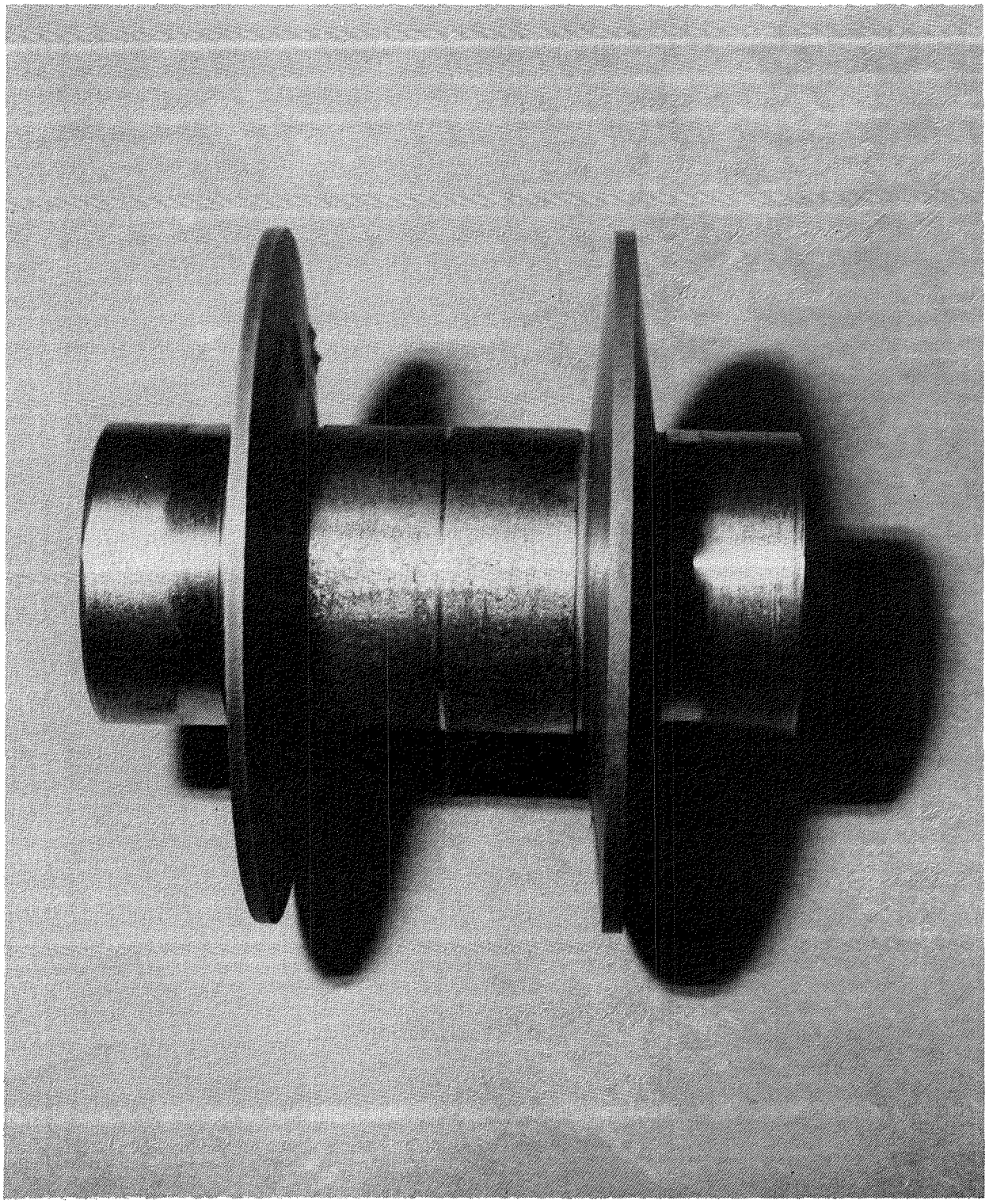

Figure 36. Monofilar Tuning Pin, Galled Surfaces.

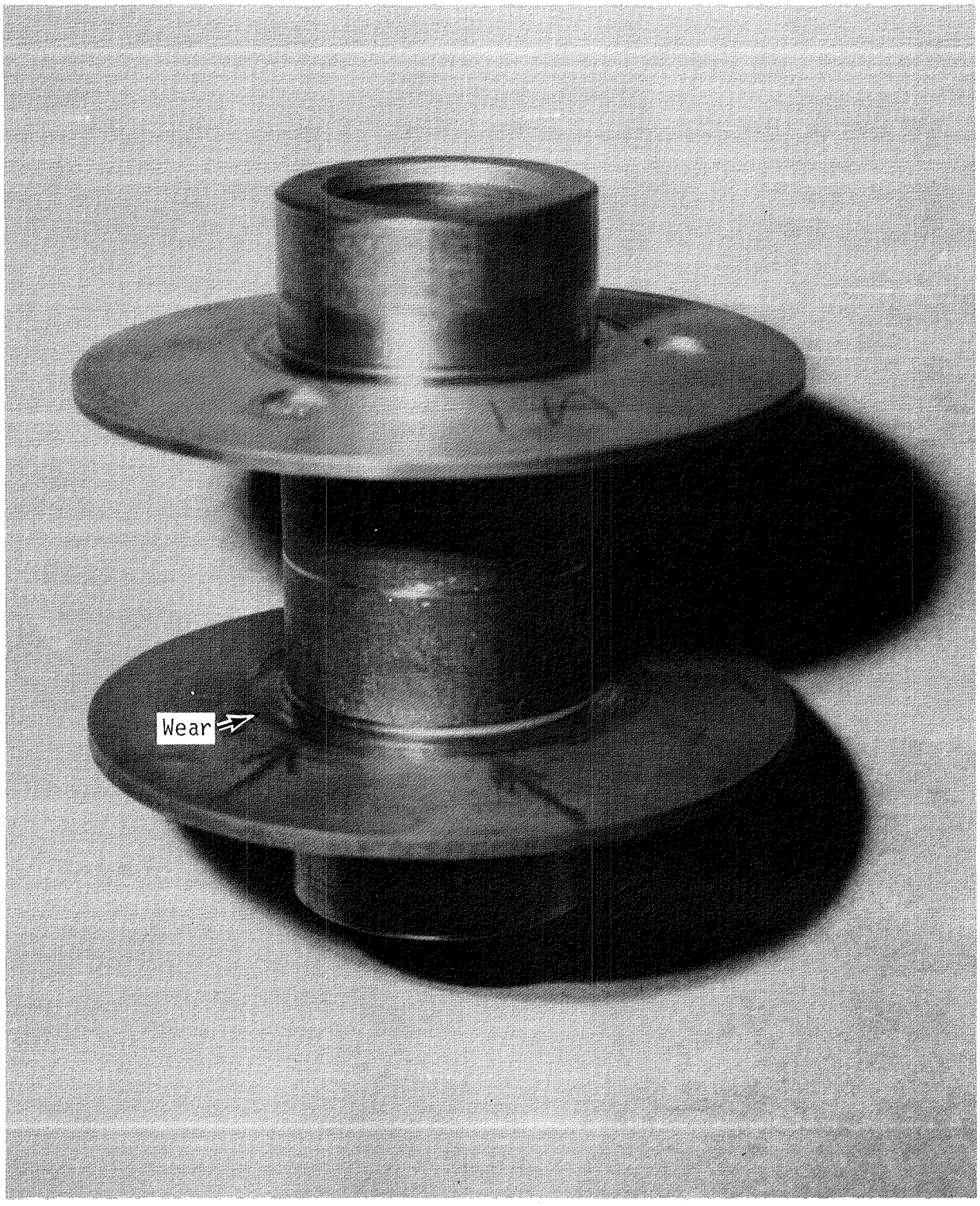

Figure 37. Monofilar Tuning Pin, Root Flange Wear.

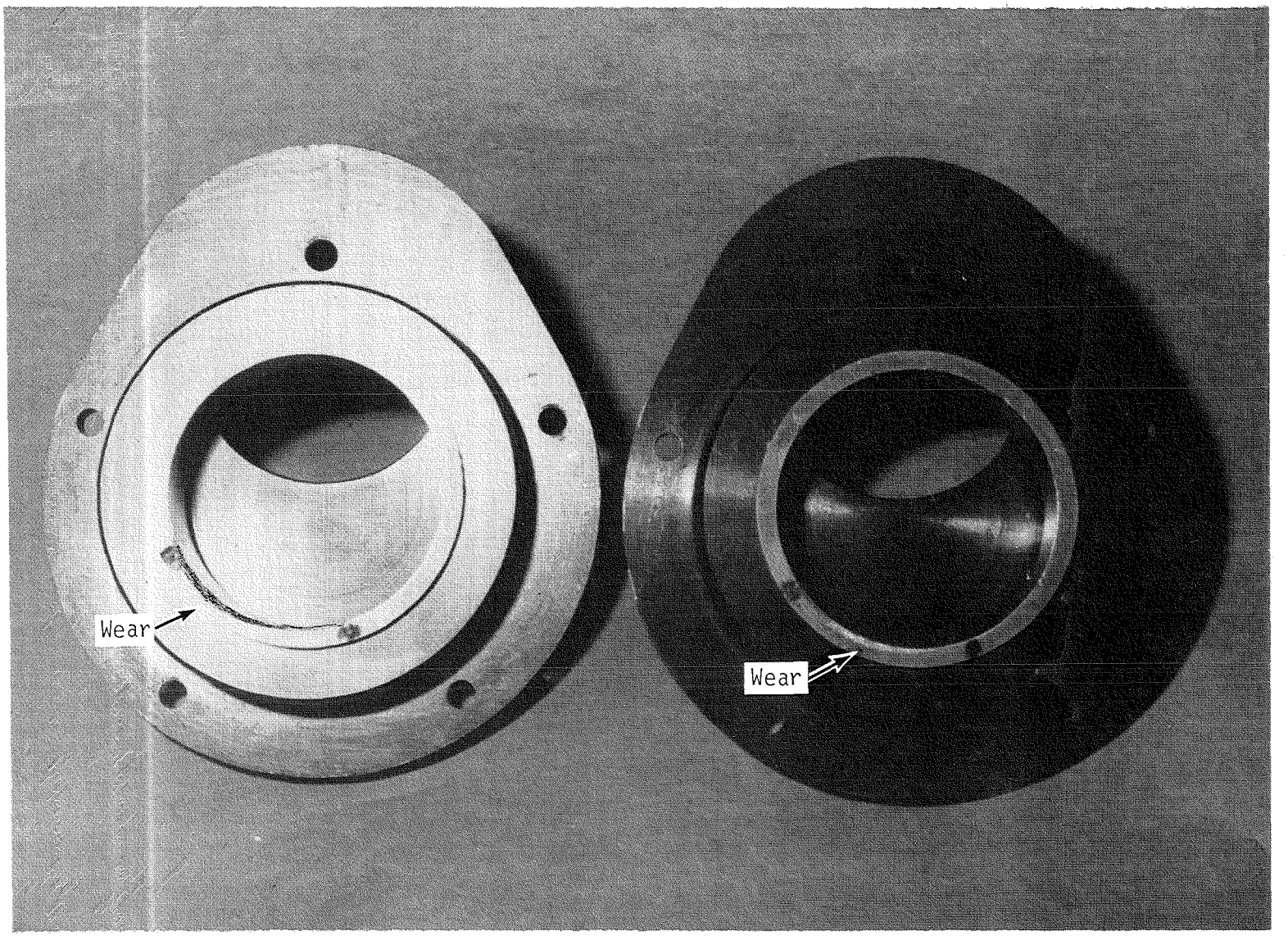

Figure 38. Monofilar Mass Bushing Wear, Top Outside Edges.

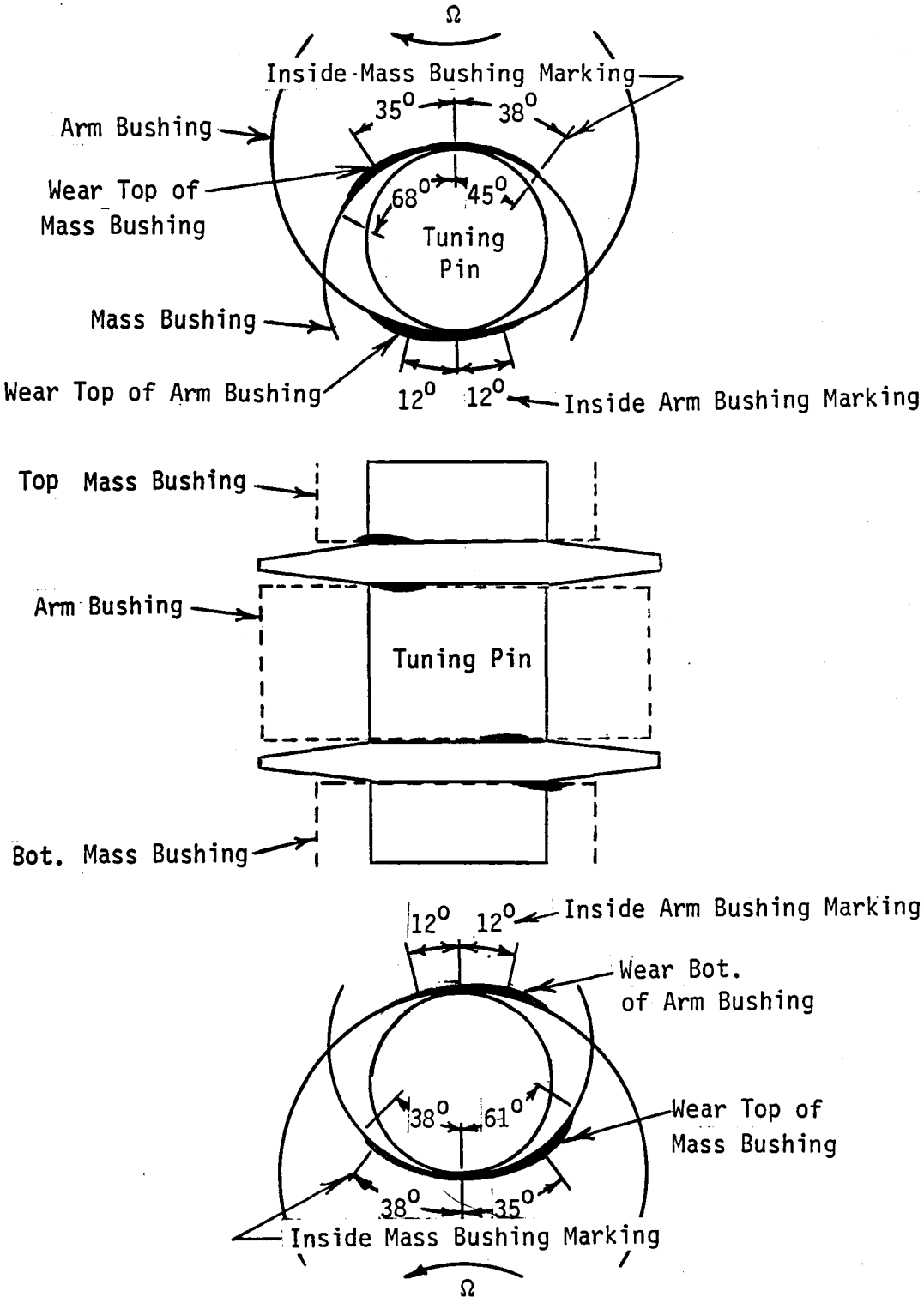

Figure 39. Monofilar Schematic of Overall Wear Pattern.

unbalance inertia forces on the top and the bottom mass. The second was due to the angular motion of the support arm when inplane motions are produced by the shaker forces at the hub. Another important consideration was that the centrifugal moment resulting from the perturbational torsional motion for the present monofilar configuration was in an unfavorable direction.

The importance of the centrifugal propeller moment effect (i.e. $[I_{horizontal} - I_{vertical}]\ \Omega^2\theta$) was demonstrated by testing the monofilar with the top and bottom mass steel weights removed. This reduced the weight of each absorber by a factor of 3 and reduced the torsional moment of inertia by a factor of 14. This configuration still had a negative propeller moment but it was much smaller than the configuration with the top and bottom masses. This configuration was tested using a forced response modal survey with test stand modes below and above 4P.

Figures 40 and 41 show that for the two test stand configurations both modes of the dynamic mass responded when excited with either (N-1)P or (N+1)P force excitations. It is clear from the phase plots of these figures that the second mode was excited each time; however, the mode occurred at two different frequencies. This variance of the frequency for the second mode is most likely being caused by the couplings with the stand dynamics and the magnitude of torsional motion. For this monofilar configuration, two vertical accelerometers were added to the leading and trailing edges of one dynamic mass to monitor the torsional motion. The results, based on the magnitude and phase of the pair of accelerometers, showed that the torsional motion was evident when the (N-1)P or the (N+1)P mode was strongly excited. These test results are considered evidence that the monofilar will function as a dual frequency absorber when the torsional dynamic mass motion is controlled.

In addition to the test program, a six degree-of-freedom eigenanalysis was developed to study the dynamics of the monofilar masses as coupled with the fixed-system test stand modes. The degrees-of-freedom were: hub longitudinal, hub lateral, γ_{1c}, γ_{1s}, γ_{2c}, and γ_{2s} (cyclic monofilar degrees of freedom in the fixed system).

The coupled mode shapes from these analytical results indicated that, with the test stand modes above or below 4P, the monofilar would respond if excited by a force at the natural frequency of either dynamic mass mode. This result supports that the monofilar should function as a dual frequency absorber.

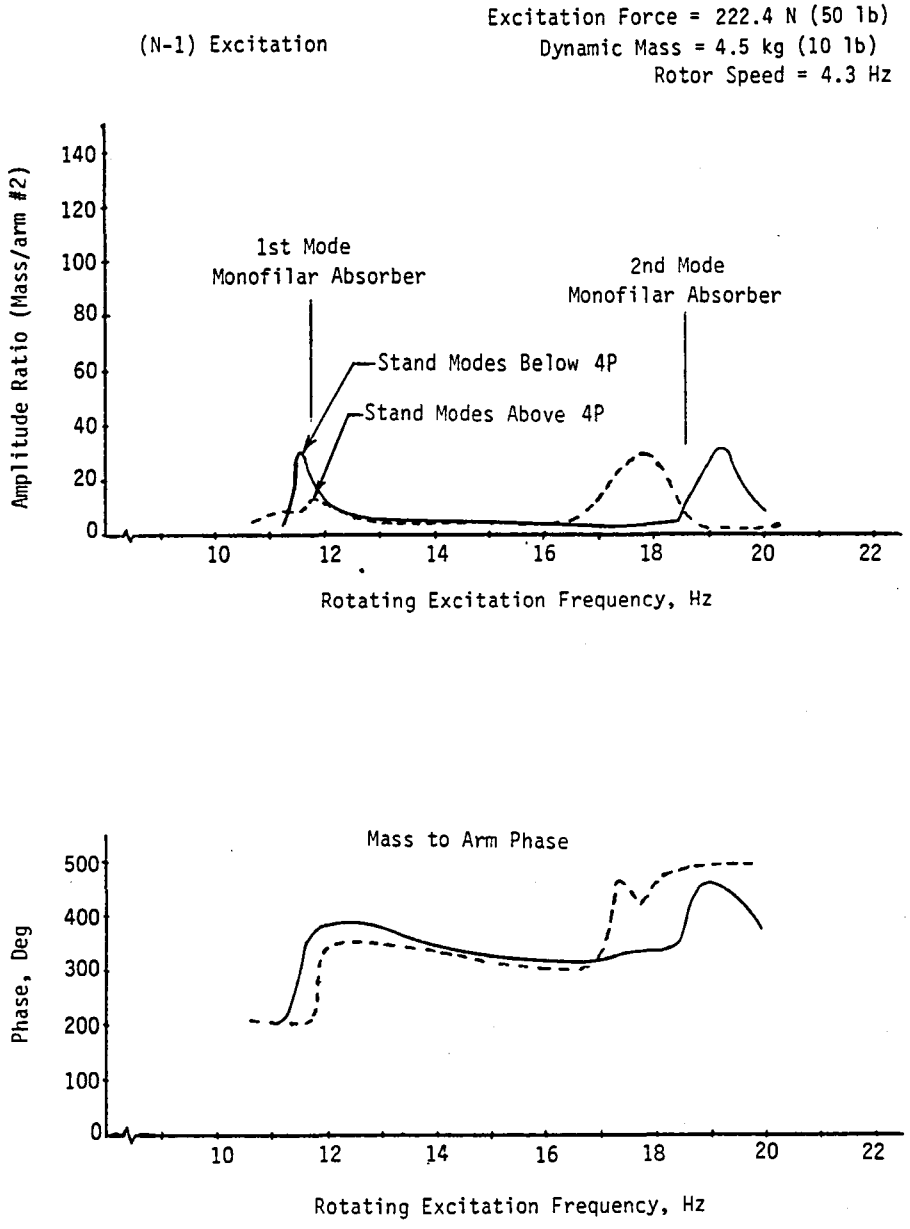

Figure 40. Modal Survey for (N-1)P Excitation, Steel Weights Removed from Dynamic Mass.

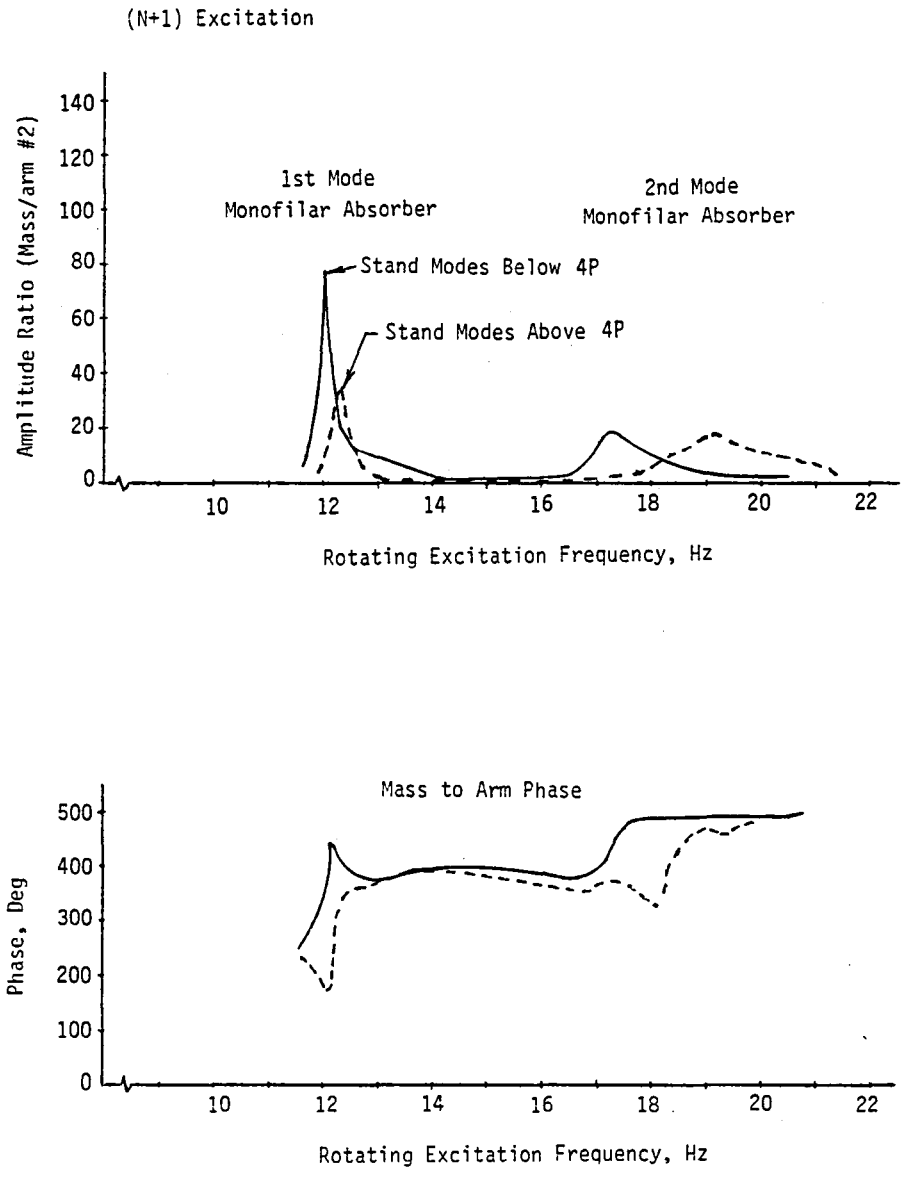

Figure 41. Modal Survey for (N+1)P Excitation, Steel Weights Removed from Dynamic Mass.

MONOFILAR DESIGN CRITERIA

Combining the analytical results from the section on Monofilar Design and the test results from the section on Ground Test, the monofilar design was studied to correlate analysis with test. In addition, the present monofilar rotor absorber design was re-examined to improve its performance with respect to attenuation of 4P hub response due to a (N+1)P excitation. This study focused on a new design that was required to eliminate the absorber mass torsional motion relative to its support arm.

Analytical Studies

The measured fixed-system hub response with the monofilar for a 3P rotating force excitation is shown versus the results from the linear ten degree-of-freedom coupled monofilar/airframe analysis (see Figure 42). The analysis was performed with the fixed-system dynamics defined for the baseline test stand configuration. The results showed that the analysis over predicted the stand hub motion using dynamic mass damping equal to 0.7 percent critical which was calculated from the modal survey test results. However, Figure 43 shows that the analytical prediction of rotor hub attenuation is in close agreement with the measured test data. The attenuation was calculated by comparing the hub response with and without absorber dynamic masses.

Figure 44 shows the absorber dynamic mass tangential acceleration from analysis and test versus 3P excitation force. As shown the predicted level of the dynamic mass motion is slightly higher than the measured data. For both the analysis and test results, the dynamic mass motions were basically a pure 3P rev which is the excitation frequency. Comparison of Figures 42 and 44 show that the correlation of hub response improves with less dynamic mass damping while the correlation of dynamic mass motion improves with an increase in damping. For these cases, the fixed system hub damping was varied from the measured .4 percent criticial but had little effect on the correlation. Because of the problems with the 5P response, as discussed earlier, no correlation results were obtained.

Improved Monofilar Design

As described in the section on Ground Test, the monofilar will function as a dual frequency absorber if the torsional motion of the dynamic mass relative to its support arm is controlled. Design solutions were studied. One approach is to reach a design that has a positive propeller moment (i.e. $[I_{horizontal} - I_{vertical}]\ \Omega^2\theta > 0$) and still has feasible geometric properties, tuning at 3P and 5P, and good attenuation characteristics.

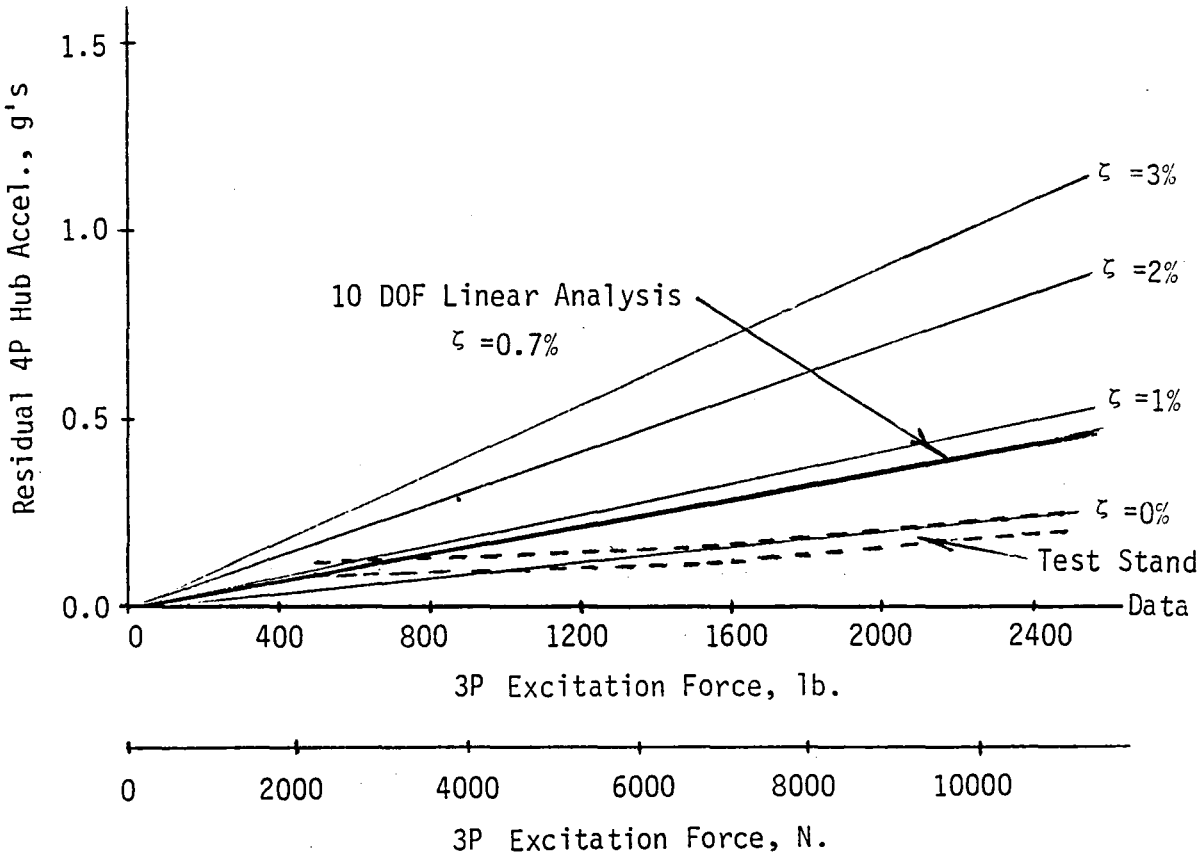

Figure 42. Monofilar Performance, Analysis versus Test.

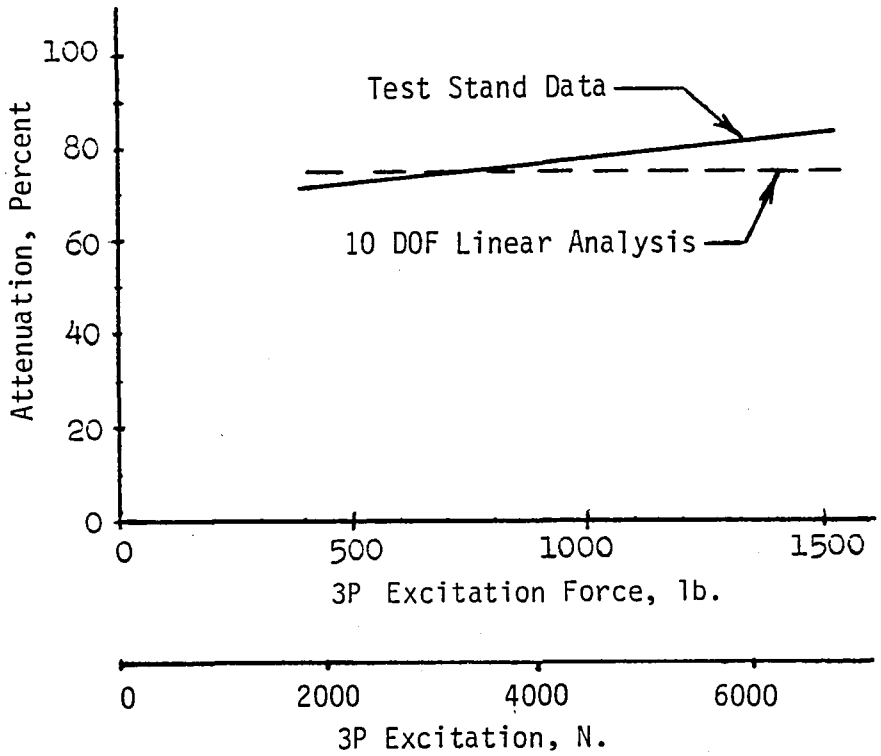

Figure 43. Monofilar 3P Attenuation, Analysis versus Test

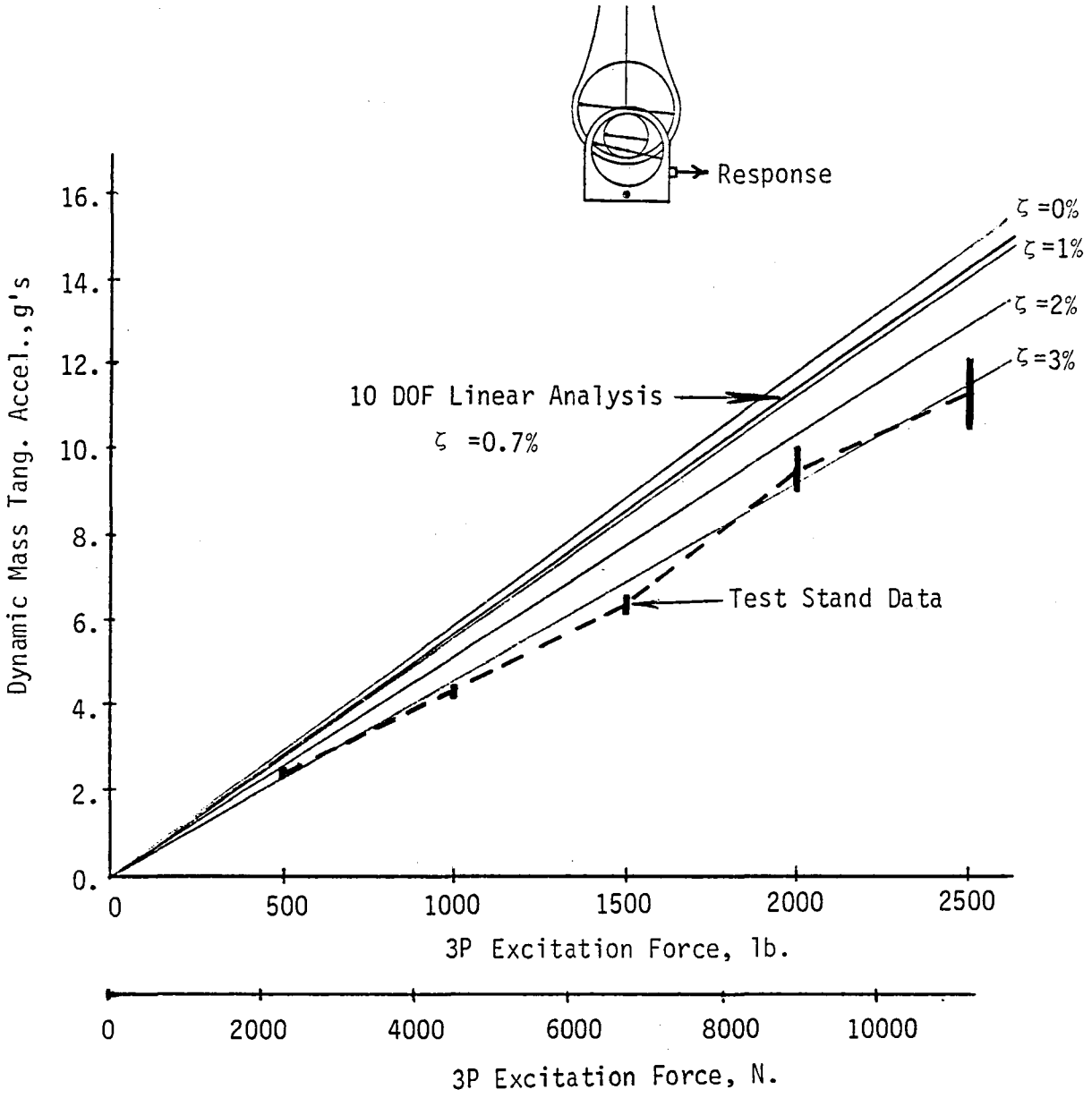

Figure 44. Dynamic Tangential Mass Motions, Analysis versus Test.

To obtain a monofilar design with the same weight 15.4 kg (34 lb) and have a positive propeller moment, it was necessary to allow the inertia of the dynamic mass (defined in Figure 5) to increase from .035 to the .062 to .068 kg-m^2 (.312 to the .55 to .60 in.-lb-sec^2) range. Figure 45 shows the design solution. Starting with the present monofilar properties, design solutions with higher mass moments of inertia were obtained using the linear tuning analysis until no solution at a higher inertia existed. Then the tuning pin diameter was incremented along with the appropriate pin properties until a final design solution was obtained.

A comparison of the performance of this revised monofilar design was obtained by using the linear analysis. The results in Figure 46 show that for a tuning design of exactly 3P and 5P, design solutions exist with performance similar to the present monofilar design. A design sketch of a monofilar dynamic mass with the required properties is shown in Figure 47. To minimize the increase in the mass moment of inertia of the new design, it was necessary to change the mass housing material from aluminum to tungsten. Other designs may be possible that have a positive propeller moment and while still retaining conventional materials.

An alternative approach would be to substitute two, vertically-displaced supports for the dynamic mass for the current single support. This would provide more capability for resisting upsetting torsional moments. However, the two-arm configuration would probably reduce the weight reduction potential of the monofilar.

Monofilar Risks

As described in the section on Design Studies, a basic design parameter pertinent to a successful monofilar design is the coefficient of friction. A fundamental assumption of the monofilar concept is that the motions of the tuning pin and the dynamic mass are pure rolling without slipping. If slipping occurs the natural frequencies of both modes will impact the effectiveness of the absorber.

During the ground test reported herein, the monofilar was excited by 3P rotating forces approximately twice as high as expected in flight. Correspondingly large excursion of the dynamic mass occurred. The performance of the monofilar at that excitation showed no loss in attenuation. In fact, the 3P attenuation improved slightly as the excitation amplitude increased. The coefficient of friction provided by steel on steel contact therefore seems to be sufficient. However, since the motion of the 5P mode was restricted by internal binding, the question of sufficient friction may still need to be resolved.

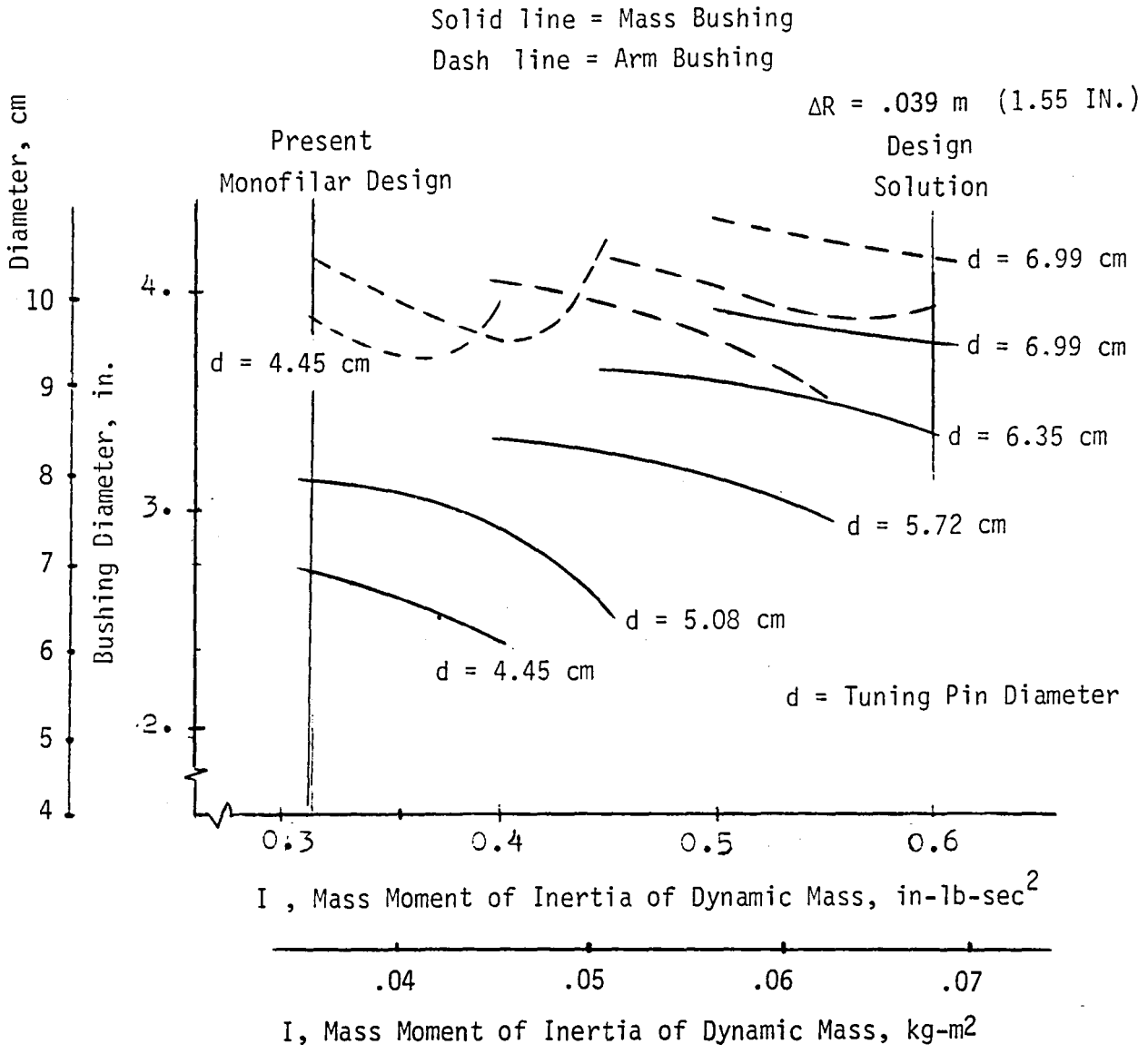

Figure 45. Tuning Curve for New Design.

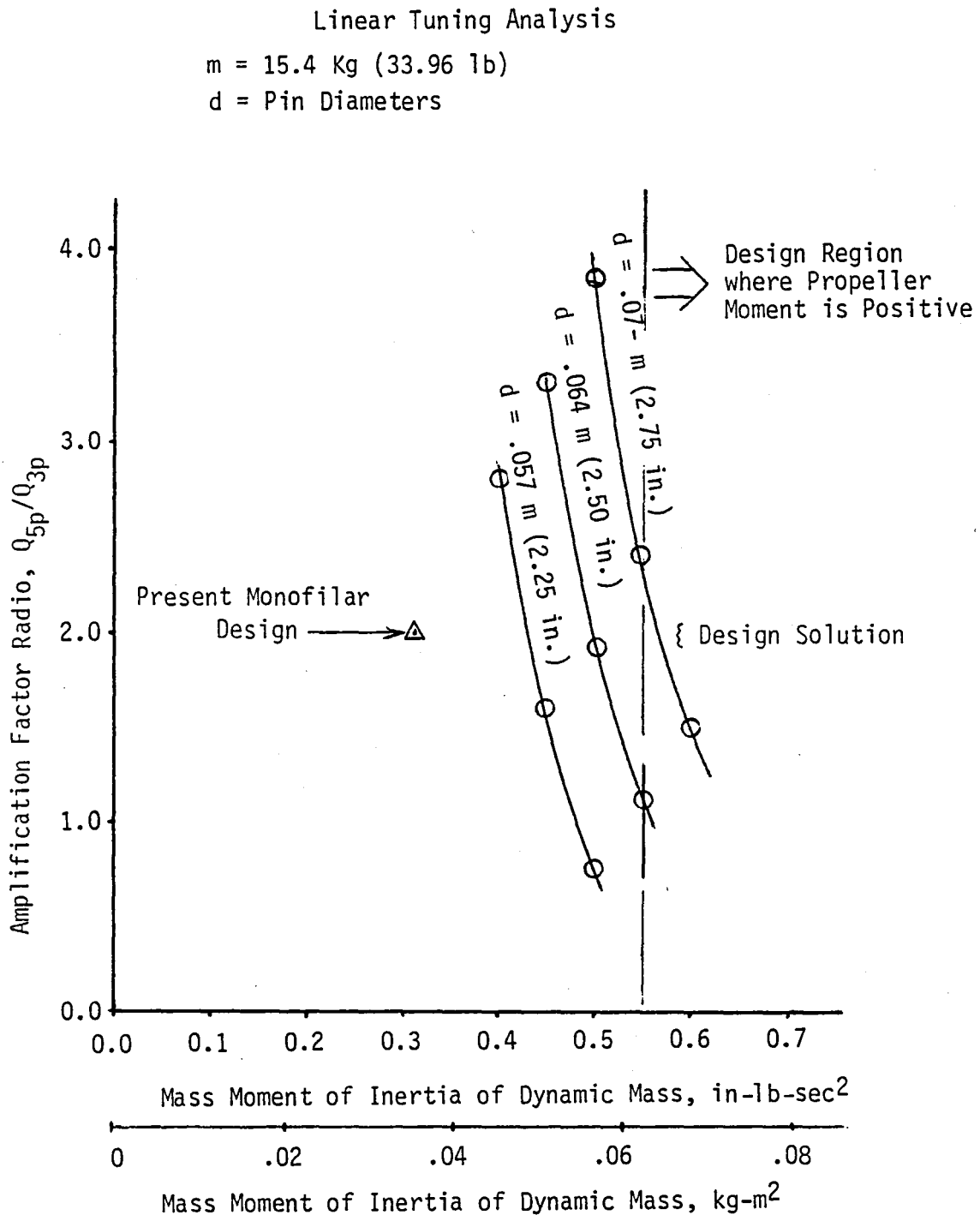

Figure 46. Predicted Monofilar Performance, New Design.

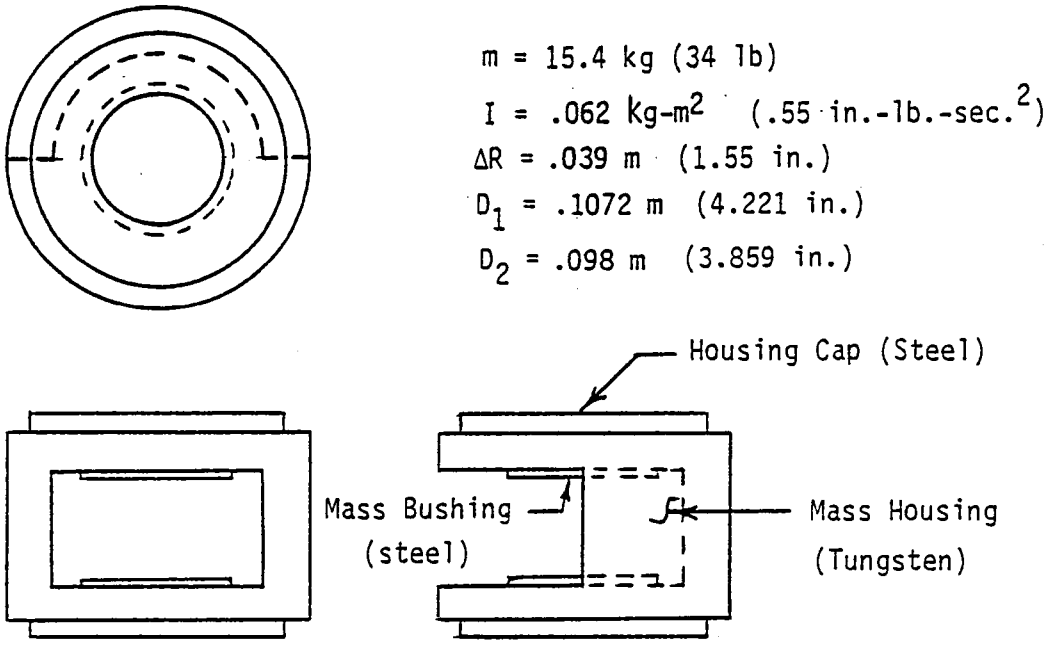

Figure 47. Monofilar Dynamic Mass, New Design.

If during future tests of the monofilar concepts, the friction coefficient becomes an issue, a tungsten carbide coating providing a higher coefficient of friction can be used. Such coatings are available which exhibit good wear and corrosion characteristics while providing a coefficient of friction that is approximately double that of steel on steel.

Another risk area is the control of the torsional motion of the dynamic masses. As discussed in the previous sections, this motion causes binding of the tuning pin resulting in suppression of the 5P mode of the monofilar. Although a conceptual redesign has been explored and shows promise in controlling this motion, a more detailed design analysis and confirmation test should be conducted to insure adequate 5P modal response.

CONCLUSIONS

Based on the results of this Monofilar Design and Bench Test Program the following conclusions are presented.

Monofilar Analyses

1. The two degree-of-freedom linear analysis provides an accurate prediction of the frequencies and mode shapes of the monofilar. Bench impact testing showed good correlation of the test frequencies and mode shapes with those calculated with the centrifugal force replaced by the gravitational force. Rotating test results also showed good correlation of frequencies. In both tests, frequencies were predicted within 4.6 and 0.1 percent of measure values for the first and second modes, respectively.

2. The ten degree-of-freedom coupled monofilar/airframe linear analysis provides a good prediction of absorber attenuation for (N-1)P excitation, but overpredicts the dynamic mass motion by 25 to 30 percent when compared to the test results.

Monofilar Performance

3. Rotating test results show that the monofilar absorber provides significant attenuation (60 to 80 percent) of (N-1)P inplane forces in the rotating system.

4. The current monofilar design provides small attenuation (40%) of (N+1)P inplane forces in the rotating system. This attenuation was primarily due to the added-mass effects rather than favorable dynamic response of the masses.

5. The relatively low (N+1)P attenuation is caused by excessive torsional motion of the absorber dynamic mass that results in binding of the tuning pin on its flanges. The wear pattern observed, together with measured torsional acceleration and the greater sensitivity of the (N+1)P mode response to binding, supports this conclusion.

6. The excessive torsional motion is believed to be caused by unsymmetrical excitation of the dynamic mass due to hub rotations combined with an unfavorable centrifugal "propeller" moment acting on the dynamic mass.

Conceptual Redesign

7. A conceptual redesign minimizing the torsional motion of the dynamic masses has been defined. It is feasible to modify the present monofilar to provide attenuation at both (N-1)P and (N+1)P frequencies.

8. The monofilar concept should be studied further. The modified design should be evaluated on the rotating absorber test facility to establish final design criteria for a flightworthy article.

Comparison with Bifilar

9. The monofilar can provide good attenuation at (N-1)P force level that is approximately twice as high as the level at which the attenuation provided by a conventional bifilar would begin to deteriorate. This implies that the monofilar could potentially be used to attenuate a single frequency force with less dynamic mass than is used on a bifilar.

10. The monofilar attenuates (N-1)P rotating inplane forces with less variance of motion among the four dynamic masses than exists on a typical bifilar. This reduces the potential for non-NP vibration that would be caused by dissimilar dynamic mass responses.

Test Facility

11. A rotating absorber test facility with fixed system representation of hub inplane modes and excitation force input provides a simple and cost effective method of testing and evaluating new absorber concepts. The facility not only provides direct measurement of quantities not usually available from flight test (such as absorber attenuation) but also allows investigation of much wider ranges of important design and operational parameters.

APPENDIX

DERIVATION OF MONOFILAR EQUATIONS OF MOTION

To apply Lagrange's equation for obtaining the required monofilar equations of motion, a position vector for the center of gravity of the dynamic mass must be defined. This position vector in the X-Y coordinate system (see Figure 48) is obtained in the following manner:

(i) Establish the location of the pin center following the γ_1 rotation:

$$X_p = R_o + \frac{D_1-d}{2} \cos \gamma_1$$

$$Y_p = \frac{D_1-d}{2} \sin \gamma_1 \qquad (1)$$

(ii) Establish the location of the center of the mass bushing following the superposition of the γ_2 rotation:

$$X_m = X_p + \frac{D_2-d}{2} \cos (\gamma_1+\gamma_2)$$

$$Y_m = Y_p + \frac{D_2-d}{2} \sin (\gamma_1+\gamma_2) \qquad (2)$$

(iii) Establish the location of the center of gravity of the dynamic mass relative to the center of the mass bushing:

$$X_{CG} = X_m + \Delta R \cos\beta$$

$$Y_{CG} = Y_m + \Delta R \sin\beta \qquad (3)$$

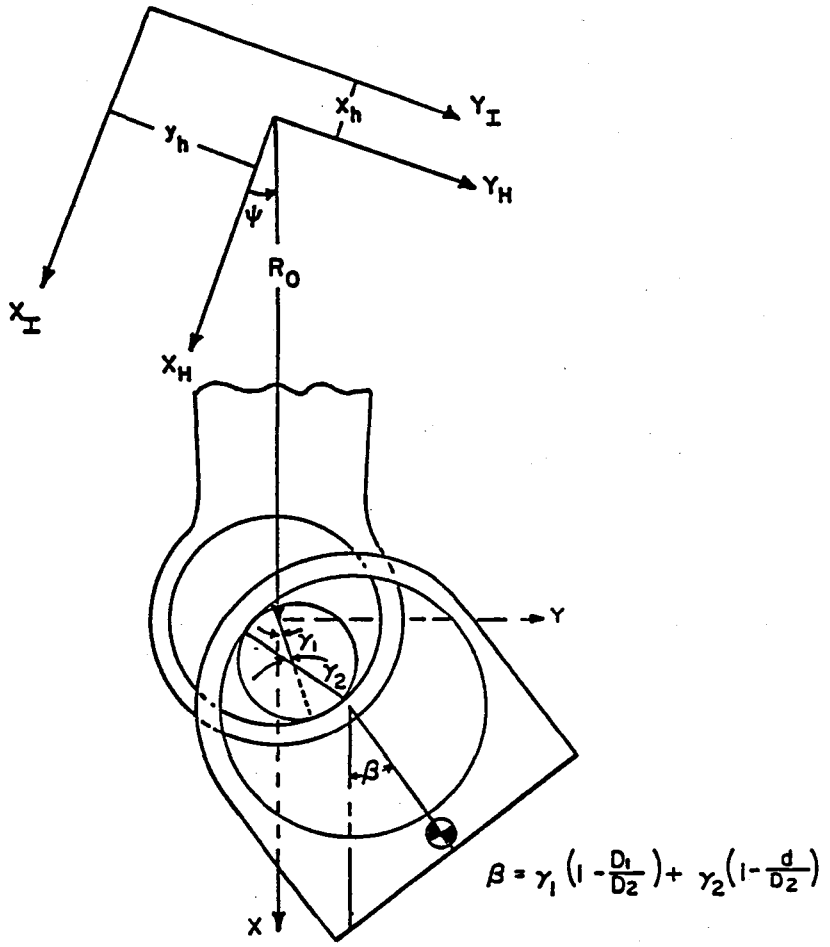

Figure 48. Monofilar Math Model.

where:

$$\beta = \gamma_1 \quad (1-\frac{D_1}{D_2}) \quad + \gamma_2 \quad (1-\frac{d}{D_2}) \tag{4}$$

Substituting equations (1), (2) and (4) into equation (3), equation (3) can be written in the following form:

$$X_{CG} = R_0 + \frac{D_1-d}{2} \cos \gamma_1 + \frac{D_2-d}{2} \cos (\gamma_1+\gamma_2)$$

$$+ \Delta R \cos [\gamma_1 \quad (1-\frac{D_1}{D_2}) \quad + \gamma_2 \quad (1-\frac{d}{D_2})]$$

$$Y = \frac{D_1-d}{2} \sin \gamma_1 + \frac{D_2-d}{2} \sin (\gamma_1+\gamma_2) \tag{5}$$

$$+\Delta R \sin [\gamma_1 \quad (1-\frac{D_1}{D}) \quad + \gamma_2 \quad (1-\frac{d}{D_2})]$$

The position of the CG of the dynamic mass can be written in reference to the inertia frame as follows:

$$X_I = X_h + R_o \cos\psi + \frac{D_1-d}{2} \cos (\gamma_1+\psi)$$

$$+ \frac{D_2-d}{2} \cos (\psi+\gamma_1+\gamma_2)$$

$$+\Delta R\cos [\psi+\gamma_1 \quad (1-\frac{D_1}{D_2}) \quad + \gamma_2 \quad (1-\frac{d}{D_2})]$$

$$Y_I = Y_h + R_o \sin\psi + \frac{D_1-d}{2} \sin (\psi+\gamma_1) \tag{6}$$

$$+ \frac{D_2-d}{2} \sin (\psi+\gamma_1+\gamma_2)$$

$$+ \Delta R \sin [\psi+\gamma_1 (1-\frac{D_1}{D_2}) + \gamma_2 (1-\frac{d}{D_2})]$$

Having defined the position vector of the CG of the dynamic mass, the kinetic energy (T) of the system becomes:

$$T = \frac{1}{2} m \{\dot{X}_I^2 + \dot{Y}_I^2\} + I [\Omega + \dot{\gamma}_1 (1-\frac{D_1}{D_2}) + \dot{\gamma}_2 (1-\frac{d}{D_2})]^2 \quad (7)$$

where X_I and Y_I can be found by differentiating equations (6).

The non-linear equations of motion for the monofilar are obtained by substitution of equation (7) into Lagrange's equation. The dissipative force due to monofilar motions were modeled as equivalent viscous damping.

$$\frac{d}{dt} \frac{\partial T}{\partial \dot{q}_i} - \frac{\partial T}{\partial q_i} = 0 \quad (8)$$

where $q_i = \gamma_1$ or γ_2

giving the following γ_1 and γ_2 equations, (9) and (10):

$$-\ddot{X}_h \left\{\frac{r_1}{2}\sin(\gamma_1+\psi) + \frac{r_2}{2}\sin(\gamma_1+\gamma_2+\psi) + \Delta R\ \left(1-\frac{D_1}{D_2}\right)\ \sin\ \left[\frac{r_2}{D_2}\gamma_2 + \left(1-\frac{D_1}{D_2}\right)\gamma_1+\psi\right]\right\}$$

$$+\ddot{Y}_h \left\{\frac{r_1}{2}\cos(\gamma_1+\psi) + \frac{r_2}{2}\cos(\gamma_1+\gamma_2+\psi) + \Delta R\ \left(1-\frac{D_1}{D_2}\right)\ \cos\ \left[\frac{r_2}{D_2}\gamma_2 + \left(1-\frac{D_1}{D_2}\right)\gamma_1+\psi\right]\right\}$$

$$+\ddot{\gamma}_1 \left\{\left(\frac{r_1}{2}\right)^2 + \left(\frac{r_2}{2}\right)^2 + (\Delta R)^2\ \left(1-\frac{D_1}{D_2}\right)^2 + \frac{r_1 r_2}{2}\cos\gamma_2 + r_1\Delta R\ \left(1-\frac{D_1}{D_2}\right)\cos\left[\frac{r_2}{D_2}\gamma_2-\frac{D_1}{D_2}\gamma_1\right]\right.$$

$$\left.+r_2\Delta R\ \left(1-\frac{D_1}{D_2}\right)\ \cos\left[\frac{d}{D_2}\ \gamma_2 + \frac{D_1}{D_2}\gamma_1\right] + \frac{I}{m}\ \left(1-\frac{D_1}{D_2}\right)^2\right\}$$

$$+\ddot{\gamma}_2 \left\{\left(\frac{r_2}{2}\right)^2 + (\Delta R)^2\ \frac{r_2}{D_2}\ \left(1-\frac{D_1}{D_2}\right) + \frac{r_1 r_2}{4}\cos\gamma_2 + \frac{r_1 r_2}{2}\frac{\Delta R}{D_2}\cos\left[\frac{r_2}{D_2}\gamma_2 - \frac{D_1}{D_2}\gamma_1\right]\right.$$

$$\left.+\frac{r_2}{2}\ \frac{2r_2-r_1}{D_2}\Delta R\cos\left[\frac{d}{D_2}\ \gamma_2 + \frac{D_1}{D_2}\gamma_1\right] + \frac{I}{m}\ \frac{r_2}{D_2}\ \left(1-\frac{D_1}{D_2}\right)\right\} + \gamma_1 2\zeta_{\gamma_1}\omega_{\gamma_1}$$

$$+\dot{\gamma}_2\left\{-\frac{r_1 r_2}{2}\Omega\sin\gamma_2 - r_1 r_2\frac{\Delta R}{D_2}\Omega\sin\left[\frac{r_2}{D_2}\ \gamma_2 - \frac{D_1}{D_2}\gamma_1\right]\right.$$

$$\left.+\frac{r_2}{2}\frac{\Delta R}{D_2}\Omega\ (2r_1)\sin\left[\frac{d}{D_2}\gamma_2 + \frac{D_1}{D_2}\gamma_1\right]\right\}$$

$$+\dot{\gamma}_1^2\left\{\frac{r_1}{2}\Delta R\ \frac{D_1}{D_2}\ \left(1-\frac{D_1}{D_2}\right)\ \sin\ \left[\frac{r_2}{D_2}\gamma_2 - \frac{D_1}{D_2}\gamma_1\right]\right.$$

$$\left.-\frac{r_2}{2}\Delta R\ \frac{D_1}{D_2}\ \left(1-\frac{D_1}{D_2}\right)\sin\left[\frac{d}{D_2}\ \gamma_2 + \frac{D_1}{D_2}\gamma_1\right]\right\}$$

$$+\dot{\gamma}_2^2 \left\{-\frac{r_1 r_2}{4} \sin \gamma_2 - \frac{r_1}{2} \Delta R \left(\frac{r_2}{D_2}\right)^2 \sin \left[\frac{r_2}{D_2} \gamma_2 - \frac{D_1}{D_2}\gamma_1\right]\right.$$

$$\left. + \frac{r_2}{2} \Delta R \left[\frac{D_1}{D_2} - 2\frac{d}{D_2} + \frac{d^2}{D_2^2}\right] \sin \left[\frac{d}{D_2} \gamma_2 + \frac{D_1}{D_2} \gamma_1\right]\right\}$$

$$+\dot{\gamma}_1\dot{\gamma}_2 \left\{ - \frac{r_1 r_2}{2} \sin \gamma_2 - r_2 \frac{\Delta R}{D_2} d \left(1-\frac{D_1}{D_2}\right) \sin \left[\frac{d}{D_2} \gamma_2 + \frac{D_1}{D_2}\gamma_1\right]\right.$$

$$\left. - r_1 \Delta R \frac{r_2}{D_2} \left(1-\frac{D_1}{D_2}\right) \sin \left[\frac{r_2}{D_2}\gamma_2 - \frac{D_1}{D_2}\gamma_1\right]\right\}$$

$$+\Omega^2 \left\{\frac{r_1}{2} R_o \sin\gamma_1 + \frac{r_2}{2} R_o \sin (\gamma_1 + \gamma_2) - \frac{r_1}{2} \Delta R \frac{D_1}{D_2} \sin \left(\frac{r_2}{D_2} \gamma_2 - \frac{D_1}{D_2}\gamma_1\right)\right.$$

$$\left. + R_o \Delta R \left(1-\frac{D_1}{D_2}\right) \sin \left[\frac{r_2}{D_2} \gamma_2 + \left(1-\frac{D_1}{D_2}\right) \gamma_1\right] + \frac{r_2}{2} \Delta R \frac{D_1}{D_2} \sin \left[\frac{d}{D_2}\gamma_2 + \frac{D_1}{D_2}\gamma_1\right]\right\} \equiv 0$$

(9)

$$-\ddot{x}_h \left\{\frac{r_2}{2} \sin (\gamma_1+\gamma_2+\psi) + r_2 \frac{\Delta R}{D_2} \sin \left[\frac{\Delta R}{D_2} \gamma_2 + \left(1-\frac{D_1}{D_2}\right) \gamma_1+\psi\right]\right\}$$

$$+\ddot{y}_h \left\{-\frac{r_2}{2} \cos(\gamma_1+\gamma_2+\psi) + r_2 \frac{\Delta R}{D_2} \cos \left[\frac{r_2}{D_2} \gamma_2 + \left(1-\frac{D_1}{D_2}\right) \gamma_1+\psi\right]\right\}$$

$$+\ddot{\gamma}_1 \left\{\left(\frac{r_2}{2}\right)^2 + (\Delta R)^2 \frac{r_2}{D_2} \left(1-\frac{D_1}{D_2}\right) + \frac{r_1 r_2}{4} \cos \gamma_2 + \frac{I}{m} \frac{r_2}{D_2} \left(1- \frac{D_1}{D_2}\right)\right.$$

$$\left. + \frac{r_1 r_2}{2} \frac{\Delta R}{D_2} \cos \left[\frac{r_2}{D_2} \gamma_2 - \frac{D_1}{D_2} \gamma_1\right] + \frac{r_2}{2} \Delta R \left[2 - \frac{D_1+d}{D_2}\right] \cos \left[\frac{d}{D_2}\gamma_2 + \frac{D_1}{D_2}\gamma_1\right]\right\}$$

$$+\dot{\gamma} \quad \{(\frac{r_2}{2})^2 + (\frac{r_2\Delta R}{D_2})^2 + r_2^2 \frac{\Delta R}{D_2} \cos [\frac{d}{D_2} \gamma_2 + \frac{D_1}{D_2}\gamma_1] + \frac{I}{m} (\frac{r_2}{D_2})^2 \}$$

$$+\dot{\gamma}_1 \quad \{-r_1 r_2 \Omega \frac{\Delta R}{D_2} \sin [\frac{d}{D_2} \gamma_2 + \frac{D_1}{D_2}\gamma_1] + \frac{r_1 r_2}{2} \Omega \sin \gamma_2$$

$$+ r_1 r_2 \frac{\Delta R}{D_2} \Omega \sin [\frac{r_2}{D_2} \gamma_2 - \frac{D_1}{D_2}\gamma_1]\}$$

$$+ \dot{\gamma}_2 (2\zeta_{\gamma_2} \omega_{\gamma_2}) + \dot{\gamma}_1\dot{\gamma}_2 \{-r_2 \frac{\Delta R}{D_2} D_1 (1- \frac{d}{D_2}) \sin [\frac{d}{D_2} \gamma_2 + \frac{D_1}{D_2} \gamma_1]\}$$

$$+ \dot{\gamma}_1^2 \{- \frac{r_1 r_2}{2} \frac{\Delta R}{D_2} (1-\frac{D_1}{D_2}) \sin [\frac{d}{D_2} \gamma_2 + \frac{D_1}{D_2} \gamma_1] + \frac{r_1 r_2}{4} \sin \gamma_2$$

$$+ \frac{r_1 r_2}{2} \frac{\Delta R}{D_2} \sin [\frac{r_2}{D_2} \gamma_2 - \frac{D_1}{D_2} \gamma_1] - \frac{r_2^2}{2} \frac{\Delta R}{D_2} \frac{D_1}{D_2} \sin [\frac{d}{D_2} \gamma_2 + \frac{D_1}{D_2} \gamma_1]\}$$

$$+ \dot{\gamma}_2^2 \{- \frac{1}{2} (\frac{r_2}{D_2})^2 d\Delta R \sin [\frac{d}{D_2} \gamma_2 + \frac{D_1}{D_2} \gamma_1]\}$$

$$+ \Omega^2 \{\frac{r_1 r_2}{4} \sin \gamma_2 + \frac{r_2}{2} R_o \sin(\gamma_1 + \gamma_2) + r_2 R_o \frac{\Delta R}{D_2} \sin [\frac{r_2}{D_2} \gamma_2 + (1-\frac{D_1}{D_2}) \gamma_1]$$

$$+ \frac{r_1 r_2}{2} \frac{\Delta R}{D_2} \sin [\frac{r_2}{D_2} \gamma_2 - \frac{D_1}{D_2} \gamma_1] + \frac{r_2}{2} \frac{\Delta R d}{D_2} \sin [\frac{d}{D_2} \gamma_2 + \frac{D_1}{D_2} \gamma_1] \equiv 0 \qquad (10)$$

To complete the math model, we should also include into the Eqs (9) and (10) the contributions of the pin mass and inertia. The pin is the second moving mass which has only γ_1 motion, and contributes to the total kinetic energy of the system. To evaluate

the kinetic energy due to the pin motion, we must define the position vector of the center of the pin with respect to the inertia frame. The position vector based on equation (1) including hub translation and rotation can be written as follows:

$$X_p^I = X_h + R_o \cos\psi + \frac{r_1}{2}\cos(\psi + \gamma_1)$$

$$Y_p^I = Y_h + R_o \sin\psi + \frac{r_1}{2}\sin(\psi + \gamma_1) \qquad (11)$$

We can now evaluate the kinetic energy (Tp) of the pin motion.

$$T_p = \frac{1}{2} m_p [(\dot{X}_p^I)^2 + (\dot{Y}_p^I)^2] + \frac{1}{2} I_p \dot{\theta}_p^2 \qquad (12)$$

where

$$\dot{\theta}_p = \frac{r_1}{d}\dot{\gamma}_1$$

Consequently, we can derive the additional terms equation (13) to the γ_1 equation (9) due to the pin motion by substituting equation (12) into the Lagrange's equation (8).

$$-\ddot{X}_h\{\frac{1}{2} m_p r_1 \sin(\psi + \gamma_1)\}$$

$$+\ddot{Y}_h\{\frac{1}{2} m_p r_1 \cos(\psi + \gamma_1)\}$$

$$+\ddot{\gamma}_1\{m_p (\frac{r_1}{2})^2 + I_p (\frac{r_1}{d})^2\}$$

$$\Omega^2 m_p R_o \frac{r_1}{2}\sin\gamma_1 = 0.0 \qquad (13)$$

These equations were developed further to provide a coupled absorber/airframe analysis for kth mass and hub lateral and longitudinal DOF's. These equations are presented in Figure 49.

γ_{1k} – EQUATION

$$
\begin{aligned}
&-m_k\ddot{x}\left\{\frac{r_{1k}}{2}\sin(\gamma_{1k}+\psi_k)+\frac{r_{2k}}{2}\sin(\gamma_{1k}+\gamma_{2k}+\psi_k)+\Delta R_k\left(1-\frac{D_{1k}}{D_{2k}}\right)\sin\left[\frac{r_{2k}}{D_{2k}}\gamma_{2k}+\left(1-\frac{D_{1k}}{D_{2k}}\right)\gamma_{1k}+\psi_k\right]\right\}\\
&+m_k\ddot{y}\left\{\frac{r_{1k}}{2}\cos(\gamma_{1k}+\psi_k)+\frac{r_{2k}}{2}\cos(\gamma_{1k}+\gamma_{2k}+\psi_k)+\Delta R_k\left(1-\frac{D_{1k}}{D_{2k}}\right)\cos\left[\frac{r_{2k}}{D_{2k}}\gamma_{2k}+\left(1-\frac{D_{1k}}{D_{2k}}\right)\gamma_{1k}+\psi_k\right]\right\}\\
&+m_k\ddot{\gamma}_{1k}\left\{\frac{r_{1k}^2+r_{2k}^2}{4}+\Delta R_k^2\left(1-\frac{D_{1k}}{D_{2k}}\right)^2+\frac{r_{1k}r_{2k}}{2}\cos\gamma_{2k}+r_{1k}\Delta R_k\left(1-\frac{D_{1k}}{D_{2k}}\right)\cos\left[\frac{r_{2k}}{D_{2k}}\gamma_{2k}-\frac{D_{1k}}{D_{2k}}\gamma_{1k}\right]\right.\\
&\quad\left.+r_{2k}\Delta R_k\left(1-\frac{D_{1k}}{D_{2k}}\right)\cos\left[\frac{d_k}{D_{2k}}\gamma_{2k}+\frac{D_{1k}}{D_{2k}}\gamma_{1k}\right]+\frac{I_k}{m_k}\left(1-\frac{D_{1k}}{D_{2k}}\right)^2\right\}\\
&+m_k\ddot{\gamma}_{2k}\left\{\left(\frac{r_{2k}}{2}\right)^2+\Delta R_k^2\frac{r_{2k}}{D_{2k}}\left(1-\frac{D_{1k}}{D_{2k}}\right)+\frac{r_{1k}r_{2k}}{4}\cos\gamma_{2k}+\frac{r_{1k}r_{2k}}{2}\frac{\Delta R_k}{D_{2k}}\cos\left[\frac{r_{2k}}{D_{2k}}\gamma_{2k}-\frac{D_{1k}}{D_{2k}}\gamma_{1k}\right]\right.\\
&\quad\left.+\frac{r_{2k}}{2}\left(\frac{2r_{2k}-r_{1k}}{D_{2k}}\right)\Delta R_k\cos\left[\frac{d_k}{D_k}\gamma_{2k}+\frac{D_{1k}}{D_{2k}}\gamma_{1k}\right]+\frac{I_k}{m_k}\frac{r_{2k}}{D_{2k}}\left(1-\frac{D_{1k}}{D_{2k}}\right)\right\}+m_k\dot{\gamma}_{1k}\left\{2\zeta_{k\gamma_1}\omega_{k\gamma_1}\right\}\\
&+m_k\dot{\gamma}_{2k}\left\{\frac{r_{1k}r_{2k}}{D_{2k}}\Delta R_k\Omega\sin\left[\frac{d_k}{D_{2k}}\gamma_{2k}+\frac{D_{1k}}{D_{2k}}\gamma_{1k}\right]-\frac{r_{1k}r_{2k}}{2}\Omega\sin\gamma_{2k}-\frac{r_{1k}r_{2k}}{D_{2k}}\Delta R_k\Omega\sin\left[\frac{r_{2k}}{D_{2k}}\gamma_{2k}-\frac{D_{1k}}{D_{2k}}\gamma_{1k}\right]\right\}\\
&-m_k\dot{\gamma}_{1k}\dot{\gamma}_{2k}\left\{\frac{r_{1k}r_{2k}}{2}\sin\gamma_{2k}+\frac{r_{2k}}{D_{2k}}\Delta R_k d_k\left(1-\frac{D_{1k}}{D_{2k}}\right)\sin\left[\frac{d_k}{D_{2k}}\gamma_{2k}+\frac{D_{1k}}{D_{2k}}\gamma_{1k}\right]\right.\\
&\quad\left.+\frac{r_{1k}r_{2k}}{D_{2k}}\Delta R_k\left(1-\frac{D_{1k}}{D_{2k}}\right)\sin\left[\frac{r_{2k}}{D_{2k}}\gamma_{2k}-\frac{D_{1k}}{D_{2k}}\gamma_{1k}\right]\right\}\\
&+m_k\dot{\gamma}_{1k}^2\left\{\frac{r_{1k}}{2}\Delta R_k\frac{D_{1k}}{D_{2k}}\left(1-\frac{D_{1k}}{D_{2k}}\right)\sin\left[\frac{r_{2k}}{D_{2k}}\gamma_{2k}-\frac{D_{1k}}{D_{2k}}\gamma_{1k}\right]-\frac{r_{2k}}{2}\Delta R_k\frac{D_{1k}}{D_{2k}}\left(1-\frac{D_{1k}}{D_{2k}}\right)\sin\left[\frac{d_k}{D_{2k}}\gamma_{2k}+\frac{D_{1k}}{D_{2k}}\gamma_{1k}\right]\right\}\\
&+m_k\dot{\gamma}_{2k}^2\left\{\frac{r_{2k}}{2}\Delta R_k\left[\frac{D_{1k}}{D_{2k}}-2\frac{d_k}{D_{2k}}+\frac{d_k^2}{D_{2k}^2}\right]\sin\left[\frac{d_k}{D_{2k}}\gamma_{2k}+\frac{D_{1k}}{D_{2k}}\gamma_{1k}\right]\right.\\
&\quad\left.-\frac{r_{1k}r_{2k}}{4}\sin\gamma_{2k}-\frac{r_{1k}}{2}\Delta R\left(\frac{r_{2k}}{D_{2k}}\right)^2\sin\left[\frac{r_{2k}}{D_{2k}}\gamma_{2k}-\frac{D_{1k}}{D_{2k}}\gamma_{1k}\right]\right\}\\
&+m_k\Omega^2\left\{\frac{r_{1k}}{2}R_{ok}\sin\gamma_{1k}+\frac{r_{2k}}{2}R_{ok}\sin(\gamma_{1k}+\gamma_{2k})-\frac{r_{1k}}{2}\Delta R_k\frac{D_{1k}}{D_{2k}}\sin\left[\frac{r_{2k}}{D_{2k}}\gamma_{2k}-\frac{D_{1k}}{D_{2k}}\gamma_{1k}\right]\right.\\
&\quad\left.+R_{ok}\Delta R_k\left(1-\frac{D_{1k}}{D_{2k}}\right)\sin\left[\frac{r_{2k}}{D_{2k}}\gamma_{2k}+\left(1-\frac{D_{1k}}{D_{2k}}\right)\gamma_{1k}\right]+\frac{r_{2k}}{2}\Delta R_k\frac{D_{1k}}{D_{2k}}\sin\left[\frac{d_k}{D_{2k}}\gamma_{2k}+\frac{D_{1k}}{D_{2k}}\gamma_{1k}\right]\right\}=0
\end{aligned}
$$

Figure 49. Non-linear Equations of Motion with Hub Inplane Degrees-of-Freedom.

γ_{2k} – EQUATION

$$-m_k\ddot{x}\left\{\frac{r_{2k}}{2}\sin(\gamma_{1k}+\gamma_{2k}+\psi_k)+r_{2k}\frac{\Delta R_k}{D_{2k}}\sin\left[\frac{r_{2k}}{D_{2k}}\gamma_{2k}+\left(1-\frac{D_{1k}}{D_{2k}}\right)\gamma_{1k}+\psi_k\right]\right\}$$

$$+m_k\ddot{y}\left\{\frac{r_{2k}}{2}\cos(\gamma_{1k}+\gamma_{2k}+\psi_k)+r_{2k}\frac{\Delta R_k}{D_{2k}}\cos\left[\frac{r_{2k}}{D_{2k}}\gamma_{2k}+\left(1-\frac{D_{1k}}{D_{2k}}\right)\gamma_{1k}+\psi_k\right]\right\}$$

$$+m_k\ddot{\gamma}_{1k}\left\{\left(\frac{r_{2k}}{2}\right)^2+(\Delta R_k)^2\left(\frac{r_{2k}}{D_{2k}}\right)\left(1-\frac{D_{1k}}{D_{2k}}\right)+\frac{r_{1k}r_{2k}}{4}\cos\gamma_{2k}+\frac{I_k}{m_k}\frac{r_{2k}}{D_{2k}}\left(1-\frac{D_{1k}}{D_{2k}}\right)\right.$$

$$\left.+\frac{r_{1k}r_{2k}}{2}\frac{\Delta R_k}{D_{2k}}\cos\left[\frac{r_{2k}}{D_{2k}}\gamma_{2k}-\frac{D_{1k}}{D_{2k}}\gamma_{1k}\right]+\frac{r_{2k}}{2}\Delta R_k\left[2-\frac{D_{1k}+d_k}{D_{2k}}\right]\cos\left[\frac{d_k}{D_{2k}}\gamma_{2k}+\frac{D_{1k}}{D_{2k}}\gamma_{1k}\right]\right\}$$

$$+m_k\ddot{\gamma}_{2k}\left\{\frac{r_{2k}^2}{4}+\left(\frac{r_{2k}\Delta R_k}{D_{2k}}\right)^2+r_{2k}^2\frac{\Delta R_k}{D_{2k}}\cos\left[\frac{d_k}{D_{2k}}\gamma_{2k}+\frac{D_{1k}}{D_{2k}}\gamma_{1k}\right]+\frac{I_k}{m_k}\left(\frac{r_{2k}}{D_{2k}}\right)^2\right\}$$

$$+m_k\dot{\gamma}_{1k}\left\{\frac{r_{1k}r_{2k}}{2}\Omega\sin\gamma_{2k}-r_{1k}r_{2k}\Omega\frac{\Delta R_k}{D_{2k}}\sin\left[\frac{d_k}{D_{2k}}\gamma_{2k}+\frac{D_{1k}}{D_{2k}}\gamma_{1k}\right]\right.$$

$$\left.+\frac{r_{1k}r_{2k}}{D_{2k}}\Delta R_k\Omega\sin\left[\frac{r_{2k}}{D_{2k}}\gamma_{2k}-\frac{D_{1k}}{D_{2k}}\gamma_{1k}\right]\right\}+m_k\dot{\gamma}_{2k}\left\{2\zeta_{k_{\gamma_2}}\omega_{k_{\gamma_2}}\right\}$$

$$-m_k\dot{\gamma}_{1k}\dot{\gamma}_{2k}\left\{r_{2k}^2\Delta R_k\frac{D_{1k}}{D_{2k}^2}\sin\left[\frac{d_k}{D_{2k}}\gamma_{2k}+\frac{D_{1k}}{D_{2k}}\gamma_{1k}\right]\right\}$$

$$+m_k\dot{\gamma}_{1k}^2\left\{\frac{r_{1k}r_{2k}}{4}\sin\gamma_{2k}+\frac{r_{1k}r_{2k}}{2}\frac{\Delta R_k}{D_{2k}}\sin\left[\frac{r_{2k}}{D_{2k}}\gamma_{2k}-\frac{D_{1k}}{D_{2k}}\gamma_{1k}\right]\right.$$

$$\left.-\frac{r_{1k}r_{2k}}{2}\frac{\Delta R_k}{D_{2k}}\left(1-\frac{D_{1k}}{D_{2k}}\right)\sin\left[\frac{d_k}{D_{2k}}\gamma_{2k}+\frac{D_{1k}}{D_{2k}}\gamma_{1k}\right]-\frac{r_{2k}^2}{2}\frac{\Delta R_k}{D_{2k}}\frac{D_{1k}}{D_{2k}}\sin\left[\frac{d_k}{D_{2k}}\gamma_{2k}+\frac{D_{1k}}{D_{2k}}\gamma_{1k}\right]\right\}$$

$$-m_k\dot{\gamma}_{2k}^2\left\{\frac{d_k}{2}\left(\frac{r_{2k}}{D_{2k}}\right)^2\Delta R_k\sin\left[\frac{d_k}{D_{2k}}\gamma_{2k}+\frac{D_{1k}}{D_{2k}}\gamma_{1k}\right]\right\}$$

$$+m_k\Omega^2\left\{\frac{r_{1k}r_{2k}}{4}\sin\gamma_{2k}+\frac{r_{2k}}{2}R_{ok}\sin(\gamma_{1k}+\gamma_{2k})+r_{2k}R_{ok}\frac{\Delta R_k}{D_{2k}}\sin\left[\frac{r_{2k}}{D_{2k}}\gamma_{2k}+\left(1-\frac{D_{1k}}{D_{2k}}\right)\gamma_{1k}\right]\right.$$

$$\left.+\frac{r_{1k}r_{2k}}{2}\frac{\Delta R_k}{D_{2k}}\sin\left[\frac{r_{2k}}{D_{2k}}\gamma_{2k}-\frac{D_{1k}}{D_{2k}}\gamma_{1k}\right]+\frac{r_{2k}}{2}d_k\frac{\Delta R_k}{D_{2k}}\sin\left[\frac{d_k}{D_{2k}}\gamma_{2k}+\frac{D_{1k}}{D_{2k}}\gamma_{1k}\right]\right\}=0$$

Figure 49. Continued.

X - EQUATION

$$(m_G + M_T)\ddot{x} + 2m_G\omega_x\zeta_x\dot{x} + m_G\omega_x^2 x$$

$$+\sum_{k=1}^{N}\Bigg\{-m_k\ddot{\gamma}_{1k}\left[\frac{r_{1k}}{2}\sin(\gamma_{1k}+\psi_k) + \frac{r_{2k}}{2}\sin(\gamma_{1k}+\gamma_{2k}+\psi_k) + \Delta R_k\left(1-\frac{D_{1k}}{D_{2k}}\right)\sin\left[\frac{r_{2k}}{D_{2k}}\gamma_{2k} + \left(1-\frac{D_{1k}}{D_{2k}}\right)\gamma_{1k} + \psi_k\right]\right]$$

$$-m_k\ddot{\gamma}_{2k}\left[\frac{r_{2k}}{2}\sin(\gamma_{1k}+\gamma_{2k}+\psi_k) + \Delta R_k\frac{r_{2k}}{D_{2k}}\sin\left[\frac{r_{2k}}{D_{2k}}\gamma_{2k} + \left(1-\frac{D_{1k}}{D_{2k}}\right)\gamma_{1k} + \psi_k\right]\right]$$

$$-m_k\dot{\gamma}_{1k}\left[r_{1k}\Omega\cos(\gamma_{1k}+\psi_k) + r_{2k}\Omega\cos(\gamma_{1k}+\gamma_{2k}+\psi_k)\right.$$

$$\left. + 2\Delta R_k\Omega\left(1-\frac{D_{1k}}{D_{2k}}\right)\cos\left[\frac{r_{2k}}{D_{2k}}\gamma_{2k} + \left(1-\frac{D_{1k}}{D_{2k}}\right)\gamma_{1k} + \psi_k\right]\right]$$

$$-m_k\dot{\gamma}_{2k}\left[r_{2k}\Omega\cos(\gamma_{1k}+\gamma_{2k}+\psi_k) + 2r_{2k}\Omega\frac{\Delta R_k}{D_{2k}}\cos\left[\frac{r_{2k}}{D_{2k}}\gamma_{2k} + \left(1-\frac{D_{1k}}{D_{2k}}\right)\gamma_{1k} + \psi_k\right]\right]$$

$$-m_k\dot{\gamma}_{1k}\dot{\gamma}_{2k}\left[r_{2k}\cos(\gamma_{1k}+\gamma_{2k}+\psi_k) + 2\Delta R_k\frac{r_{2k}}{D_{2k}}\left(1-\frac{D_{1k}}{D_{2k}}\right)\cos\left[\frac{r_{2k}}{D_{2k}}\gamma_{2k} + \left(1-\frac{D_{1k}}{D_{2k}}\right)\gamma_{1k} + \psi_k\right]\right]$$

$$-m_k\dot{\gamma}_{1k}^2\left[\frac{r_{1k}}{2}\cos(\gamma_{1k}+\psi_k) + \frac{r_{2k}}{2}\cos(\gamma_{1k}+\gamma_{2k}+\psi_k) + \Delta R_k\left(1-\frac{D_{1k}}{D_{2k}}\right)^2\cos\left[\frac{r_{2k}}{D_{2k}}\gamma_{2k} + \left(1-\frac{D_{1k}}{D_{2k}}\right)\gamma_{1k} + \psi_k\right]\right]$$

$$-m_k\dot{\gamma}_{2k}^2\left[\frac{r_{2k}}{2}\cos(\gamma_{1k}+\gamma_{2k}+\psi_k) + \Delta R_k\left(\frac{r_{2k}}{D_{2k}}\right)^2\cos\left[\frac{r_{2k}}{D_{2k}}\gamma_{2k} + \left(1-\frac{D_{1k}}{D_{2k}}\right)\gamma_{1k} + \psi_k\right]\right]$$

$$-m_k\Omega^2\left[\frac{r_{1k}}{2}\cos(\gamma_{1k}+\psi_k) + \frac{r_{2k}}{2}\cos(\gamma_{1k}+\gamma_{2k}+\psi_k) + R_{0k}\cos\psi_k\right.$$

$$\left. + \Delta R_k\cos\left[\frac{r_{2k}}{D_{2k}}\gamma_{2k} + \left(1-\frac{D_{1k}}{D_{2k}}\right)\gamma_{1k} + \psi_k\right]\right]\Bigg\} = F_x$$

Figure 49. Continued.

Y-EQUATION

$$(m_s + M_T)\ddot{y} + 2m_s\omega_y\zeta_y\dot{y} + m_s\omega_y^2 y$$

$$+\sum_{k=1}^{N}\Bigg\{+m_k\ddot{\gamma}_{1k}\left[\frac{r_{1k}}{2}\cos(\gamma_{1k}+\psi_k) + \frac{r_{2k}}{2}\cos(\gamma_{1k}+\gamma_{2k}+\psi_k) + \Delta R_k\left(1-\frac{D_{1k}}{D_{2k}}\right)\cos\left[\frac{r_{2k}}{D_{2k}}\gamma_{2k} + \left(1-\frac{D_{1k}}{D_{2k}}\right)\gamma_{1k} + \psi_k\right]\right]$$

$$+m_k\ddot{\gamma}_{2k}\left[\frac{r_{2k}}{2}\cos(\gamma_{1k}+\gamma_{2k}+\psi_k) + \Delta R_k\frac{r_{2k}}{D_{2k}}\cos\left[\frac{r_{2k}}{D_{2k}}\gamma_{2k} + \left(1-\frac{D_{1k}}{D_{2k}}\right)\gamma_{1k} + \psi_k\right]\right]$$

$$-m_k\dot{\gamma}_{1k}\left[r_{1k}\Omega\sin(\gamma_{1k}+\psi_k) + r_{2k}\Omega\sin(\gamma_{1k}+\gamma_{2k}+\psi_k)\right.$$

$$\left.+ 2\Delta R_k\Omega\left(1-\frac{D_{1k}}{D_{2k}}\right)\sin\left[\frac{r_{2k}}{D_{2k}}\gamma_{2k} + \left(1-\frac{D_{1k}}{D_{2k}}\right)\gamma_{1k} + \psi_k\right]\right]$$

$$-m_k\dot{\gamma}_{2k}\left[r_{2k}\Omega\sin(\gamma_{1k}+\gamma_{2k}+\psi_k) + 2r_{2k}\Omega\frac{\Delta R_k}{D_{2k}}\sin\left[\frac{r_{2k}}{D_{2k}}\gamma_{2k} + \left(1-\frac{D_{1k}}{D_{2k}}\right)\gamma_{1k} + \psi_k\right]\right]$$

$$-m_k\dot{\gamma}_{1k}\dot{\gamma}_{2k}\left[r_{2k}\sin(\gamma_{1k}+\gamma_{2k}+\psi_k) + 2\Delta R_k\frac{r_{2k}}{D_{2k}}\left(1-\frac{D_{1k}}{D_{2k}}\right)\sin\left[\frac{r_{2k}}{D_{2k}}\gamma_{2k} + \left(1-\frac{D_{1k}}{D_{2k}}\right)\gamma_{1k} + \psi_k\right]\right]$$

$$-m_k\dot{\gamma}_{1k}^2\left[\frac{r_{1k}}{2}\sin(\gamma_{1k}+\psi_k) + \frac{r_{2k}}{2}\sin(\gamma_{1k}+\gamma_{2k}+\psi_k) + \Delta R_k\left(1-\frac{D_{1k}}{D_{2k}}\right)^2\sin\left[\frac{r_{2k}}{D_{2k}}\gamma_{2k} + \left(1-\frac{D_{1k}}{D_{2k}}\right)\gamma_{1k} + \psi_k\right]\right]$$

$$-m_k\dot{\gamma}_{2k}^2\left[\frac{r_{2k}}{2}\sin(\gamma_{1k}+\gamma_{2k}+\psi_k) + \Delta R_k\left(\frac{r_{2k}}{D_{2k}}\right)^2\sin\left[\frac{r_{2k}}{D_{2k}}\gamma_{2k} + \left(1-\frac{D_{1k}}{D_{2k}}\right)\gamma_{1k} + \psi_k\right]\right]$$

$$-m_k\Omega^2\left[\frac{r_{1k}}{2}\sin(\gamma_{1k}+\psi_k) + \frac{r_{2k}}{2}\sin(\gamma_{1k}+\gamma_{2k}+\psi_k) + R_{ok}\sin\psi_k\right.$$

$$\left.+ \Delta R_k\sin\left[\frac{r_{2k}}{D_{2k}}\gamma_{2k} + \left(1-\frac{D_{1k}}{D_{2k}}\right)\gamma_{1k} + \psi_k\right]\right]\Bigg\} = F_y$$

Figure 49. Concluded.

REFERENCES

1. Paul, William F.: Development and Evaluation of the Main Rotor Bifilar Absorber Proceedings of the 25th AHS Forum, May 1969.

2. Miao, W. and Mouzakis, T.: Non-Linear Dynamic Characteristics of the Rotor Bifilar Absorber 37th AHS Forum, May 1981.

3. Miao, W. and Mouzakis, T.: Bifilar Analysis Study - Volume I NASA CR 159227, August 1980.

4. Mouzakis, T.: Monofilar, A Dual Frequency Rotorhead Absorber Presented at AHS Northeast Region National Specialists' Meeting, Hartford, CT, November 1981.

1. Report No.	2. Government Accession No.	3. Recipient's Catalog No.
NASA CR-166088		

4. Title and Subtitle	5. Report Date
DEVELOPMENT OF MONOFILAR ROTOR HUB VIBRATION ABSORBER	May 1983
	6. Performing Organization Code

7. Author(s)	8. Performing Organization Report No.
J. Duh and W. Miao	
	10. Work Unit No.

9. Performing Organization Name and Address	11. Contract or Grant No.
UNITED TECHNOLOGIES CORPORATION Sikorsky Aircraft Division Stratford, Connecticut 06602	NAS1-16700
	13. Type of Report and Period Covered
12. Sponsoring Agency Name and Address	Contractor Report
National Aeronautics and Space Administration Washington, D.C. 20546	14. Sponsoring Agency Code

15. Supplementary Notes

Langley Technical Monitor: Dr. F. D. Bartlett, Jr.
The research effort which led to the results of this report was financially supported by the Sturctures Laboratory, USARTL (AVRADCOM).

16. Abstract

A design and ground test program was conducted to study the performance of the monofilar absorber for vibration reduction on a four-bladed helicopter. A monofilar is a centrifugally tuned two degree-of-freedom rotor hub absorber that provides force attenuation at two frequencies using the same dynamic mass. Linear and non-linear analyses of the coupled monofilar/airframe system were developed to study tuning and attenuation characteristics. Based on the analysis, a design was fabricated and impact bench tests verified the calculated non-rotating natural frequencies and mode shapes. Performance characteristics were measured using a rotating absorber test facility. These tests showed significant attenuation of fixed-system 4P hub motions due to 3P inplane rotating-system hub foces. In addition, detuning effects of the 3P monofilar modal response were small due to the nonlinearities and tuning pin slippage. However, attenuation of 4P hub motions due to 5P inplane hub forces was poor. The performance of the 5P monofilar modal response was degraded by torsional motion of the dynamic mass relative to the support arm which resulted in binding of the dynamic components. Analytical design studies were performed to evaluate this torsional motion problem. An alternative design is proposed which may alleviate the torsional motion of the dynamic mass.

17. Key Words (Suggested by Author(s))	18. Distribution Statement
Monofilar, Rotor Absorber, Dynamic Mass, Coupled Monofilar/Airframe Analysis, Rotating Absorber Test Facility, UH-60A, Tuning, Damping	Unclassified-Unlimited

19. Security Classif. (of this report)	20. Security Classif. (of this page)	21. No. of Pages	22. Price
Unclassified	Unclassified		

For sale by the National Technical Information Service, Springfield, Virginia 22161

End of Document